LBNL-40350
UC-410

ERNEST ORLANDO LAWRENCE
BERKELEY NATIONAL LABORATORY

Nonlinear Optical Properties of Atomic Vapor and Semiconductors

Doseok Kim
Materials Sciences Division

May 1997
Ph.D. Thesis

RECEIVED
JUN 23 1997
OSTI

MASTER

DISCLAIMER

This document was prepared as an account of work sponsored by the United States Government. While this document is believed to contain correct information, neither the United States Government nor any agency thereof, nor The Regents of the University of California, nor any of their employees, makes any warranty, express or implied, or assumes any legal responsibility for the accuracy, completeness, or usefulness of any information, apparatus, product, or process disclosed, or represents that its use would not infringe privately owned rights. Reference herein to any specific commercial product, process, or service by its trade name, trademark, manufacturer, or otherwise, does not necessarily constitute or imply its endorsement, recommendation, or favoring by the United States Government or any agency thereof, or The Regents of the University of California. The views and opinions of authors expressed herein do not necessarily state or reflect those of the United States Government or any agency thereof, or The Regents of the University of California.

Ernest Orlando Lawrence Berkeley National Laboratory
is an equal opportunity employer.

LBNL-40350

NONLINEAR OPTICAL PROPERTIES OF ATOMIC VAPOR AND SEMICONDUCTORS

DOSEOK KIM

Ph.D. Thesis

DEPARTMENT OF PHYSICS

University of California

and

MATERIALS SCIENCES DIVISION

Lawrence Berkeley National Laboratory

University of California

Berkeley, CA 94720

SPRING 1997

MASTER

DISTRIBUTION OF THIS DOCUMENT IS UNLIMITED

This work was supported by the Director, Office of Energy Research, Office of Basic Energy Sciences, Materials Sciences Division, of the U. S. Department of Energy under Contract No. DE-AC03-76SF00098.

DISCLAIMER

Portions of this document may be illegible in electronic image products. Images are produced from the best available original document.

DISCLAIMER

This report was prepared as an account of work sponsored by an agency of the United States Government. Neither the United States Government nor any agency thereof, nor any of their employees, make any warranty, express or implied, or assumes any legal liability or responsibility for the accuracy, completeness, or usefulness of any information, apparatus, product, or process disclosed, or represents that its use would not infringe privately owned rights. Reference herein to any specific commercial product, process, or service by trade name, trademark, manufacturer, or otherwise does not necessarily constitute or imply its endorsement, recommendation, or favoring by the United States Government or any agency thereof. The views and opinions of authors expressed herein do not necessarily state or reflect those of the United States Government or any agency thereof.

Abstract

Nonlinear Optical Properties of Atomic Vapor and Semiconductors

by

Doseok Kim

Doctor of Philosophy in Physics

University of California, Berkeley

Professor Yuen Ron Shen, Chair

This thesis contains the study of highly forbidden resonant second harmonic generation (SHG) in atomic potassium vapor using tunable picosecond pulses. Various output characteristics of vapor SHG have been investigated including the input intensity dependence, potassium vapor density dependence, buffer gas pressure dependence, and spatial profile. A pump–probe experiment was conducted to probe time dependence of the SHG signal. The experimental results can be understood from an ionization–initiated dc–field–induced SHG model. A theory of dc–field–induced SHG model is developed which takes into account the time development of the dc electric field in detail. This temporal buildup of the dc field along with two–photon transient coherent excitation of the one–photon–forbidden transition can explain the experimental results quantitatively, including the previous SHG results in atomic vapor with nanosecond laser pulses.

Recently, the discovery of new nonlinear optical crystals such as barium borate (β–BaB_2O_4, BBO) and lithium borate (LiB_3O_5, LBO) has greatly improved the performance of a tunable coherent optical devices based on optical parametric gen-

eration and amplification. In the second part of this thesis, a homebuilt picosecond optical parametric generator/amplifier (OPG/OPA) system is described in detail, including its construction details and output characteristics. The OPG/OPA system based on BBO crystals combined with difference frequency generation from a $AgGaS_2$ crystal generates picosecond output with a tuning range from 0.4 μm to 9 μm and a maximum output energy of $\sim$400 μJ/pulse. This laser device has found many useful applications in spectroscopic studies including surface nonlinear optical spectroscopy via sum–frequency generation (SFG).

The last part of this thesis reports studies on multiphoton–excited photoluminescence from porous silicon and GaN. Multiphoton excitation and photoluminescence can give numerous complementary information about semiconductors not obtainable with one–photon, above–bandgap excitation. Photoluminescence spectra and photoluminescence excitation spectra were measured with multiphoton excitation of porous silicon. Using the tunable, picosecond output from the above–mentioned OPG/OPA system, we were able to detect visible photoluminescence from porous silicon with pump wavelength as long as $\sim$5 μm. Energy conservation requires at least 9 photons at 5 μm wavelength to yield photoluminescence in the visible range. On GaN, two–photon photoluminescence excitation (PLE) spectrum around the bandgap was found to agree well with the theoretical prediction. The multiphoton PLE spectra of GaN with pump wavelength in the infrared range showed the existence of midgap defect states around 1 eV above the valence band.

Acknowledgements

First, I cannot thank my advisor Professor Y. R. Shen enough for his guidance, support, and patience on me throughout my years in the Shen group. His clear thinking in physical problems, optimism towards challenges, and love and enthusiasm for the subject set me very tough standard to follow throughout my life.

I was first introduced to experimental physics with lasers on which I never had experience before by Chris Mullin. I owe him a lot of help as we dealt with the infamous amplified dye laser system and studied the second harmonic generation in potassium vapor.

I would like to thank Quan Du and Rodney Chin for their help as we built the new optical parametric generator/amplifier system. Without their knowledge and help, it would have taken me much longer to make the system work. Paulo Miranda's help in building the sum–frequency detection setup and in polishing the system to a better performance was also invaluable.

I have also indebted from numerous discussions with many members in our group. It was a great fortune to be with such a talented, hard working group of people pursuing similar problems in physics. Especially, Paulo Miranda and Xiaowei Zhuang taught me a lot about surface sum–frequency and surface second–harmonic generation. I wish good luck to the newer members of the group, Xing Wei and Seokcheol Hong. I also want to thank Barbara Gordon, Barbara Iwai, and Anne Takizawa for helping me on just about anything.

During the past years in the group, many students, postdocs, and visitors have

been in our group. I have benefited from all of them through discussions on physics and on life in general and feel sorry not to be able to name them all. Special thanks to Lorenzo Marrucci, Christian Jacobson, Ralf Muenster, Tony Schuster, Imke Libon, Carsten Voelkmann, Markus Jarasch, Shen Ye, Minyao Mao, and Joachim Diener.

Throughout the graduate student years, the unselfish support from our parents was most important even if they could be only reached remotely by phone. This thesis is dedicated to them and also to my wife Wonran Cho and my son Byunghoon Kim.

Contents

Chapter 1

Introduction

It is well known from symmetry arguments [1] that optical second harmonic generation (SHG) is forbidden in centrosymmetric media. Especially SHG in atomic vapor is highly forbidden nonlinear optical process, both microscopically and macroscopically [1, 2]. Yet many experiments in the past have demonstrated that SHG in atomic vapors can be easily observed with an exciting laser pulse two–photon tuned to an atomic resonance [3]. Clearly, in those experiments, the symmetry of the medium must have been broken during the laser excitation. Several mechanisms have been proposed to provide the required broken symmetry but the success was limited [3, 4].

The first part of this thesis is on study of this highly forbidden resonant second harmonic generation in potassium vapor using tunable picosecond pulses. In the beginning of this chapter, the previous experiments on SHG from atomic vapor are reviewed along with several proposed mechanisms. It was shown that all the

proposed mechanisms cannot explain the measured SHG satisfactorily except the one on ionization–initiated dc–field–induced SHG proposed by Mossberg *et al.* [3]. The dc field generated by laser ionization of atoms is capable of breaking the microscopic and macroscopic inversion symmetry of the atomic vapor. One can then easily speculate that the input intensity dependence of SHG should be much more than I^2 since in most experiments at least 3 photons are needed for laser ionization. Also there should be correlation between SHG and ionization as the laser is tuned to the resonances with different atomic transitions. But in experiments performed with tunable nanosecond pulses, input intensity dependence was found to be mostly I^2, and no clear correlation existed between SHG and ionization.

According to the above dc–field–induced SHG model, it should take a finite amount of time (10–100 ps) for the dc field to build up from laser ionization. To probe such a time–varying dc field, picosecond laser pulses are needed. This is basically the idea behind our work on SHG in potassium vapor. In the experimental part of the next chapter, the output characteristics of resonant SHG by picosecond laser pulses were measured including the input intensity dependence, vapor density dependence, buffer gas pressure dependence, and spatial profile of the output. Also a pump–probe experiment was conducted to probe time dependence of the SHG signal. It is shown later in the chapter that all the experimental results can be understood from an ionization–initiated dc–field–induced SHG model. A theory of dc–field–induced SHG model was developed which takes into account the time development of the dc electric field in detail. It was found that transient coherence induced by two–

photon laser excitation is necessary to explain our results. This temporal buildup of the dc field along with transient coherent excitation between a two–photon–allowed but one–photon–forbidden transition can explain the experimental results quantitatively, including the previous results obtained by others with nanosecond laser pulses.

In the second part of the thesis, a picosecond optical parametric generator/amplifier (OPG/OPA) system is described. Optical parametric devices have been considered ideal coherent tunable sources over conventional dye lasers for a long time [5], but the lack of suitable nonlinear optical crystals with large nonlinearity and high laser damage threshold delayed the advancement of such devices. Recently, the discovery of new nonlinear crystals such as barium borate (β–BaB_2O_4, BBO) and lithium borate (LiB_3O_5, LBO) have changed the scene [6].

Our homebuilt OPG/OPA system using BBO crystals combined with difference frequency generation in a $AgGaS_2$ crystal allows a tuning range from $\sim$0.4 μm to $\sim$9 μm with an output up to 400 μJ/pulse. In the first part of this chapter, construction of each section of the system is described in detail. Later output characteristics including output energy, pulsewidth, and the laser linewidths are presented. This system has many useful applications in spectroscopy including surface sum–frequency generation (SFG). Several sample surface SFG spectra are shown as examples.

The last part of this thesis contains the experiments on multiphoton–excited photoluminescence (PL) observed in porous silicon and GaN. Multiphoton excitation

and photoluminescence can give complementary information about semiconductors not obtainable with one–photon, above–bandgap transitions. For example, a scaling law was found from the measurement of two–photon absorption coefficients of several direct gap semiconductors [7]. Also enhancement of transition strengths in one–photon absorption and luminescence for clusters and nanoparticles of semiconductors (as compared to bulk) is expected to be even stronger for multiphoton transitions.

We first studied multiphoton–excited photoluminescence from porous silicon. After the discovery of efficient visible luminescence at room temperature [8], porous silicon has been studied extensively as a possible material for Si–based optoelectronic devices. In particular, its photoluminescence properties have been well investigated, but there are very few studies of photoluminescence by multiphoton excitation [9]. Using the tunable, picosecond output from the our OPG/OPA system, multiphoton photoluminescence spectra and photoluminescence excitation spectra were obtained. Visible photoluminescence at the pump wavelength as long as $\sim$5 μm could be easily detected, resulting from absorption of at least 9 photons.

We also studied multiphoton–excited photoluminescence from GaN. GaN is considered to be one of the most promising materials for short wavelength light emitting devices and electronic devices for high temperature and high power applications [10]. Using the above OPG/OPA system, PL spectra, input intensity dependence of PL, and photoluminescence excitation spectra were obtained. The two–photon photoluminescence excitation (PLE) spectra near the bandgap of GaN showed good agree-

ment with theoretical prediction. The multiphoton photoluminescence excitation spectra in the infrared pump wavelength region showed a peak at $\sim$1 eV, providing direct evidence of the existence of midgap defect states around 1 eV above the valence band, in agreement with previous experimental results [11].

Bibliography

[1] See, for example, Y. R. Shen, *The Principles of Nonlinear Optics* (John Wiley & Sons, New York, 1984).

[2] D. L. Andrews, J. Phys. B **13**, 4091 (1980); T. F. Heinz and D. P. DiVincenzo, Phys. Rev. A **42**, 6249 (1990).

[3] T. Mossberg, A. Flusberg, and S.R. Hartmann, Opt. Commun. **25**, 121 (1978); J. Okada, Y. Fukuda, and M. Matsuoka, J. Phys. Soc. Jpn. **50**, 1301 (1981); J. Bokor, R. R. Freeman, R. L. Panock, and J. C. White, Opt. Lett. **6**, 182 (1981); M. Lu and J. Tsai, J. Phys. B **23**, 921 (1990).

[4] D. S. Bethune, Phys. Rev. A **23**, 3139 (1981).

[5] J. A. Giordmaine and R. C. Miller, Phys. Rev. Lett. **14**, 973 (1965); R. A. Baumgartner and R. L. Byer, IEEE. J. Quantum Electron. **QE–15**, 432 (1979).

[6] J. Y. Huang, J. Y. Zhang, Y. R. Shen, C. Chen, and B. Wu, Appl. Phys. Lett. **57**, 1961 (1990); H. J. Krause and W. Daum, Appl. Phy. Lett. **60**, 18 (1992); J. Y. Huang, J. Y. Zhang, Y. R. Shen, and C. Chen, J. Opt. Soc. Am. B **10**, 1758 (1993).

[7] E. W. Van Stryland *et al.*, Opt. Eng. **24**, 613 (1985); J. A. Bolger, *et al.*, Opt. Commun. **97**, 203 (1993).

[8] L. T. Canham, Appl. Phys. Lett. **57**, 1046 (1990).

[9] X. Wang *Porous Silicon*, edited by Z. Chuan and R. Tsu (World Scientific, River Edge, NJ, 1994), p. 77–98; J. Wang *et al.*, Phys. Rev. Lett. **69**, 3252, (1992); R. P. Chin, Y. R. Shen, and V. Petrova–Koch, Science, **270**, 776 (1995); J. Diener *et al.*, Phys. Rev. B **52**, R6817 (1995).

[10] S. Strite and H. Morkoc, J. Vac. Sci. Technol. B **10**, 1237 (1992); H. Morkoc *et al.*, J. Appl. Phys. **76**, 1363 (1994).

[11] P. Perlin *et al.*, Phy. Rev. Lett. **75**, 296 (1995); D. M. Hoffmann *et al.*, Phys. Rev. B **52**, 16072 (1995).

Chapter 2

Second Harmonic Generation in Atomic Vapor

2.1 Introduction

Atomic vapors have long been the media of interest for nonlinear optics studies [1]. Their exceptionally large resonant nonlinearities have led to many interesting nonlinear optical effects. Resonant wave mixing in atomic vapors can be readily observed and has been used to generate tunable ultraviolet and infrared coherent radiation [2, 3]. However, second–order nonlinear optical processes are forbidden by symmetry in an isotropic medium [4]. Second harmonic generation (SHG), in particular, is forbidden to all orders of multipole expansion if the infinite plane wave geometry can be assumed [5]. In an atomic vapor, the second–order nonlinear response is also forbidden by microscopic symmetry. Consider, for example, the

case of an alkali vapor. The resonant hyperpolarizability $\alpha^{(2)}(2\omega)$ with the second harmonic frequency 2ω near an ns–$n'd$ transition becomes nonvanishing only if the electric quadrupole contribution is included [6, 7]. If 2ω is resonant with an ns–$n's$ transition, then $\alpha^{(2)}(2\omega)$ vanishes in all orders of multipole expansion. Thus, naturally, one would not anticipate observation of SHG from atomic vapors. It was therefore a total surprise when Mossberg *et al.* [8] first reported the result of resonant SHG in thallium vapor. Many others subsequently reported similar findings in other atomic vapors [9, 10, 11, 12, 13, 14].

That resonant SHG in an atomic vapor can be readily observed with pulsed lasers and the output is fairly strong suggests that both microscopic and macroscopic symmetries of the medium must have been broken in the process. Mossberg *et al.* [8] first proposed that symmetry breaking could result from the presence of a dc field generated by multiphoton ionization of the atoms. Later experiments however found no correlation between SHG and the degree of ionization in the medium [14, 15]. The output also did not vary with the laser intensity as predicted [8, 9, 13, 14]. This led to the proposals of numerous other mechanisms to explain the observation [13, 16, 17, 18]. We now show, by time–resolved measurements and careful analysis of the problem, that resonant SHG in an atomic vapor is indeed induced by an ionization–initiated dc field, and essentially all experimental results can be satisfactorily explained with this mechanism [19].

We first give a brief review on previous experiments and various proposed mechanisms of SHG in atomic vapor in the next section. We then present in Secs. 2.3

and 2.4 experimental arrangements and results of our own work using picosecond laser pulses. Finally, Sec. 2.5 describes the theory of dc–field generation by multiphoton ionization of atoms and subsequent dc–field–induced SHG in atomic vapor. The theory is shown to predict results that agree well with the experiment.

2.2 Review of Past Experiments and Proposed Mechanisms

2.2.1 Past experiments

Resonant SHG in atomic vapor was first observed by Mossberg *et al.* [8] in Thallium vapor. Using a 7 ns, 0.2 kW dye laser pulse focused to 200 μm in a vapor density of 7×10^{15} /cm^3, they obtained $\sim 5 \times 10^3$ second–harmonic photons in the output. They reported that the output depended both on the square of the input power and on the square of the density of the vapor and proposed that the electric field produced by three–photon ionization of the Tl atoms could break the symmetry and induce the observed SHG.

Subsequent experiments by many others in alkali [9, 11, 13, 14, 17, 20], alkali–earth, and other metallic vapors [10, 12, 15] yielded similar results. In most of the experiments, nanosecond dye laser pulses were used and resonant enhancement of SHG around two–photon s–s, s–p, s–d, or p–p transitions of the vapor was investigated. The resonant SHG around s–s transitions [9, 12, 13, 14] has attracted

particular attention since the process is expected to be both microscopically and macroscopically forbidden to all multipole orders.

With tunable dye lasers, typical input intensity used ranged from 10^6 W/cm^2 to 10^9 W/cm^2. At 10^9 W/cm^2, an SHG efficiency as high as 10^{-5} has been reported in sodium vapor [11]. If ionization of vapor is responsible for SHG, one would expect that SHG be proportional to I^n with $n \geq 2$, where I is the input laser intensity. Many groups [8, 9, 11, 13], however, reported the observation of an I^2 dependence. Also, the electrons released from multiphoton ionization were measured simultaneously with SHG but little correlation between ionization and SHG strength was found [14, 15]. The vapor density dependence of SHG usually showed an N^2 dependence [8, 9, 13], although an N^4 dependence was also reported at s–p two–photon resonances [13, 17].

Okada *et al.* [9] used the cylindrical lens to purposely focus the beam either in horizontal or vertical direction and measured the SHG polarization from the s–s resonance of the Li vapor. They found that the SHG was mainly polarized along the gradient of the input beam intensity and explained it in terms of a dc–field–induced SHG model. Subsequently, SHG polarization has been measured in several experiments and different results have been reported depending on the combination of ground and excited states used [8, 11, 13]. Output profile of SHG is difficult to measure without spectral filtering since allowed four–wave–parametric emission from a nearby state is usually much stronger than the SHG signal. Using the nonresonant, intense picosecond laser pulses, pictures of the SHG

profile on sodium vapor was first taken by Miyazaki *et al.* [20] and they showed a doughnut (with circular polarization input) or bimodal (with linear polarization input) profile. This SHG profile measurement was repeated later in sodium vapor [11] and in xenon vapor [21] with nonresonant, picosecond pulses and a doughnut or bimodal SHG profile was also observed.

2.2.2 Proposed mechanisms

Several symmetry–breaking mechanisms have been proposed to explain SHG in atomic vapor [8, 13, 16, 17, 18, 20]. Mossberg *et al.* [8] suggested that laser–induced ionization followed by a buildup of dc electric field due to charge separation could be the dominant mechanism. Stoicheff and coworkers recently showed that this model described their results of resonant SHG in atomic hydrogen very well [22, 23]. This theory of dc–field–induced SHG will be developed in detail in a later section to explain our experimental results with picosecond laser pulses as well as those of others. Here we shall review the other proposed models and discuss their inherent difficulties.

Superradiance

The observed resonant SHG could be due to superradiance [24] if the pulsed two–photon coherent transient excitation is so strong that between the ground and excited states an inverted population is actually established. To check this possibility, in one of the nanosecond experiments a probe laser beam tuned to

the transition frequency (SHG frequency) was propagated into the vapor together with the pump pulse but no gain was observed [13], indicating that the population of the system was not inverted. In our case of picosecond SHG in potassium vapor, the two–photon excitation from $4s$ to $9d$ was estimated to be 1 % with a typical laser intensity of 10 GW/cm^2. It is certainly too weak for superradiance to occur.

SHG due to quadrupole nonlinearity

Resonant SHG could arise from the quadrupole nonlinearity of the vapor. However, unlike the case with two noncollinear, cross–polarized pump beams [7], the amount of quadrupole SHG due to a single, focused pump beam is generally too small to be significant [11, 18]. Bethune [18] has estimated the quadrupole SHG generated by a focused laser beam in an atomic vapor. Here we use his theory on potassium vapor as an example. Since the dipole and the quadrupole matrix elements between $4s$, np, and $9d$ states of potassium are known [25, 26], we can estimate the quadrupole nonlinear susceptibility of potassium.

$$\begin{aligned} \overleftrightarrow{\chi}^{(2)}_{Q}(2\omega) &\cong \frac{Ne^3}{30\hbar^2}\sum_{np}\frac{\langle 4s|\mathbf{r}^2|9d\rangle\langle 9d|\mathbf{r}|np\rangle\langle np|\mathbf{r}|4s\rangle}{(\omega_{4s,9d}-2\omega)(\omega_{4s,np}-\omega)} \\ &\approx 2\times 10^{-18}\ \text{esu}, \end{aligned} \tag{2.1}$$

where $N = 10^{16}$ cm^{-3} is assumed to be the number density of potassium, $\omega_{4s,9d} = (E_{9d} - E_{4s})/\hbar$, and $2\omega \sim \omega_{4s,9d}$. In the numerical estimate, we assumed $np = 4p$ being the only dominant intermediate state and obtained the values of the dipole moments from Ref. [25] and the value of the quadrupole moment ($\langle 4s|\mathbf{r}^2|9d\rangle = 2\times 10^{-17}$cm^2) from Ref. [26].

If the pump beam is a plane wave, the nonlinear polarization $\vec{P}^{(2)}(2\omega)$ resulting from $\overleftrightarrow{\chi}_{Q}^{(2)}$ is parallel to the beam propagation direction and therefore cannot radiate. For a focused pump beam with a confocal angle θ, however, $P(2\omega)$ does have a transverse radiating component. Let $\hat{z}$ be the propagation direction and $\hat{x}$ the direction of pump beam polarization, then the first nonvanishing term of $P_x^{(2)}(2\omega)$ is [18]

$$P_x^{(2)}(2\omega) = \chi_Q^{(2)}(2\omega)\frac{\theta^2\zeta}{4}\frac{\partial}{\partial x}(E^2), \tag{2.2}$$

where $\zeta(z) = (1 + iz/z_0)^{-1}$, $z_0 = kR^2/2$ is the confocal parameter, and E is the laser field. In our experiment with a picosecond pulsed laser with pump intensity 10 GW/cm^2 and focusing angle $\theta \approx 4 \times 10^{-4}$, $P_x^{(2)}(2\omega)$ is only 3×10^{-17} esu, which is four orders of magnitude smaller than what is needed to explain the observed SHG . In typical nanosecond SHG experiments, pump intensity and hence $P_x^{(2)}(2\omega)$ are even much smaller than in the picosecond case. We also note that resonant SHG observed at two-photon ns–$n's$ transitions [9, 12, 13, 14] is another strong evidence against this mechanism since all multipole moments including the quadrupole one should vanish in this case.

Collision–induced SHG

Several authors have proposed that atomic collisions may play a role in breaking the inversion symmetry of the vapor by mixing states of different angular momenta [13, 16, 17]. However, how the collision can break the macroscopic symmetry is not very clear. In most atomic vapor experiments, inert gas of an overwhelming

proportion was used as the buffer gas. Thus the primary collision partners of a metal atom were the inert gas atoms. The collisions can break the microscopic symmetry of the metal atoms by mixing the different l–states so that the second–order nonlinear polarizability of the atoms no longer vanishes under the electric–dipole approximation but such collisions cannot break the macroscopic symmetry of the vapor.

If the atomic density $n(\mathbf{r})$ in the laser beam is nonuniform, then with a non-vanishing nonlinear polarizability $\alpha^{(2)}$, the vapor system can have an effective quadrupole nonlinear susceptibility $\chi^{(2)}(2\omega) \propto \nabla n(\mathbf{r}) \cdot \overleftrightarrow{\alpha}^{(2)}$. This could happen with a finite–size pump beam as the excitation might cause a spatially nonuniform distribution of atoms in the ground and excited states. To estimate the effect, we use the dephasing impact parameter of l =50 Å as the maximum distance that may induce the microscopic symmetry breaking for a typical atomic collision [27] causing, for example, the potassium atom to have $|9d\rangle \longrightarrow a\,|9d\rangle + b|\,n'p\rangle$ where $|a^2| + |b^2| = 1$. This value of l together with the interatomic distance at a buffer gas pressure of 10 Torr translates to about 10 % of the atoms under the influence of collision at any time at that buffer gas pressure. Increasing the buffer gas pressure would increase collision–induced state mixing. Assuming that on average, 10 % of the potassium atoms are under the influence of collisions, we then have, near the $4s$–$9d$ two–photon resonance,

$$\chi^{(2)}(2\omega) \sim \frac{0.1\nabla n(r)e^3}{\hbar^2} \sum_{np} \frac{ab\langle 4s|r|np\rangle\langle np|r|9d\rangle\langle n'p|r|4s\rangle}{(\omega_{4s,9d} - 2\omega)(\omega_{4s,np} - \omega)} l \qquad (2.3)$$

where $n'p$ is the nearest p state to the $9d$ state. Even for the most optimistic case

of maximum microscopic symmetry breaking, i. e. $a = b = 0.5$, one would find $\chi^{(2)} \approx 10^{-23}$ esu, which is too small to account for the observed SHG. Moreover, in our experiments to be described later, we observed a signal that decreases with increase of Ar pressure in contrast to the prediction based on the collision–induced SHG.

Other mechanisms

The nonuniform excitation and ionization of the atomic vapor can create a nonuniform distribution of free electrons in space. This nonuniform plasma can generate a second–harmonic polarization [4].

$$\vec{P}(2\omega) = \frac{e^3}{4m^2\omega^4}(\nabla N_e \cdot \vec{E})\vec{E}, \tag{2.4}$$

where N_e is the free electron density. In most experimental conditions, this is too small to account for the observed SHG, as pointed out by Bethune [18]. For example, in our case of picosecond two–photon resonant $4s$–$9d$ excitation, the three–photon ionization is estimated to yield $N_e = 10^{12}$ cm^{-3} at 20 GW/cm^2. For a column of Gaussian–distributed electrons with a radius of 200 μm, the calculated polarization is five orders of magnitude too small.

The pump radiation pressure could separate the electrons from ions after the atoms are ionized and could produce rapidly a strong macroscopic dc electric field for field–induced SHG [20, 21, 28]. The ponderomotive potential U_p is responsible for the charge separation.

$$U_p = \frac{e^2E^2}{2m\omega^2}. \tag{2.5}$$

However, the movement of the electrons during a picosecond laser pulse subject to this potential is very small. For example, at 10 GW/cm^2, the electrons can move at most 10^{-10} cm in 2 ps, and the dc electric field thus produced is negligible compared to the dc field induced by diffusion of electrons, which will be discussed in detail in a later section.

2.2.3 Motivation of vapor SHG with picosecond pulses

From the review above, the dc–field–induced SHG model remains as the only viable candidate to explain SHG in atomic vapor. In the model, the electric field builds up when electrons released by ionization move away from the ions. It should take a finite amount of time for the electrons to move and the resultant dc field to build up after the laser ionization of atoms, and the observed dc–field–induced SHG should vary on the same time scale. However, in essentially all the previous experiments, nanosecond laser pulses were used and they would not have the needed time resolution to experience the time–varying dc field. A rough estimate shows that it takes less than 100 ps for the dc field to reach a maximum. Several SHG experiments with picosecond laser pulses have been reported [20, 21, 28], but they are nonresonant and difficult to relate to the nanosecond experiments since the lasers used were not tunable.

We carried out the first detailed study of picosecond, resonant SHG in an atomic vapor composed of potassium/argon mixture. We found that with a 2 psec, ~200 μJ pump pulse tuned to the two–photon resonant $4s$–$9d$ transition, SHG was

easily detectable. This was rather surprising since the build–up time of the dc field from laser ionization is of the order of 100 ps and therefore the dc field should be negligibly small during the presence of the laser pulse. This result are now understood after we realize that the short laser pulse can induce a two–photon coherent resonant excitation in the atoms that has dephasing time also of the order of 100 ps [27, 29]. Coherent emission of this coherent excitation is forbidden because of the selection rule against the $9d$–$4s$ transition, but becomes allowed in the presence of the dc field. Using the pump/probe scheme, we have actually observed the time–varying SHG resulting from the dc–field–induced emission of coherent excitation. Theoretical calculations based on the above picture yield a semi–quantitative agreement with experiment. In the following sections, we give a full account of our investigation.

2.3 Experimental Setup

The potassium/argon gas mixture was enclosed in a heat pipe, which was not operated in a heat–pipe mode [30]. The heat–pipe temperature was at $\sim$320°C and could be controlled to within 1°C. Accordingly, the vapor pressure of K was $\sim$0.6 Torr. The Ar buffer gas pressure was varied between 8 and 100 Torr. Windows on each end of the heat pipe allowed the passage of light; cooling of the ends kept the potassium atoms from sticking to the windows.

The experimental setup is shown in Fig. 2.1. A tunable picosecond pulsed dye laser

with four amplifier stages was used as the pump beam in the experiment. The system was constructed as follows. A frequency–doubled cw mode–locked YLF laser synchronously pumped a dye laser oscillator (with Rhodamine 6G dye) to yield 100 mW of 3 psec pulses at 100 MHz tunable in the 570—620 nm range. The output was sent through four Bethune–type dye amplifiers transversely pumped by a 10 Hz frequency–doubled Q-switched YAG laser. Two saturable dye jets were used between the amplifiers to suppress amplified spontaneous emission (ASE). The final amplified dye laser output, after spatial filtering to yield a TEM_{00} mode, was about 200 μJ/pulse at 10 Hz. In our pump–only experiment, the dye laser beam was loosely focused by a telescope to a radius of $\sim$300 μm and confocal length of $\sim$1 m in the heat pipe. In our pump–probe experiment, the beam was split into two by a polarizing beamsplitter, propagated along the two separate arms, and then recombined by another polarizing beamsplitter before passing through the telescope. The polarizer with a half–wave plate was placed before the beamsplitter to allow partition of the relative energy in the two arms in a continuous way. The pump and probe beams cross in the heat pipe with an angle of 0.2°. For the SHG experiment on $4s$–$10p$ resonance, an output from the widely tunable, picosecond optical parametric generator/amplifer pumped by the third–harmonic of the Nd:YAG laser was used [31]. The 15 ps laser pulse was two–photon tuned to the $4s$–$10p$ resonance of the vapor for the generation of second harmonic and later to the $4s$–$9d$ resonance for comparison.

A 3/4–meter f/7 double monochromator with 100 μm slits was used to detect

the SHG from the vapor cell with an 1 Å resolution. The signal was recorded by a photomultiplier and photon–counting gated–integrator system. The total detection efficiency was measured to be about 1 %. The beam alignment was fairly critical in our experiment. A CCD camera or position–sensitive quadrant photodiode was used to constantly monitor the beam intensity and position to assure the correct beam alignment.

2.4 Experimental Results

We first present the results of the single–beam pump–only experiment. With the pump pulses at 200 μJ/pulse and tuned to the two–photon $4s$–$9d$ resonance, SHG from the K vapor was easily observable. As shown in Fig. 2.2, for SHG from a 0.6 Torr K / 20 Torr Ar mixture, the output was well–resolved from the nearby $11s$–$4s$ luminescence signal or the much stronger four–wave–mixing signal from the $10p$–$4s$ transition. Most of the experiments discussed below were done with the laser tuned to the two–photon $4s$–$9d$ resonance, but results were similar for other s–d and s–s transitions, for example, the two–photon $4s$–$11s$ resonance.

Within the time resolution (~3 ns) of the photomultiplier and electronic detection system, the SH output pulse was synchronous with the pump pulse, and well–collimated in the forward direction. As a function of K vapor density N_K (varied by adjusting the temperature), the output exhibited an N_K^4 dependence for small N_K and gradually saturated to a constant level, as displayed in Fig. 2.3.

The input intensity dependence of the resonant SHG signal from the $9d$–$4s$ transition is presented in Fig. 2.4. It shows the I^8 dependence up to 10 GW/cm^2 and gradually saturates thereafter. The input intensity dependence of resonant SHG from the $11s$–$4s$ transition is also given in Fig. 2.4 for comparison. The results including the overall signal level and the input intensity at which SHG begins to saturate are very similar.

With the pump beam linearly polarized, the SHG output was found to be polarized mainly in the direction of input polarization with a polarization ratio $(S_{\parallel}/S_{\perp}) = 16$, where $S_{\parallel}$ $(S_{\perp})$ is the output power of the SH component polarized parallel (perpendicular) to the input polarization direction. The spatial beam profile of the SH output was also measured by scanning a 100 μm slit horizontally and vertically across the beam. Figure 2.5 depicts the result. The pump beam was vertically polarized. The figure describes an SH output profile that has two lobes along the direction of the input polarization.

The SHG should depend on the buffer gas pressure. This has been measured by Dinev [13] with nanosecond pump pulses. He found that the SHG signal did not change much until about 100 mbar above which it dropped rapidly. We studied in our picosecond pulse measurement the SHG dependence on the Ar buffer gas pressure P_{Ar} at two different pump intensities. The result is presented in Fig. 2.6. For the higher pump intensity, the dependence is close to $1/P_{Ar}$ for sufficiently large P_{Ar}, but at the lower intensity, it decreases faster than $1/P_{Ar}$.

The above descriptions apply to SHG resonant with $4s$–$9d$ or $4s$–$11s$ of K. We

also studied SHG with the pump tuned to the two–photon forbidden, but one–photon allowed $4s$–$10p$ transition. To have SHG more readily observable, 15 ps pump pulses from the optical parametric generator/amplifier system was employed. The SHG signal was detectable ($\sim$0.02 counts/shot) above 20 GW/cm^2 but decreased very rapidly below the noise limit when input intensity was decreased. At 20 GW/cm^2, the SHG from the $4s$–$10p$ resonance was more than 2 orders of magnitude smaller than that from the $4s$–$9d$ or $4s$–$11s$ resonance.

We now discuss the pump–probe experiment. For dc–field–induced SHG, we anticipated that the dc field builds up on a time scale of $\sim$100 ps. A picosecond pump–probe experiment would allow the pump pulse to initiate the dc field and the time–delayed probe pulse to probe the dc field buildup. In out experiment, the time–separated pump and probe pulsed beams cross at the center of the vapor cell at a small angle as shown in Fig. 2.1 and only the SHG signal generated along the probe beam was measured. The probe intensity was about 3 GW/cm^2, which was too weak to generate a measurable SHG signal by itself. With the pump pulse present , however, SHG by the probe pulse was readily detectible. The result of SHG as a function of the pump–probe time delay is displayed in Fig. 2.7 for two different pump intensities of 12 and 8 GW/cm^2. It is shown that at the higher pump intensity the signal rises with increase of time delay and reaches the maximum sooner. Note that even at negative time delay, the signal is significant. In Fig. 2.8, the dependence of SHG along the probe beam on the probe intensity is shown. The SHG signal was measured for a fixed pump–probe delay of 100 ps

and a fixed pump intensity. The data in Fig. 2.8 show an I^2_{probe}, instead of I^8_{pump} in the pump–only experiment discussed earlier.

In the pump–probe experiment, if the time delay is within the pulsewidth, another SH signal appears in the direction between the pump and probe propagation direction. The cross–correlation SH signal generated by varying the time delay between the pump and probe shown in Fig. 2.9(a) indicated that it was a picosecond pulse with a pulsewidth somewhat less that the laser pulsewidth, as seen by comparing the cross–correlation curve of Fig. 2.9(a) with the autocorrelation curve generated by pump pulse from a nonlinear crystal, given in Fig. 2.9(b). As seen from Fig. 2.9(a), the maximum intensity at zero time delay is close to 70 photons/pulse, which is more than twice higher than the saturated value of the delayed SHG signal generated by the probe in Fig. 2.7. The signal disappeared as the laser was tuned to the two–photon $4s$–$11s$ transition of K. Input intensity dependence of this SHG signal is given in Fig. 2.10. It shows an intensity dependence of $\sim I^{3.7}$.

2.5 Theory and Discussions

We shall now present in detail the theory of multiphoton–ionization–initiated dc–field–induced resonant SHG in atomic vapor. We shall discuss how the theory explains almost all our observations and in some cases how electric quadrupole contribution to the nonlinearity must be considered.

2.5.1 Time development of the dc field

We first discuss the development of a dc field by multiphoton ionization of atoms in a vapor followed by separation of electrons from ions. Consider tuning of the pump beam to the two–photon $4s$–$9d$ transition of K. In this case, a three–photon absorption of K will excite the atom to 1.9 eV above the ionization level. (See Fig. 2.16.) This means that the three–photon ionization of K will release an electron with an excess kinetic energy of 1.9 eV corresponding to a velocity $v_0 = 8 \times 10^5$ cm/sec.

Assume a picosecond pump pulse with a Gaussian profile and a peak intensity of $\sim 10^{10}\mathrm{W/cm}^2$ tuned to the two–photon $4s$–$9d$ transition of K. The electrons released by three–photon ionization of K should have an initial density distribution

$$N_e(r,0) = \sigma^{(3)} \int I^3(r,t)dt N_e(r,0) \tag{2.6}$$

$$= N \exp(\frac{-r^2}{R_i^2}), \tag{2.7}$$

which equals the initial ion density $N_i(r)$. Here, $\sigma^{(3)}$ is the three–photon ionization cross–section, r denotes the distance from the beam axis, and R_i is $1/\sqrt{3}$ times the pump beam radius. We also treated the picosecond laser pulse as a δ–function pulse. The electrons released by ionization with a finite velocity tend to drift away from the ions, but feel the pull of Coulomb attraction from the ions. In the presence of sufficiently high Ar pressure, the electrons collide frequently with buffer Ar atoms and their motion becomes diffusion–dominated. However, thermalizing collisions with other electrons are rare, so the electrons do maintain

their initial velocity v_0 for a long time. We can therefore assume that electrons released from a three–photon ionization of K by a picosecond pump pulse diffuse radially outward and obey the diffusive equation of motion.

$$\frac{\partial N_e(r,t)}{\partial t} = \nabla \cdot \left(\frac{v_0 L}{3} \nabla N_e(r,t) + \frac{eL}{v_0 m_e} N_e(r,t) \vec{E}_{\rm dc}(r.t) \right), \tag{2.8}$$

where L is the mean free path of electrons [32, 33], m_e is the mass of an electron, and $E_{\rm dc}$ is radially directed. The first term on the right of Eq. (2.8) is the usual diffusive term while the second term is the drift term under the action of $E_{\rm dc}$ that tends to prevent the electrons from diffusing away from the ions. The movement of ions is assumed negligible. Then the dc field resulting from electron–ion separation can be obtained from the Gauss' Law:

$$E_{\rm dc}(r,t) = \frac{4\pi e}{r} \int_0^r \left(N_i(r',0) - N_e(r',t) \right) r' dr', \tag{2.9}$$

in the radial directions. Knowing $N_i(r,0) = N_e(r,0)$, L, and v_0, we can find $E_{\rm dc}$ and $N_e(r,t)$ from Eqs. (2.8) and (2.9).

While the analytical solution of Eqs. (2.8) and (2.9) is difficult to obtain, one can resort to numerical solution to find out the details of the field evolution. It is expected that $E_{\rm dc}$ will grow until it balances the diffusive term in Eq. (2.8). At high levels of ionization, the equilibrium is reached before the electrons could move too much. Thus the equilibrium electron density distribution $N_e(r,\infty)$ for $r < R_i$ is nearly equal to the original distribution $N_e(r,0)$, i.e. $N_e(r,\infty) = N_e(r,0) - \Delta(r)$ with $N_e(r,0) \gg \Delta(r)$. From Eq. (2.8), the equilibrium electric field is given by

$$E_{\rm dc}(r) = \frac{-v_0^2 m_e}{3e} \frac{\frac{\partial}{\partial r}\left(N_e(r,\infty)\right)}{N_e(r,\infty)} \tag{2.10}$$

$$\approx \frac{-v_0^2 m_e}{3e} \frac{\frac{\partial}{\partial r}\left(N_e(r,0)\right)}{N_e(r,0)} = \frac{2v_0^2 m_e r}{3eR_i^2}, \qquad \text{for} \quad r < R_i.$$

Figure 2.11 describes the development of the dc electric field obtained from a numerical calculation using an initial electron density of 3×10^{11} cm^{-3} at $r = 0$ and an initial radius of electron distributions of R_i =170 μm. It is seen that $E_{\rm dc}$ grows until ~200 ps and then gradually saturates to a value of about 0.5 esu. This saturation value agrees fairly well with that predicted by Eq. (2.10). That $E_{\rm dc}$ is proportional to r for $r < R_i$ is also well reproduced by the simulation. Figure 2.12 gives more explicitly the time development of the dc electric field at $r = 200$ μm for two different initial electron densities (hence different laser intensities) of 3×10^{11} cm^{-3} and 10^{12} cm^{-3} at $r = 0$. Note that even if the fields are different at earlier times, the equilibrium value of $E_{\rm dc}$ appears to be the same, independent of $N_e(r,0)$. This is also predicted by the approximation in Eq. (2.10) and was found to be valid for $N_e(r,0) > 10^{11}$ cm^{-3} from the simulation.

In the experiment of SHG in atomic hydrogen, Marmet *et al.* [23] calculated the dc electric field created by the three–photon ionization of hydrogen atoms and found a similar saturation behavior of $E_{\rm dc}$. Their estimated saturation field of several esu seems to agree with the prediction of Eq. (2.10) knowing that their laser beam was focused to about 30 μm. However, the detailed motions of electrons and ions assumed in their simulation were very different from ours; the electron motion was more ballistic than diffusive. The agreement with Eq. (2.10) may be understood from the fact that in both cases the field saturation comes from the pulling action of the ions that keeps the electrons from moving farther away from the ions.

If the SHG does not involve any ionization, we should have a potassium vapor density dependence of N_K^2 as is usually the case for all coherent radiation. However, ionization is necessary for dc–field–induced SHG process, and we expect an additional dependence of SHG on N_K for very low potassium vapor density. When N_e is a number density of electrons from multiphoton ionization, we should have $N_e \propto N_K$. And before the saturation of dc field we expect $E_{\rm dc}$ to be proportional to N_e. As a result, the potassium density dependence of N_K^4 before saturation (Fig. 2.3) can be explained with the additional N_K^2 dependence coming from the dc field.

2.5.2 Generation of second harmonic coherent excitation

Consider SHG in an atomic vapor by a 2 ps pump pulse. Since the buildup of $E_{\rm dc}$ initiated by the pump pulse takes ~100 ps, one would expect the dc–field–induced SHG by the pump pulse itself to be very weak. This is however not what was observed. The reason is that the pump pulse actually excites by two–photon transition a coherent excitation in the atoms that last for ~100 ps or larger. Radiation from this coherent excitation is forbidden because of the selection rule, but becomes allowed in the presence of $E_{\rm dc}$. We discuss here the transient coherent excitation of K atoms by a pulsed two–photon pumping process. With picosecond pump pulses, the pulsewidth is likely to be shorter than the dephasing time of the resonant transition. Coherent transient excitation could result. This is the case of

two–photon excitation of potassium vapor by picosecond pulses. We develop here the formalism, specifically with the $4s$–$9d$ and $4s$–$11s$ transitions in mind.

Consider a two–photon transition from the ground state $|g\rangle$ to an excited state $|f\rangle$ of an atom. The effective Hamiltonian for the transition is known to be [34]

$$\mathcal{H}_{eff} = \sum_{m \neq g} \frac{(eE)^2 x|m\rangle\langle m|x}{\hbar(\omega - \omega_{mg})}, \tag{2.11}$$

where E is the pump field assumed to be polarized along $\hat{x}$, and $\hbar\omega_{mg}$ is the energy difference between $|g\rangle$ and an intermediate state $|m\rangle$. With $\mathcal{H}_{eff}$, we can use the density matrix method to calculate the two–photon excitation. If the pump pulsewidth T_L is much shorter than the dephasing time T_2 of the transition, then immediately after the pump pulse is over, the coherent excitation between $|g\rangle$ and $|f\rangle$ is given by the off–diagonal density matrix element

$$\rho_{fg}(0) = \frac{i}{\hbar}\langle f|\mathcal{H}_{eff}|g\rangle T_L. \tag{2.12}$$

This excitation is expected to decay with time due to dephasing and Doppler effects. We find, for $t > 0$, [27]

$$\begin{aligned} \rho_{fg}(t) &= \rho_{fg}(0)\exp\left(i\omega_{fg}t - \frac{t^2}{T_D^2} - \frac{t}{T_2}\right), \\ T_2 &= \frac{1}{\sqrt{2}v\sigma N_B}, \\ T_D &= \sqrt{\frac{2Mc^2}{k_B T\omega_{fg}^2}}, \end{aligned} \tag{2.13}$$

where T_2 is assumed to be dominated by collisions (e. g., K with Ar in our case), v is the average thermal velocity of the atoms(both K and Ar), σ is the collision

cross section of the excited state [27], N_B is the number density of the buffer atoms (e. g. Ar) assuming that they dominate the collisions, M is the mass of potassium, T is the oven temperature (600°Kinourcase), and $T_D = 190$ ps for the $4s$–$9d$ transition of K.

The oscillating electric dipole created by ρ_{fg} is $p = \langle g|er|f\rangle\rho_{fg}$. Clearly for an atom, p should vanish since if the transition between $|g\rangle$ and $|f\rangle$ is two–photon allowed, it must be one–photon forbidden. Therefore the excitation ρ_{fg} cannot radiate at $2\omega \approx \omega_{fg}$. Perturbation on $\rho_{fg}(t)$ due to mixing of states of different parities can lead to a dc–field–induced polarization

$$\begin{aligned} P_{2\omega}(r,t) &\cong \sum_{np} N_K \frac{e^2\langle g|x|np\rangle\langle np|x|f\rangle}{\hbar(\omega_{np,g} - 2\omega)} E_{\rm dc}(r,t)\rho_{fg}(r,t) \\ &= \sum_{np,mp} N_K \frac{ie^4\langle g|x|np\rangle\langle np|x|f\rangle\langle f|x|mp\rangle\langle mp|x|g\rangle}{\hbar^3(\omega_{np,g} - 2\omega)(\omega - \omega_{mp,g})} \\ &\quad \times E(r,0)^2 E_{\rm dc}(r,t) \exp\left(i\omega_{fg}t - \frac{t^2}{T_D^2} - \frac{t}{T_2}\right) T_L. \end{aligned} \tag{2.14}$$

The generated SH signal is proportional to the square of $P_{2\omega}(r,t)$ and can be calculated if all the relevant parameters are known. It is seen that $P_{2\omega}$, and hence the SHG, can be significant as long as $E_{\rm dc}$ and ρ_{fg} overlap appreciably in space and time. This is the case with picosecond two–photon resonant excitation of atoms, since both $E_{\rm dc}$ and ρ_{fg} are initiated by the pump pulse and both remain significant on the 100 ps time scale. The above theory can be tested by our experiment on K/Ar vapor. In the pump–only experiment, the variables can be the pump intensity and the Ar buffer pressure. At a fixed pump intensity, we can vary the Ar pressure and look for the change in SHG.

Figure 2.13 is the time development of $E_{\rm dc}$ and ρ_{fg} for two different Ar pressures. Not only the tail of ρ_{fg} is reduced at high Ar pressure due to collision broadening, but also the $E_{\rm dc}$ is seen to develop a bit more slowly since increased Ar pressure hinders the diffusion of electrons from ionization. As expected, the higher Ar pressures results in less overlapping between $E_{\rm dc}(r,t)$ and $\rho_{fg}(r,t)$, and hence a weaker SHG. (The SHG signal is proportional to the the square of the common area under the curves of $E_{\rm dc}$ and ρ_{fg} in Fig. 2.13). A full calculation of SHG versus Ar pressure is presented in Fig. 2.6 in comparison with the experimental data for two different laser intensities. At the higher laser intensity, $E_{\rm dc}$ reaches the equilibrium value in a time fast compared to either T_2 or T_D regardless of the Ar pressure and SHG decreases with Ar pressure mainly due to shortening of the coherent decay, $\rho_{fg} \propto e^{-t/T_2} \propto e^{-\alpha t P_{Ar}}$, where α is a constant. In this case, we have roughly $SHG \propto \int_0^\infty |\rho_{fg}(t')|^2 dt'$, so we can expect a $1/P_{Ar}$ dependence of SHG. At the lower laser intensity where the buildup time of $E_{\rm dc}$ is comparable with T_2 or T_D, increasing the Ar pressure decreases the SHG in two ways. First, SHG is reduced by the faster decay of ρ_{fg} at higher Ar pressure as in the high intensity case. Second, as the tail of ρ_{fg} shrinks with higher Ar pressure, it samples the earlier part and hence the weaker part of $E_{\rm dc}$ in the build-up. Altogether we expect a smaller SHG signal that decreases faster than $1/P_{Ar}$ in the high pump intensity case. The solid lines in Fig. 2.6 are obtained from numerical simulation taking both effect into account and they appear to describe the experimental data very well. Recently, this SHG due to atomic coherence ρ_{fg} has also been confirmed

nicely by Brownell *et al.* [35] in the time–delayed SHG experiment in Cs vapor.

As for the pump intensity dependence, the above result on second harmonic coherence together with the development of E_{dc} can be used to explain the observed different pump intensity dependences of SHG in atomic vapor by nanosecond [8, 9, 13, 14] and picosecond pump pulses. In both cases, the levels of ionization were high enough for the approximation in Eq. (2.10) to work. However, it takes typically $\sim$ 100 ps for E_{dc} to reach equilibrium. This is short on the nanosecond scale. Therefore for a nanosecond pump pulse E_{dc} should have reached the constant equilibrium value given by Eq. (2.10) during most of the pulse duration. The numerical calculation of $E_{dc}(t)$ is shown in Fig. 2.14 for the case of a 15 ns pump pulse with a 0.1 cm^{-1} linewidth tuned to the $4s$–$9d$ two–photon resonance of potassium vapor. From Fig. 2.14(a), saturation of $E_{dc}(t)$ at pump intensities greater than 10 MW/cm^2 is clearly seen. As a result, the dc–field–induced SHG should be given by $I(2\omega) \propto |E_{dc}|^2 I(\omega)^2 \propto I(\omega)^2$ as was indeed observed in previous experiments [8, 9, 11, 13]. Calculated input intensity dependence of SHG for nanosecond laser pulses is shown in Fig. 2.15. In the figure, SHG is proportional to I^8 at low pump intensities, but soon changes to the I^2 dependence as the higher pump intensity brings the dc field into saturation. For a picosecond pump pulse, however, the dc–field–induced SHG occurs at the rising part of E_{dc}. Since $E_{dc}(r,t)$ is proportional to $I(\omega)^3$ during the build–up, we find $I(2\omega) \propto I(\omega)^8$, as was observed and shown in Fig. 2.4.

At higher pump intensities, the degree of ionization of atoms increases and the

dc field is expected to saturate earlier. The dc–field–induced SHG may partly occur after E_{dc} saturates. In that case, the SHG signal should deviate from I^8 towards high pump intensities as shown in Fig. 2.4. The theory here applies to SHG resonant with the $4s$–$9d$ transition as well as that with the $4s$–$11s$ transition. As seen in Fig. 2.4, both display an I^8 dependence at low I and a weakly saturated behavior at large I.

2.5.3 Pump–probe experiment

Since E_{dc} from multiphoton ionization is built up on a time scale longer than the laser pulsewidth, we can employ a pump–probe scheme to test the model. The picosecond pump and probe pulses can be used to create the $E_{dc}(r,t)$ and $\rho_{fg}(r,t)$, respectively. By varying the time delay between the two pulses, the time overlap between $E_{dc}(r,t)$ and $\rho_{fg}(r,t)$ can be adjusted and the SHG signal changes accordingly. The SH signal as a function of the time delay can be calculated from the equations given earlier. The calculated result of SHG as a function of the pump-probe time delay is plotted in Fig. 2.7 to compare with the experimental result. It is seen that if the probe pulse is too far ahead of the pump pulse (negative time delay), the signal is negligibly small as expected. As the pulses get closer, $\rho_{fg}(t)$ generated by the probe overlaps more with $E_{dc}(t)$ generated by the pump, and the dc–field–induced SHG becomes stronger. Because the tail of $\rho_{fg}(t)$ extends over a dephasing time to overlap with $E_{dc}(t)$, an appreciable SHG signal can still be produced with the probe pulse proceeding the pump pulse.

Eventually, for sufficiently long positive time delays, $\rho_{fg}(t)$ moves completely under the saturated region of $E_{\rm dc}(t)$ (see Fig. 2.13), and the SH signal saturates accordingly. The signal remains nearly unchanged between delays of 100 psec and 600 psec which is the limit of this experiment. In Fig. 2.7, the results for pump intensities of 12 and 8 GW/cm^2 are shown. The higher pump intensity is expected to bring $E_{\rm dc}(t)$ more rapidly to saturation. This is reflected in the faster growth of the SH signal to saturation. As seen in Fig. 2.7, the agreement between theory and experiment is quite satisfactory, considering the simplicity of the model. The observed bump between delay times 10 and 100 psec was not reproduced in the theoretical curve. This could be due to the fact that we have neglected the non–diffusive or ballistic aspect of the electron motion during the initial period right after the electrons are released by multiphoton ionization. Presumably before the electrons experience a sufficient number of collsions, the diffusion equation is not expected to be fully valid because the overall direction of electron motion is not yet random.

If the probe beam is only effective in creating ρ_{fg} but not affecting $E_{\rm dc}$, we should expect to see an $I^2_{\rm probe}$ dependence of the SH signal. Figure 2.8 shows that this is indeed the case. Clearly in our case, $E_{\rm dc}$ was induced mainly by the pump beam.

When the pump and probe beams are overlapped in time a well–collimated SHG signal was also observed midway between the pump and probe beam directions. As shown in Fig. 2.9, the measured cross correlation curve has a peak somewhat narrower than the autocorrelation trace of the laser pulse obtained with a

nonlinear crystal. The peak intensity is about 70 photons/pulse. This temporal characteristic of the SHG is very different from that of the dc–field–induced SHG discussed earlier in this section.

Since the SH signal vanished when the laser was tuned to the two–photon $4s$–$11s$ transition, we suspect that quadrupole nonlinearity is responsible for the SHG in this case. A similar sum–frequency generation process was reported earlier by Bethune *et al.* [7] in sodium vapor. The quadrupolar nonlinear optical susceptibility $\chi_Q^{(2)}$ of potassium vapor was already calculated in Sec. 2. For a vapor density of $N = 10^{16}$ /cm^3, $\chi_Q^{(2)}$ for the $4s$–$9d$ resonant transition was estimated to be 2×10^{-18} esu. With an input intensity 5 GW/cm^2 for the pump and probe beams and an angle of $\sim$0.2° between the two beams, the estimated SH signal is about $\sim$10 photons/pulse, which is within an order of magnitude of the observed SH signal.

Although the above estimate is in favor of the SHG due to quadrupole nonlinearity, some of our results appear anomalous. The theory of SHG by quadrupole nonlinearity predicts that the output should have an I^2 pump intensity dependence and should vanish when the pump and probe beams are polarized along the same direction. Our experiment however showed that the output was proportional to $\sim I^{3.7}$ (Fig. 2.10) and did not completely vanish when the polarizations of the pump and probe are made parallel. The discrepancy may come from the fact that this SHG also has a dc–field–induced component although it is estimated to be weak, namely, about 20 % in field amplitude of SHG from the quadrupole non-

linearity at a pump intensity of $\sim$20 GW/cm^2. In this case, the dc–field–induced part also exists only if the pump and probe pulses overlap in time. More explicitly, we have the SHG output given by

$$\begin{aligned} S(2\omega) &\propto |\vec{P}_Q(2\omega) + \vec{P}_{\rm dc}(2\omega)|^2 \\ &= |\vec{P}_Q(2\omega)|^2 + 2{\rm Re}(\vec{P}_Q(2\omega)\cdot\vec{P}_{\rm dc}(2\omega)) + |\vec{P}_{\rm dc}(2\omega)|^2, \end{aligned} \tag{2.15}$$

where $\vec{P}_Q$ and $\vec{P}_{\rm dc}$ are nonlinear polarizations due to χ_Q and dc–field–induced SHG effect, respectively. With $\vec{P}_Q$ vanishing as in the $4s$–$11s$ case, SHG from $\vec{P}_{\rm dc}$ only may be too weak to be detected. With $\vec{P}_Q$ nonvanishing as in the $4s$–$9d$ case, and $\vec{P}_{\rm dc}$ being appreciable in comparison with $\vec{P}_Q$, the pump intensity dependence of SHG could be significantly modified by $\vec{P}_{\rm dc}$, yielding the observed $I^{3.7}$ instead of the I^2 dependence expected from $\vec{P}_Q$ alone.

2.5.4 Details of the SHG output

Since all the matrix elements in Eq. (2.14) are known from Ref. [25], we can calculate the SHG output quantitatively. The SHG intensity related to $P_{2\omega}(r,t)$ is given by Ref. [4].

$$I(2\omega) = \frac{8\pi\omega^2}{cn(2\omega)}|P(2\omega)|^2\left(\frac{\sin(\Delta kz/2)}{\Delta kz/2}\right)^2 z^2, \tag{2.16}$$

where $\Delta k = 2k(\omega) - k(2\omega)$ is the phase mismatch between the fundamental and the second harmonic waves, and z is the interaction length of the two beams in the medium. In this equation, $P(2\omega)$ is a function of both time and space. To find the SH output signal, we must integrate $I(2\omega)$ in both time and space.

To estimate the amount of SHG, there are several approximations we can make to ease the calculation. The atomic level diagram of potassium is shown in Fig. 2.16. We consider $4s$–$9d$ resonant SHG. The linewidth of our picosecond pulse was 7 cm^{-1} and the linewidth of the $4s$–$9d$ transition of K at 0.6 Torr K and 20 Torr Ar is 0.2 cm^{-1}. Contribution from $4s$– $11s$ is negligible as the transition is 26 cm^{-1} away. About the intermediate states in $P(2\omega)$ of Eq. (2.14), we only need to include $4p$, $10p$, and $11p$ levels in the summation since other p states give a negligible contribution either because they are sufficiently detuned from the laser frequency or because the oscillation strength is too small. About phase matching in the vapor, the dielectric constant of the potassium vapor at 2ω is larger than that in ω and the medium is not phase matched. Index mismatch $\Delta n = n(\omega) - n(2\omega)$ of the vapor can be calculated from the Sellmeier equation and found to be 3.5×10^{-6} at 0.6 torr of K. From this, the coherence length of SHG in the vapor is estimated to be $z = 4$ cm. Using the above simplifications, we can calculate $P(2\omega)$ and $I(2\omega)$ and then integrate $I(2\omega)$ over time and space. From the perturbation calculation, a 10 GW/cm^2 laser pulse tuned to the $4s$–$9d$ two–photon transition can bring 1.4×10^{-2} of the potassium atoms to the excited state, and about 1.2×10^{-3} of them ionized. From Eqs. (2.14) and (2.16), we then estimate a SHG signal of $\sim$700 photons/pulse. This number is within an order of magnitude of the observed SHG of $\sim$100 photons/pulse. The disagreement can come from: (1) simplifications made in the calculation, and (2) error in measuring the input intensity of the laser (Since SHG in our experiment is a very steep

function of input intensity, a 20 % error in the input intensity measurement can lead to more than 400 % error in the SHG signal.).

The resonant SHG observed at the $4s$–$10p$ transition was much weaker. However, it still cannot be explained by all the other proposed machanisms reviewed in Sec. 2 B. For example, quadrupole matrix elements associated with the input field $\vec{E}_1(\vec{k}_1, \omega)$ yield a nonlinear polarization of the form

$$\vec{P}(2\omega) = \chi_1 \vec{k}_1(\vec{E}_1 \cdot \vec{E}_1) + \chi_2 \vec{E}_1(\vec{k}_1 \cdot \vec{E}_1) \tag{2.17}$$

where χ_1 and χ_2 are independent coefficients. Since $\vec{k}_1 \perp \vec{E}_1$, the second term vanishes. As for the first term, the nonlinear polarization is in the beam propagation direction and cannot radiate. In the real case where the pump beam is focused, SHG strictly does not vanish, but as shown in Sec. 2 B. 2, is expected to be very small.

We then consider again the dc–field–induced machanism. Here, it is clearly different from the $4s$–$9d$ case. In the latter case, the two–photon coherent excitation between $4s$ and $9d$ is first established by the pump pulse, but is allowed to radiate only with the help of $E_{\rm dc}$. For the $4s$–$10p$ case, the radiative transition between $10p$ and $4s$ is electric–dipole–allowed, but the two–photon coherent excitation between $10p$ and $4s$ must be set up by the $E_{\rm dc}$–induced dipole–dipole pathway. (The dipole–quadrupole pathway establishes a two–photon coherent excitation that cannot produce SHG as mentioned above.) Thus $E_{\rm dc}$ and the pump field $E(\omega)$ must overlap in time.

To estimate the multiphoton–ionization induced E_{dc} in the $4s$–$10p$ case, we first calculate two–photon excitation into the $10p$ state. This process is expected to be much less efficient than that into the $9d$ state because it must take the dipole–quadrupole (or quadrupole–dipole) pathway. Comparison of various dipole and quadrupole matrix elements for various transitions [25, 26] shows that the $4s$–$3d$–$10p$ excitation pathway contributes the most to the two–photon $4s$–$10p$ excitation ($\langle 4s|r^2|3d\rangle = 2\times 10^{-15}$ cm^2 from Ref. [26]). With a pump intensity of 20 GW/cm^2 and a pump pulsewidth of 15 ps, we find the two–photon transition probability to $10p$ is $\sim 10^{-3}$. In comparison, for the $4s$–$9d$ transition with the same experimental conditions, about 40 % of the atoms would be excited to the $9d$ state. Since the one–photon ionization rate from $10p$ is not too much different from that of $9d$, we expect that in the $4s$–$10p$ case, about 10^{-3} less electrons are released by ionization with the same pump intensity. This is consistent with the earlier observations [14, 15] where hardly any multiphoton ionization from excitation via the np state was seen while those from the ns and nd states could be easily detected. From this estimate, we would expect that E_{dc} in the $4s$–$10p$ case should be about 3 orders of magnitude smaller than in the $4s$–$9d$ case. However, this difference can be significantly reduced if E_{dc} in the latter case saturates. With the 15 ps, 20 GW/cm^2 pump pulse, we find from calculation that $\sim 10^{13}$ cm^{-3} of electrons would be released by three–photon ionization via the $4s$–$9d$ transition and E_{dc} would reach in $\sim$5 ps its saturation value of 0.5 esu predicted by Eq. (2.10). With the same pump intensity tuned to the two–photon $4s$–$10p$ transition, E_{dc}

generated would reach only ~0.08 esu at the end of the pump pulse. Knowing how $E_{\rm dc}$ induces SH radiation from the two–photon nonradiative coherent excitation in the $4s$–$9d$ case but helps set up the radiative two–photon coherent excitation in the $4s$–$10p$ case, we can estimate SHG for the two cases. We find that SHG from the $10p$ state should be about 2–3 orders of magnitude smaller than that from the $9d$ state considering that the dephasing times of $4s$–$9d$ and $4s$–$10p$ coherences are comparable. This is in crude agreement with the experimental observation.

Since the radial dependences of ρ_{fg} and $E_{\rm dc}$ can be calculated from the pump beam profile, we can also determine the spatial profile of the $4s$–$9d$ SHG output. Following Bethune [18], the second harmonic polarization for dc–field–induced SHG can be written as

$$\vec{P}(2\omega) = \chi_a \vec{E}(\omega)\left(\vec{E}(\omega)\cdot\vec{E}_{\rm dc}\right) + \chi_b \vec{E}_{\rm dc}\left(\vec{E}(\omega)\cdot\vec{E}(\omega)\right), \qquad (2.18)$$

where χ_a and χ_b are the two independent components of the nonlinear susceptibility tensor for dc–field–induced SHG. Since the laser field is linearly polarized and has a Gaussian profile, $\vec{E}(\omega) = E_0 e^{-r^2/R^2}\hat{y}$, and the dc field is linear in r with a cylindrical symmetry (Fig. 2.11), $\vec{E}_{\rm dc} = E_{\rm dc}\hat{r}$, we find

$$\vec{P}(2\omega) = \chi_b E_0^2 E_{\rm dc} \exp\left(-2r^2/R^2\right)\left[\frac{x}{r}\hat{x} + (a+1)\frac{y}{r}\hat{y}\right], \qquad (2.19)$$

$$|\vec{P}(2\omega)|^2 = \chi_b^2 E_0^4 E_{\rm dc}^2 \exp\left(-4r^2/R^2\right)\left[\frac{x^2}{r^2} + (a+1)^2\frac{y^2}{r^2}\right], \qquad (2.20)$$

where $a = \chi_a/\chi_b$, and $(a+1)^2$ is the ratio of SHG polarization $(|P_y(2\omega)|^2/|P_x(2\omega)|^2)$.

Our measurement of the ratio of SHG outputs polarized along $\hat{y}$ and $\hat{x}$ yields $(a+1)^2 = 16$. We can then calculate the spatial profile of the SHG output from Eq. (2.20). This is plotted in Fig. 2.17. The result is compared with the measured SHG profile in Fig. 2.5. The solid lines in Fig. 2.5 are obtained from integration of the two–dimensional curve in Fig. 2.17 along vertical and horizontal directions to simulate the effect of a narrow slit used in the measurement to scan the spatial profile. The agreement between theory and experiment is good. The deviation may come from the fact that the input beam profile was not perfectly Gaussian. The experimentally deduced value of $(a+1)^2 = 16$ implies that either $\chi_a = 3\chi_b$ or $\chi_a = -5\chi_b$. However, calculation of χ_a and χ_b for the $4s$–$9d$ resonant SHG in K yields $\chi_a = -3\chi_b$ [18]. This discrepancy unfortunately is not understood. Similar measurements on resonant SHG from a set of different two–photon transitions will probably help solve the problem.

2.6 Summary and Conclusions

We have studied two–photon resonant SHG from potassium vapor using tunable picosecond pulses. We show that the multiphoton–ionization–initiated dc–field–induced SHG is the mechanism responsible for the observed resonant SHG. This mechanism explains the observed strong input intensity dependence of I^8 before saturation. Detailed investigation was carried out around the two–photon $4s$–$9d$ transition. The ultrashort laser pulse set up via two–photon pumping a transient

coherent excitation between $4s$ and $9d$, and generates via three–photon ionization a dc electric field in the medium. Radiation from the $4s$–$9d$ coherent excitation is normally electric–dipole forbidden, but the presence of the dc field make it allowed. We have calculated numerically the time developments of the dc field buildup, the coherent excitation, and then the resonant SHG output. The results satisfactorily explain the experimental observations on the gas pressure dependence of SHG and the time–delayed SHG signal in a pump–probe experiment. Saturation of the dc field is shown to be the reason behind the anomalous results obtained in previous experiments using nanosecond pulses, such as I^2 dependence of SHG and the missing correlation between ionization and SHG. We have also studied the spatial profile and polarization dependence of the SHG output and the resonant SHG around $4s$–$11s$ and $4s$–$10p$ transitions. The results can also be well explained by multiphoton–ionization–initiated dc–field–induced mechanism of SHG. An SHG output along the direction bisecting the pump and probe beams has also been observed and is identified as resulting mainly from quadrupole nonlinearity.

Bibliography

[1] D. C. Hanna, M. A. Yuratich, and D. Cotter, *Nonlinear Optics of Free Atoms and Molecules* (Springer–Verlag, Berlin, 1979) and references therein.

[2] R. T. Hodgson, P. P. Sorokin, and J. J. Wynne, Phys. Rev. Lett. **32**, 343–346 (1974); P. P. Sorokin, J. J. Wynne, and J. R. Lankard, Appl. Phys. Lett. **22**, 342–344 (1973).

[3] J. L. Carlsten and T. J. McIlrath, J. Phys. B **6** , L80–L85 (1973).

[4] See, for example, Y. R. Shen, *The Principles of Nonlinear Optics* (John Wiley & Sons, New York, 1984).

[5] D. L. Andrews, Phys. Rev. A **38**, 3113–3115 (1988); T. F. Heinz and D. P. DiVincenzo, Phys. Rev. A **42**, 6249–6251 (1990).

[6] P. S. Pershan, Phys. Rev. 130, 919–929, (1963).

[7] D. S. Bethune, R. W. Smith, and Y. R. Shen, Phys. Rev. Lett. **37**, 431–434 (1976); Phys. Rev. A **17**, 277–292 (1978).

[8] T. Mossberg, A. Flusberg, and S.R. Hartmann, Opt. Commun. **25**, 121–124 (1978).

[9] J. Okada, Y. Fukuda, and M. Matsuoka, J. Phys. Soc. Jpn. **50**, 1301–1309 (1981).

[10] J. Bokor, R. R. Freeman, R. L. Panock, and J. C. White, Opt. Lett. **6**, 182–184 (1981).

[11] R. R. Freeman, J. E. Bjorkholm, R. Panock, and W. E. Cooke, *Laser Spectroscopy V*, edited by A. R. W. McKellar, T. Oka, and B. P. Stoicheff (Springer-Verlag, Berlin, 1981), p. 453–457.

[12] W. Jamroz, P. E. LaRocque, and B. P. Stoicheff, Opt. Lett. **7**, 148–150 (1982).

[13] S. Dinev, J. Phys. B **21**, 1681–1697 (1988); S. Dinev, J. Phys. B **21**, 1111–1119 (1988).

[14] M. Lu and J. Tsai, J. Phys. B **23**, 921–935 (1990).

[15] J. Y. Zhang, H. T. Zhou, and P. Jin, *Resonance Ionization Spectroscopy 1988*, edited by T. B. Lucatorto and J. E. Parks (Institute of Physics, Bristol and Philadelphia, 1989), p. 29–32.

[16] A. Elçi and D. Depatie, Phys. Rev. Lett. **60**, 688–691 (1988).

[17] S. Vianna, and C. de Araujo, Phys. Rev. A **44**, 733–736 (1991).

[18] D. S. Bethune, Phys. Rev. A **23**, 3139–3151 (1981).

[19] C. S. Mullin, D. Kim, M. B. Feller, and Y. R. Shen, Phys. Rev. Lett. **74**, 2678–2681 (1995); D. Kim, C. S. Mullin, and Y. R. Shen, Appl. Phys. B **60**, S215–S220 (1995); D. Kim, C. S. Mullin, and Y. R. Shen, *Laser Spectroscopy*,

edited by M. Inguscio, M. Allegrini, and A. Sasso (World Scientific, Singapore, 1996), p. 337–340.

[20] K. Miyazaki, T. Sato, and H. Kashiwagi, Phys. Rev. Lett. **43**, 1154–1157 (1979).

[21] M. S. Malcuit, R. W. Boyd, W. V. Davis, and K. Rzążewski, Phys. Rev. A **41**, 3822–3825 (1990).

[22] K. Hakuta, L. Marmet, and B. P. Stoicheff, Phys. Rev. Lett. **66**, 596–599 (1991); L. Marmet, K. Hakuta, and B. P. Stoicheff, Opt. Lett. **16**, 261–263 (1991).

[23] L. Marmet, K. Hakuta, and B. P. Stoicheff, J. Opt. Soc. Am. B **9**, 1038–1046 (1992).

[24] J. C. MacGillivray and M. S. Feld, Phys. Rev. A **14** , 1169–1189 (1976).

[25] R. B. Miles and S. E. Harris, IEEE J. Quantum Electron. **QE–9**, 470–484 (1973); H. Eichner, IEEE J. Quantum Electron. **QE–11**, 121–130 (1975); W. L. Wiese, M. W. Smith, and B. M. Miles, *Atomic Transition Probabilities, Sodium through Calcium* (National Bureau of Standards, Washington, D. C. 1969), p. 225.

[26] B. Warner, Mon. Not. R. Astron. Soc. **139**, 115–128 (1968).

[27] T. F. Gallagher, S. A. Edelstein, and R. M. Hill, Phys. Rev. A **15**, 1945–1951 (1977); A. Flusberg, R. Kachru, T. Mossberg, and S. R. Hartmann, Phys. Rev. A **19**, 1607–1621 (1979).

[28] S. Augst, D. D. Meyerhofer, C. I. Moore, and J. Peatross, *Femtosecond to Nanosecond High-Intensity Lasers and Applications*, Proceedings of SPIE **1229**, edited by E. M. Campbell (SPIE, Bellingham, 1990), p. 152–158.

[29] M. Matsuoka, H. Nakatsuka, and J. Okada, Phys. Rev. A **12**, 1062–1065 (1975).

[30] C. R. Vidal and J. Cooper, J. Appl. Phys. **40**, 3370–3374 (1969).

[31] J. Y. Zhang, J. Y. Huang, Y. R. Shen, and C. Chen, J. Opt. Soc. Am. B **10**, 1758–1764 (1993).

[32] D. E. Golden and H. W. Bandel, Phys. Rev. **149**, 58–59 (1966).

[33] A. Kasden, T. M. Miller, and B. Bederson, Phys. Rev. A **8**, 1562–1569 (1973).

[34] D. Grischkowsky, M. M. T. Loy, and P. F. Liao, Phys. Rev. A **12**, 2514–2533 (1975).

[35] J. H. Brownell, X. Lu, and S. R. Hartmann, Phys. Rev. Lett. **75**, 3657–3660 (1995).

Figure Captions

Figure 2.1: Experimental setup. PD 1: reference photodiode; BS: beamsplitter; PMT: photomultiplier tube; GI: gated integrator.

Figure 2.2: Output spectrum from the K/Ar vapor obtained with the laser frequency tuned to the two–photon $4s$–$9d$ resonance. The middle peak at 2978.7 Å is the true resonant SHG signal. The peak at 2976.3 Å comes from the residual $11s$–$4s$ transition and the peak at 2993.0 Å from the $10p$–$4s$ transition in a four–wave–mixing process.

Figure 2.3: Second harmonic signal as a function of potassium vapor density in the K/Ar mixture. The dashed line describes an N_K^4 dependence.

Figure 2.4: Second harmonic signal as a function of pump intensity I (a) at the $4s$–$9d$ resonance, and (b) at the $4s$–$11s$ resonance. The straight line denotes an I^8 dependence.

Figure 2.5: Spatial profile of SHG measured by scanning a 100 μm slit (a) horizontally, and (b) vertically over the output beam. The theoretical curves (solid lines) are shown for comparison.

Figure 2.6: Dependence of SHG on Ar pressure in a mixture with 0.6 Torr of potassium. The pump intensities used are 13 GW/cm^2 (squares) and 7.5 GW/cm^2 (circles). The lines are obtained from theoretical calculation.

Figure 2.7: SHG generated by the probe pulse as a function of time delay between the pump and probe pulses. Squares: pump intensity at 12 GW/cm^2. Circles: pump intensity at 8 GW/cm^2. The lines are theoretical fits. The build-up time of E_{dc} is ~30 ps (for the upper curve) and ~150 ps (for the lower curve).

Figure 2.8: Second harmonic signal as a function of probe intensity when the pump intensity is held fixed. The vapor mixture has 0.6 Torr of K and 20 Torr of Ar, and the probe pulse is delayed by 100 ps from the pump pulse. The straight line denotes an I^2 dependence.

Figure 2.9: (a) Cross–correlation traces of SHG between pump and probe pulses from the $4s$–$9d$ (crosses) and $4s$–$11s$ (circles) resonances. Dotted line is a fit to the $4s$–$9d$ data with a FWHM (full–width at half–maximum) of 2.6 ps. (b) Autocorrelation trace of SHG from an LBO crystal. The dotted line is a theoretical fit to the data with a FWHM of 4.1 ps.

Figure 2.10: Input intensity dependence of SHG at the peak of the cross–correlation trace of the $4s$–$9d$ case shown in Fig. 9. The solid line is proportional to $I^{3.7}$.

Figure 2.11: Calculated dc electric field $E_{dc}(r,t)$ generated by three–photon ionization of K with a 2 ps laser pulse. Initial electron density is 3×10^{11} cm^{-3}.

Figure 2.12: Calculated time development of E_{dc} at $r = 200$ μm for two different initial electron densities of 3×10^{11} cm^{-3} (solid line) and 10^{12} cm^{-3} (dotted line).

Figure 2.13: Time development of E_{dc} (solid curve) and ρ_{fg} (dashed curve) for (a) 10 Torr, and (b) 50 Torr of Ar pressure at $I(\omega) = 10$GW/cm^2 and $r = 200$ μm.

Figure 2.14: Numerical simulation of E_{dc} for several different input intensities of nanosecond pulses. (a) For higher laser intensities where normal I^2 dependence of SHG can be observed. Dotted line is a time profile of the laser intensity shown as a comparison. (b) For lower intensities where I^8 input intensity dependence should be seen.

Figure 2.15: Calculation of SHG vs input intensity for nanosecond laser pulses two–photon tuned to the $4s$–$9d$ of potassium. SHG depends on I^2 except for the low input intensities where it shows an I^8 dependence. Ar pressure was set to 20 Torr and the initial electron radius was 170 μm.

Figure 2.16: Partial energy level diagram of potassium. The energy levels are not to scale. Fine structures of atomic levels are not resolved in the experiment.

Figure 2.17: Calculated spatial profile of the SHG output. The radius of the input beam and the ratio of SHG horizontal to vertical polarization ($S_{\|}/S_{\perp}$) are obtained from the experiment. The input beam shape is assumed to be Gaussian.

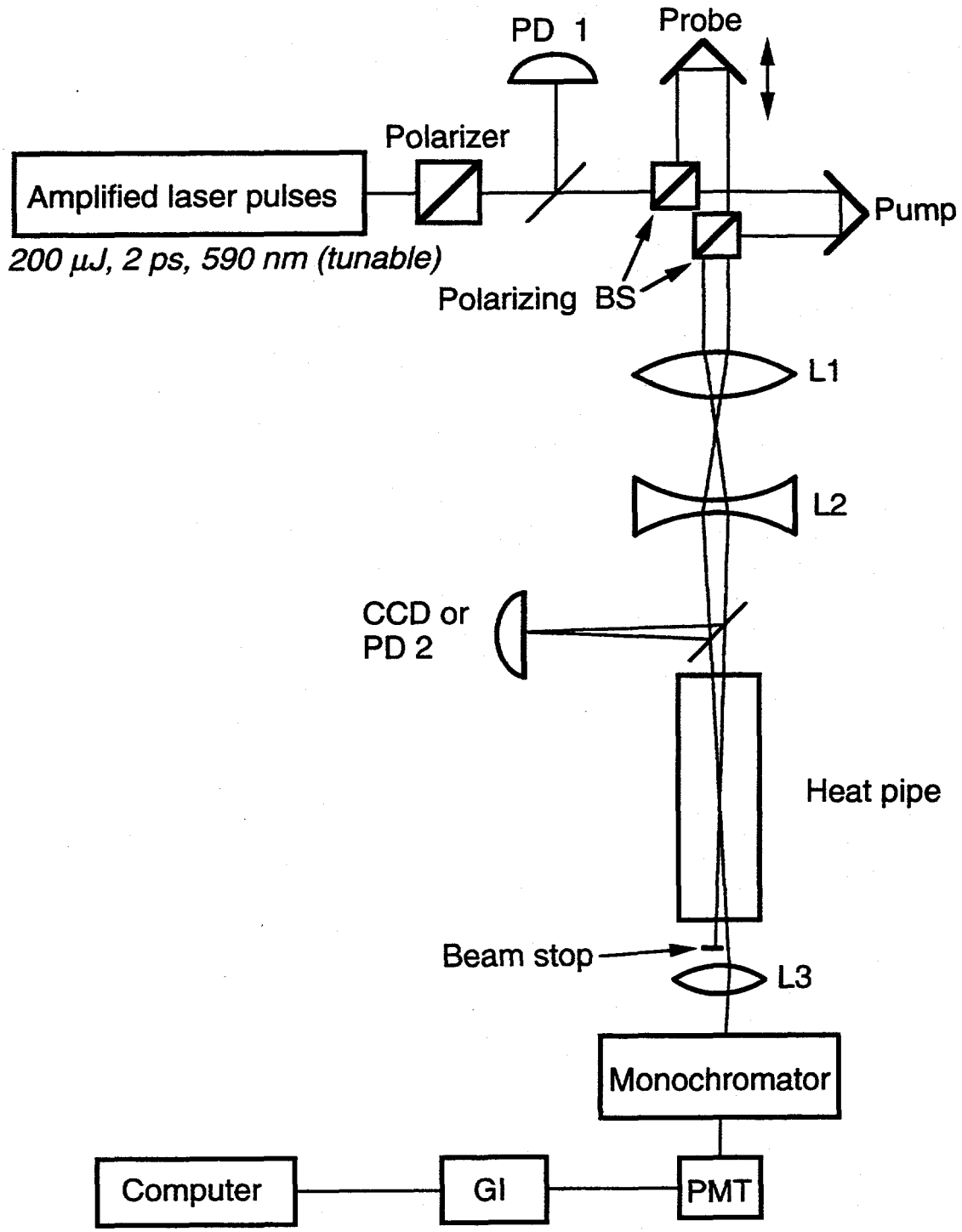
PD 1
Probe
Polarizer
Amplified laser pulses
200 μJ, 2 ps, 590 nm (tunable)
Pump
Polarizing BS
L1
L2
CCD or
PD 2
Heat pipe
Beam stop
L3
Monochromator
Computer
GI
PMT

Fig. 1

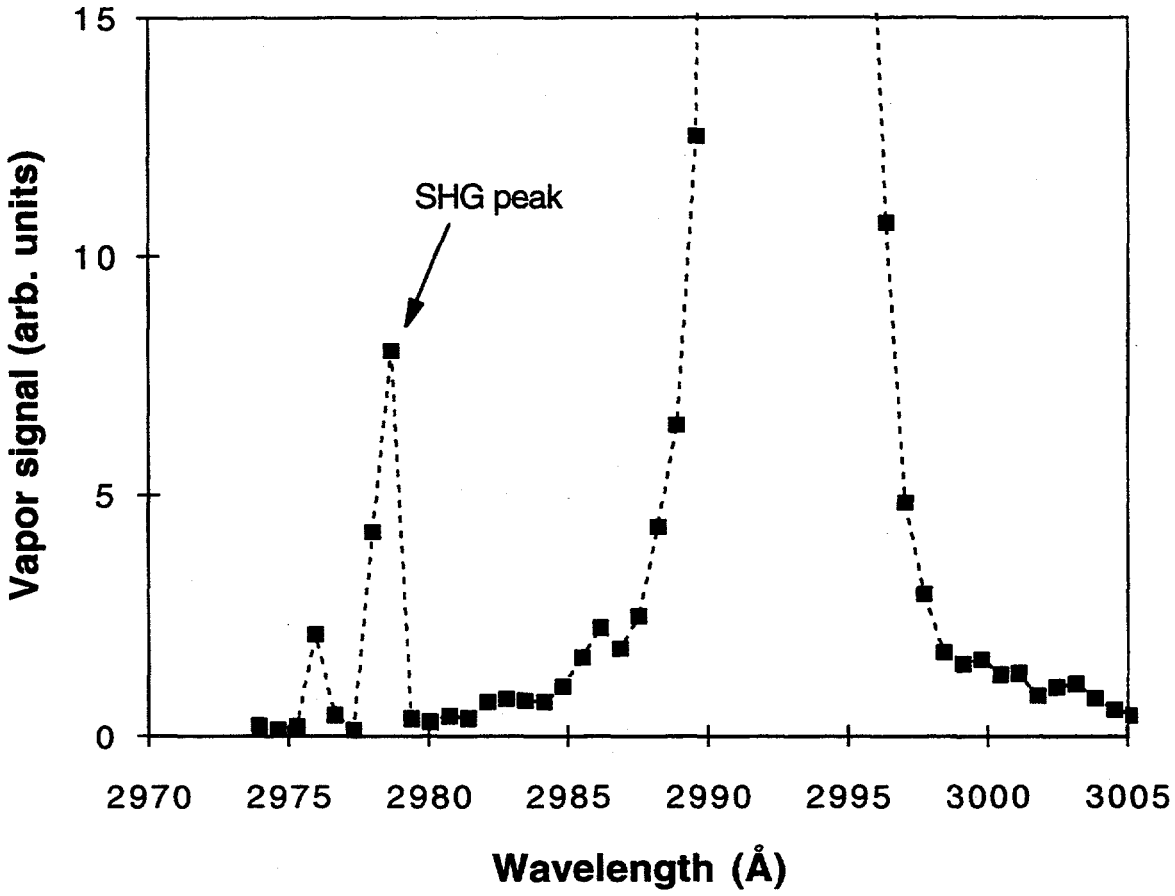
15
10
5
0
Vapor signal (arb. units)
SHG peak
2970
2975
2980
2985
2990
2995
3000
3005
Wavelength (Å)

Fig. 2

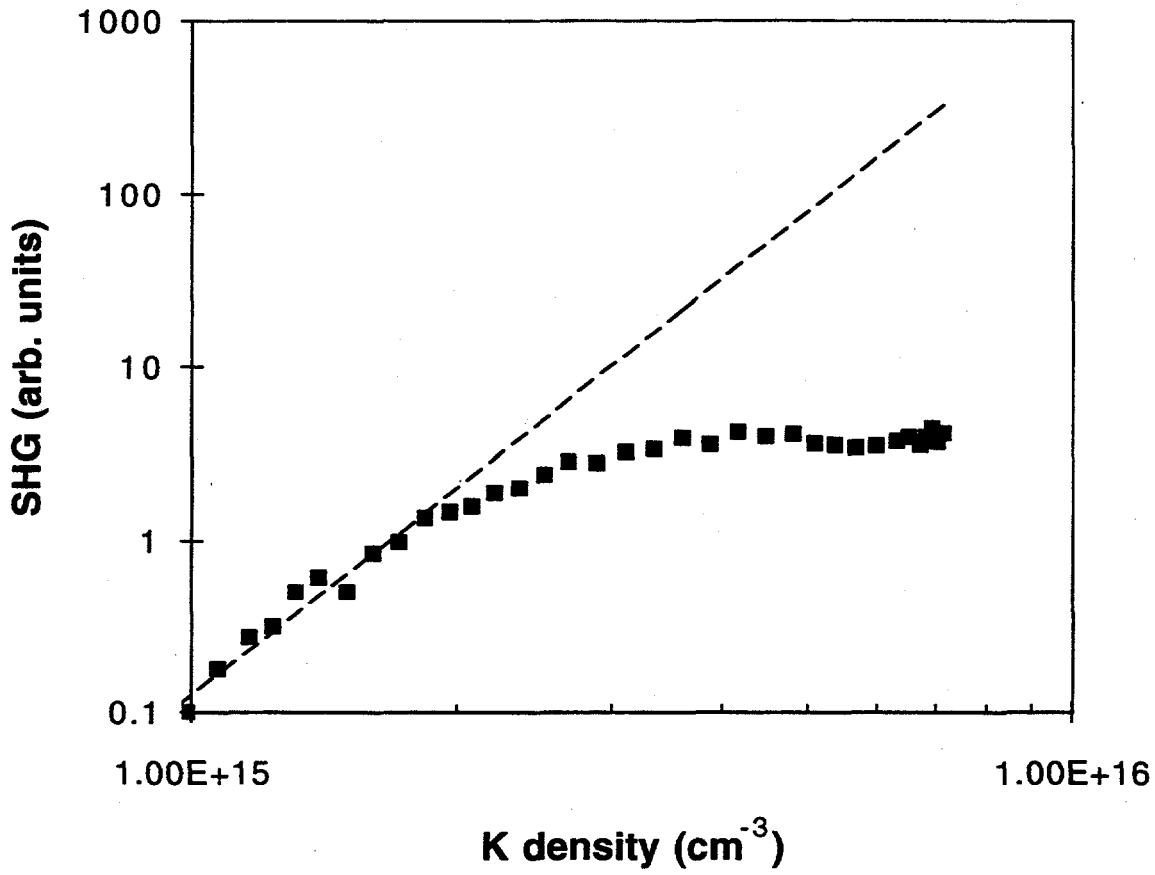

Fig. 3

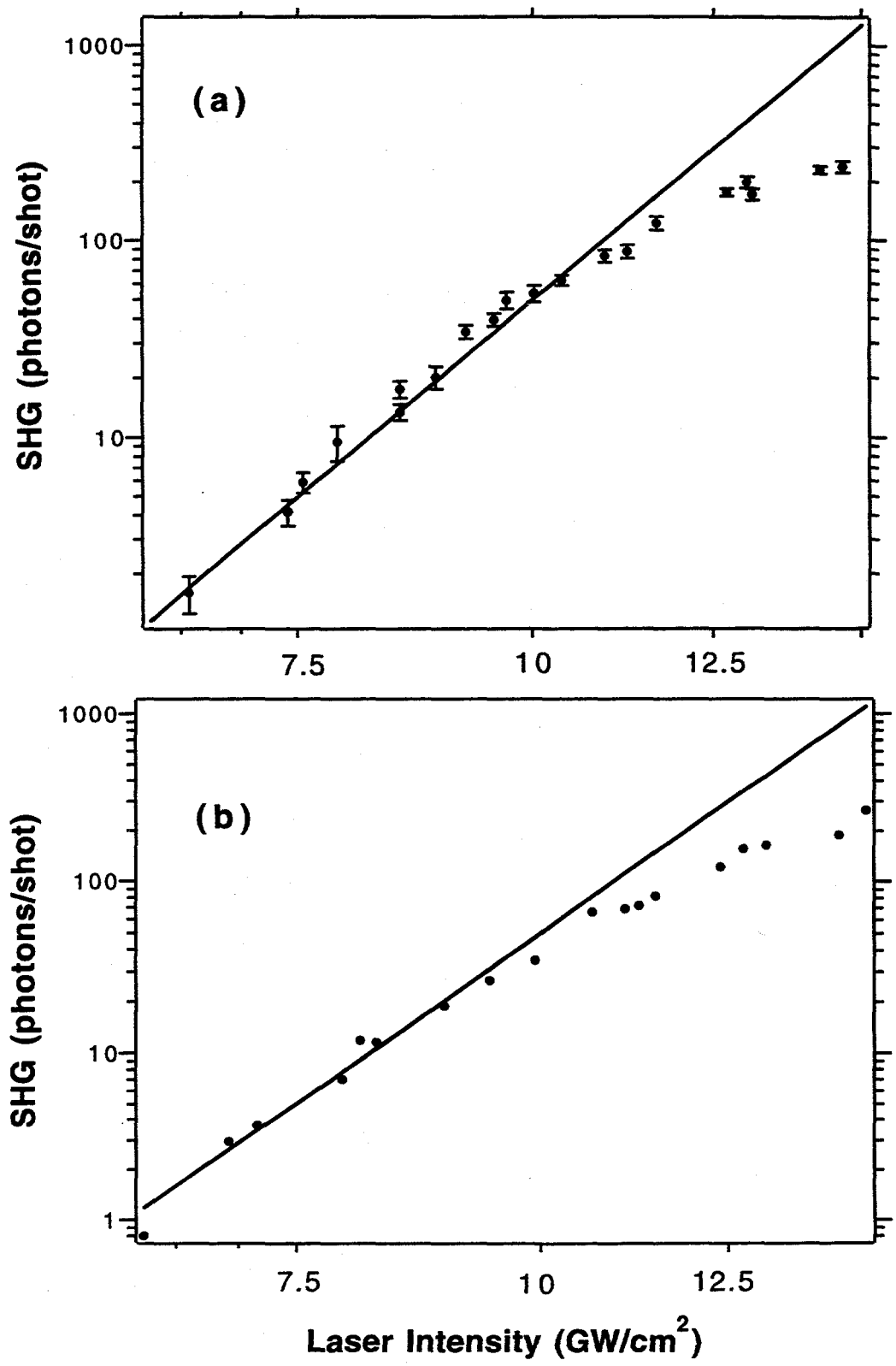
(a)
1000
100
10
SHG (photons/shot)
7.5
10
12.5
(b)
1000
100
10
1
SHG (photons/shot)
7.5
10
12.5
Laser Intensity (GW/cm^2)

Fig. 4

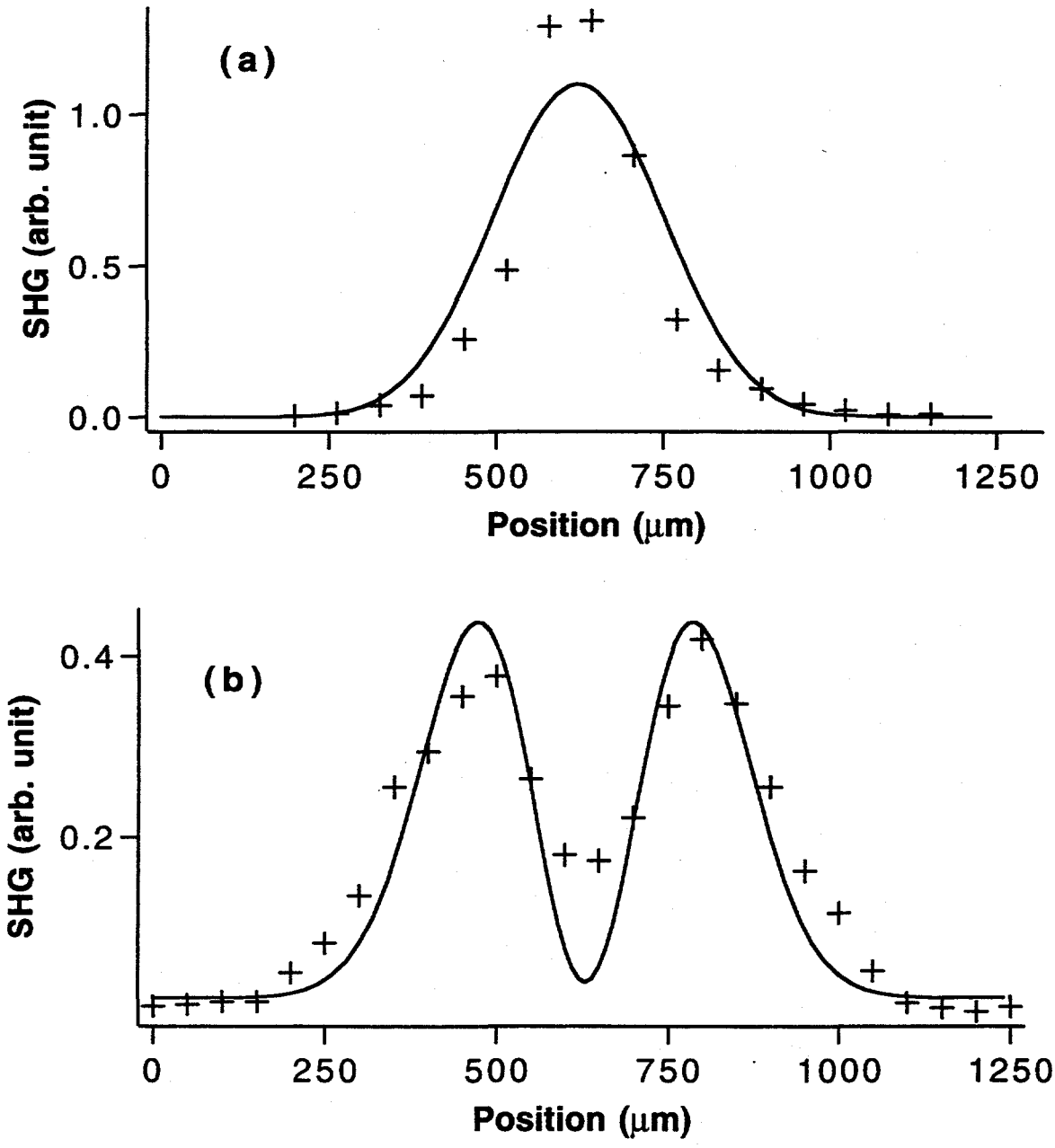
(a)
SHG (arb. unit)
1.0
0.5
0.0
0
250
500
750
1000
1250
Position (μm)
(b)
SHG (arb. unit)
0.4
0.2
0
250
500
750
1000
1250
Position (μm)

Fig. 5

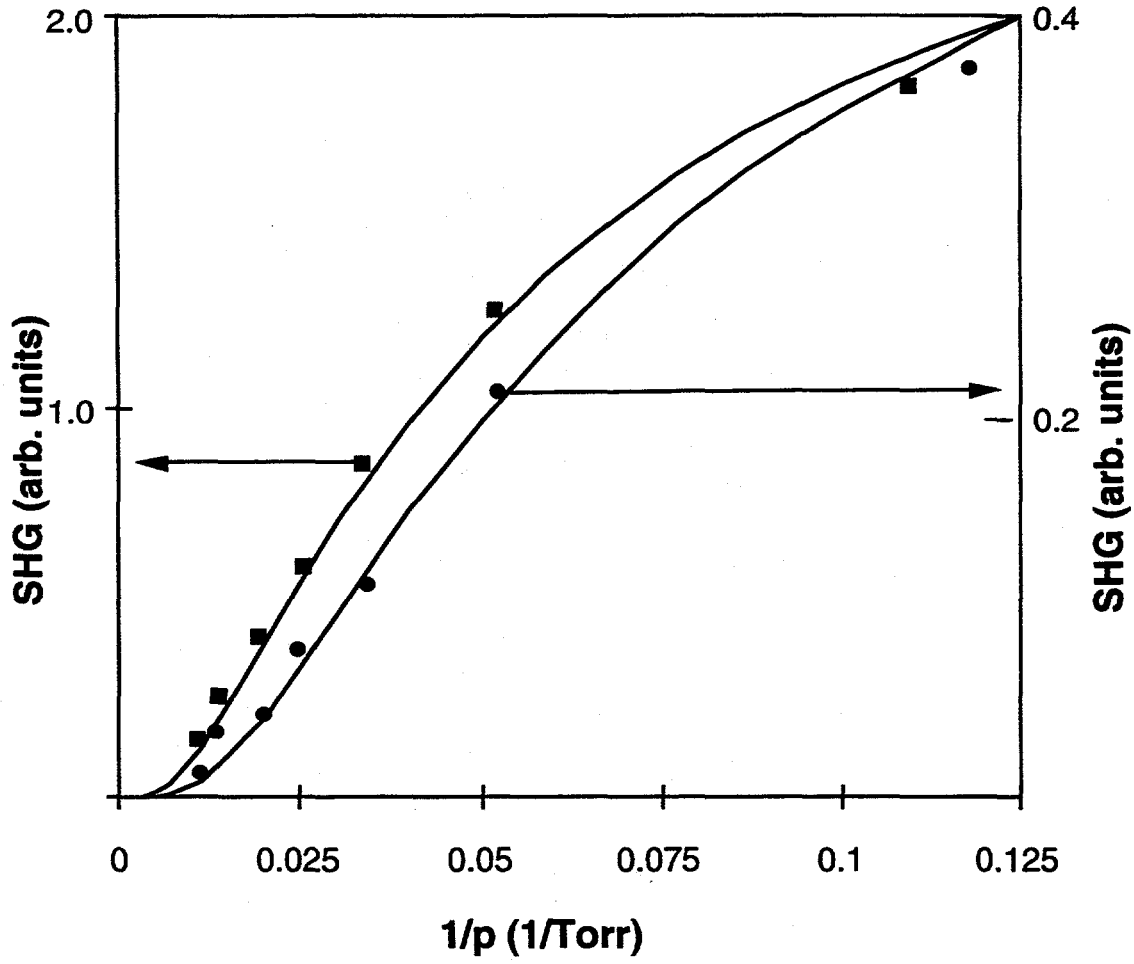
2.0
1.0
0.4
0.2
SHG (arb. units)
SHG (arb. units)
0
0.025
0.05
0.075
0.1
0.125
1/p (1/Torr)

Fig. 6

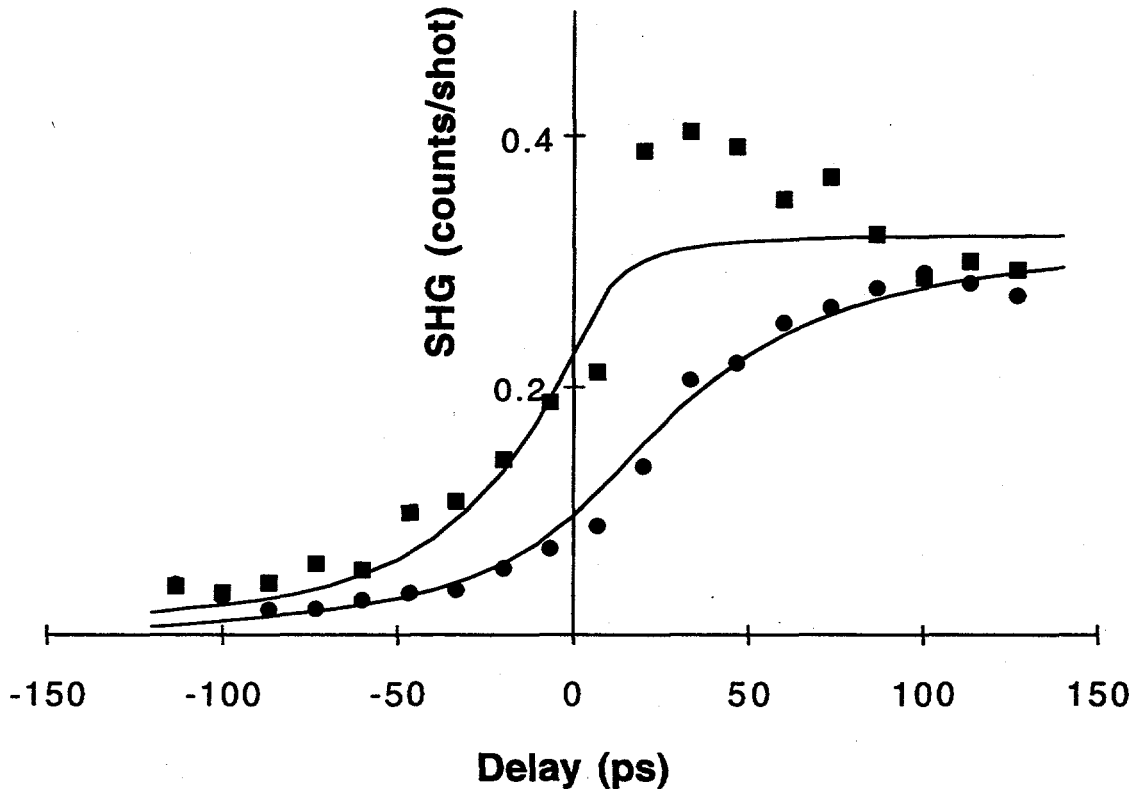

Fig. 7

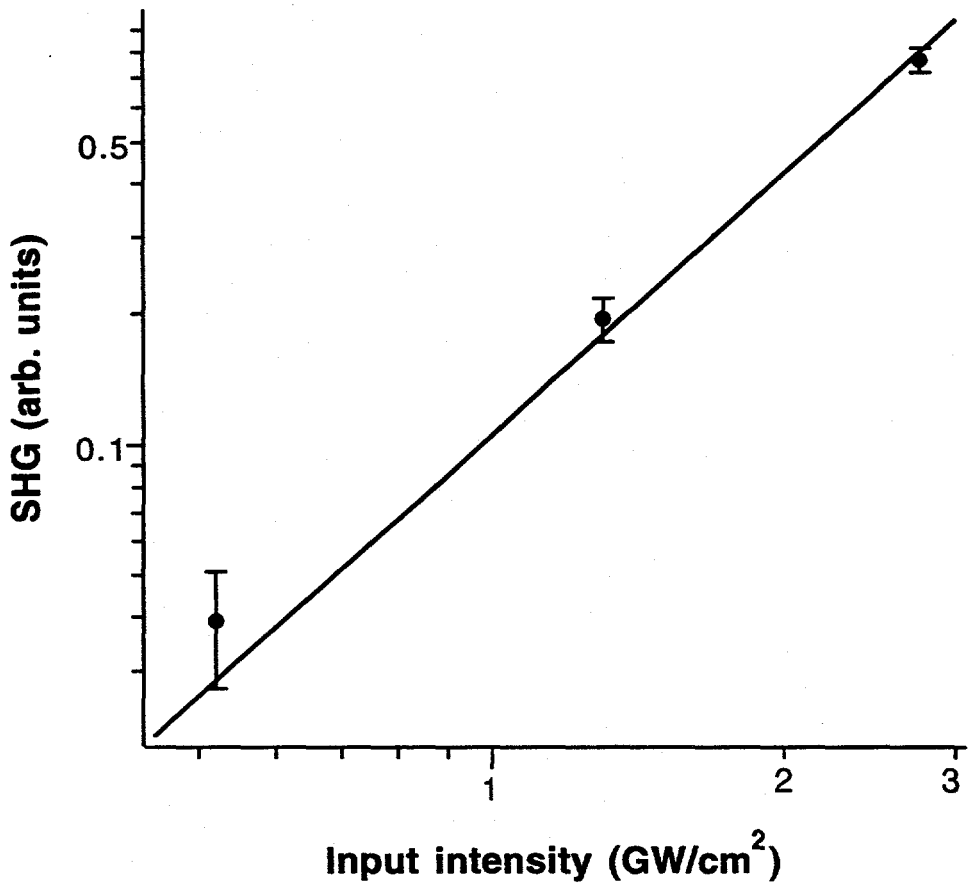

Fig. 8

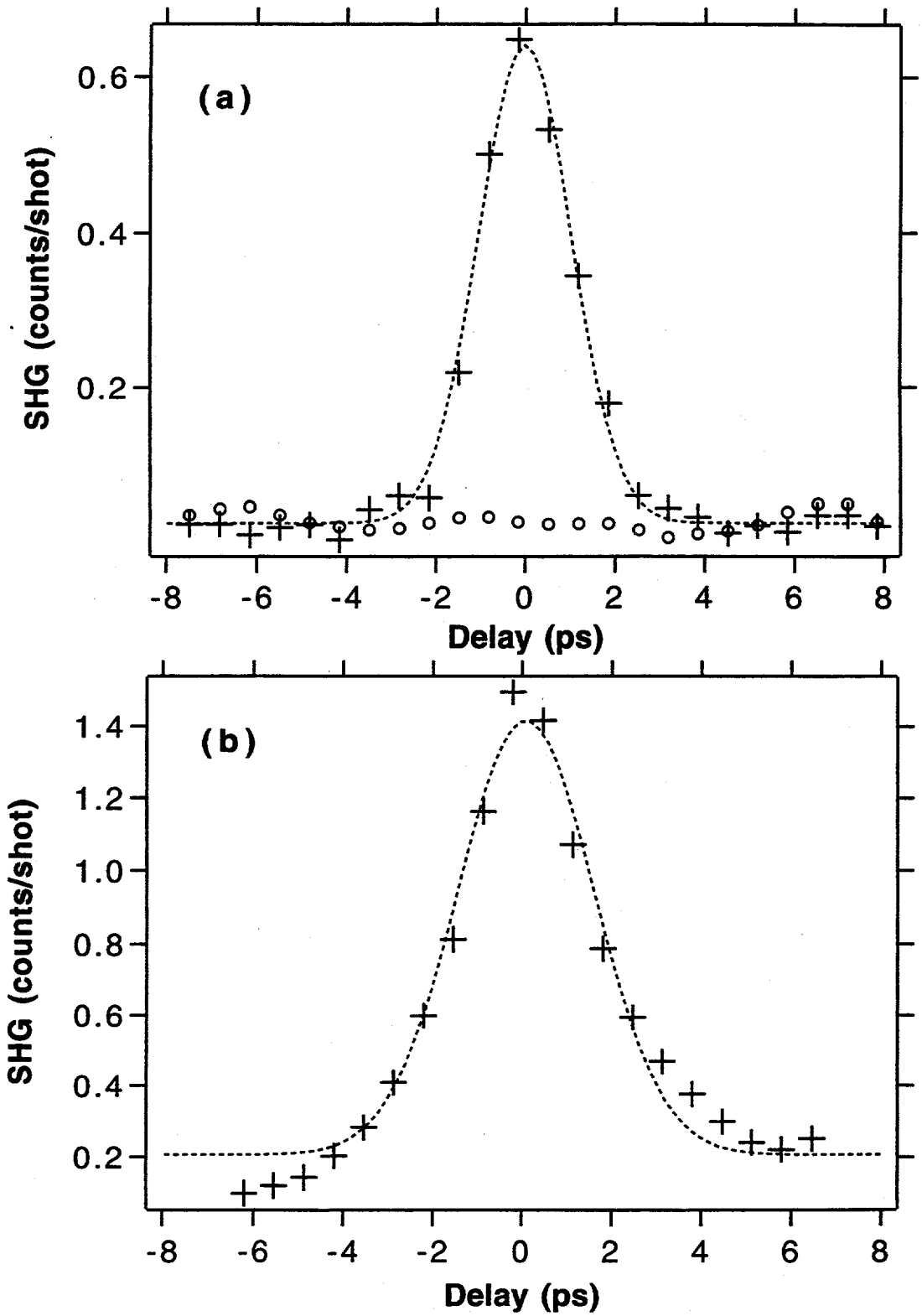
(a)
SHG (counts/shot)
0.6
0.4
0.2
-8
-6
-4
-2
0
2
4
6
8
Delay (ps)
(b)
SHG (counts/shot)
1.4
1.2
1.0
0.8
0.6
0.4
0.2
-8
-6
-4
-2
0
2
4
6
8
Delay (ps)

Fig. 9

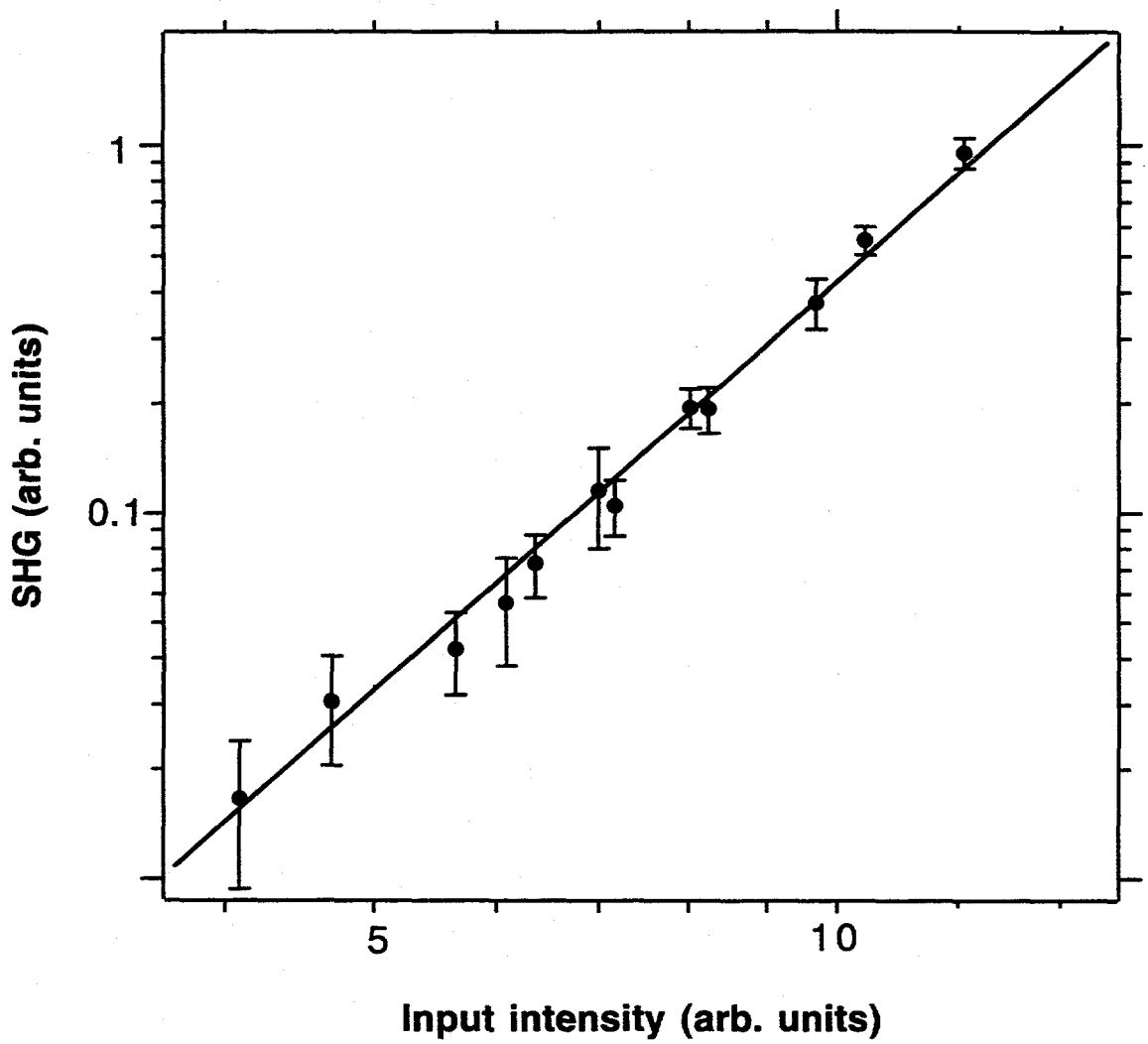

Fig. 10

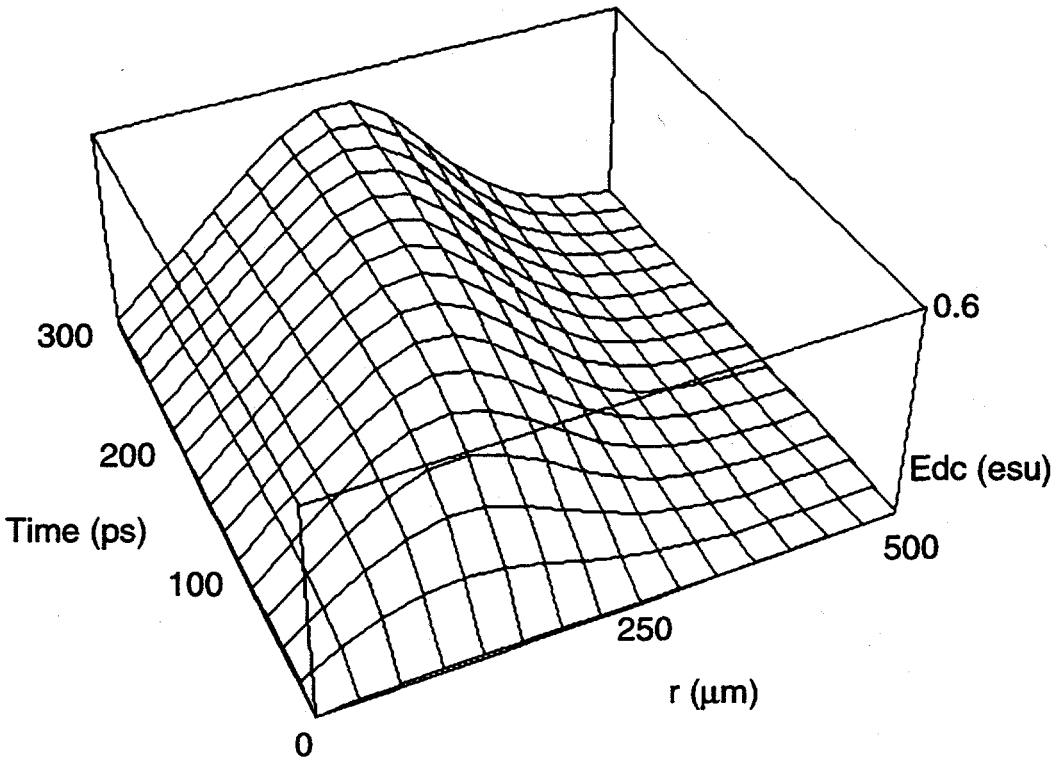

Fig. 11

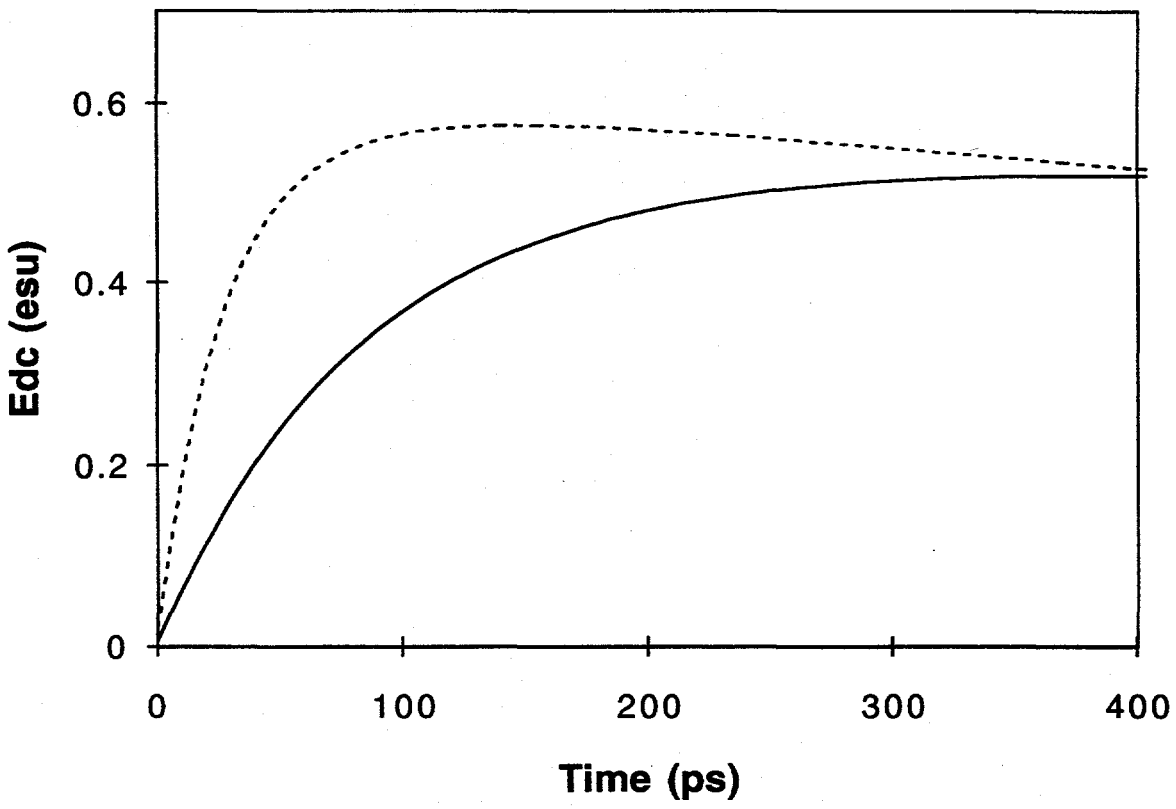

Fig. 12

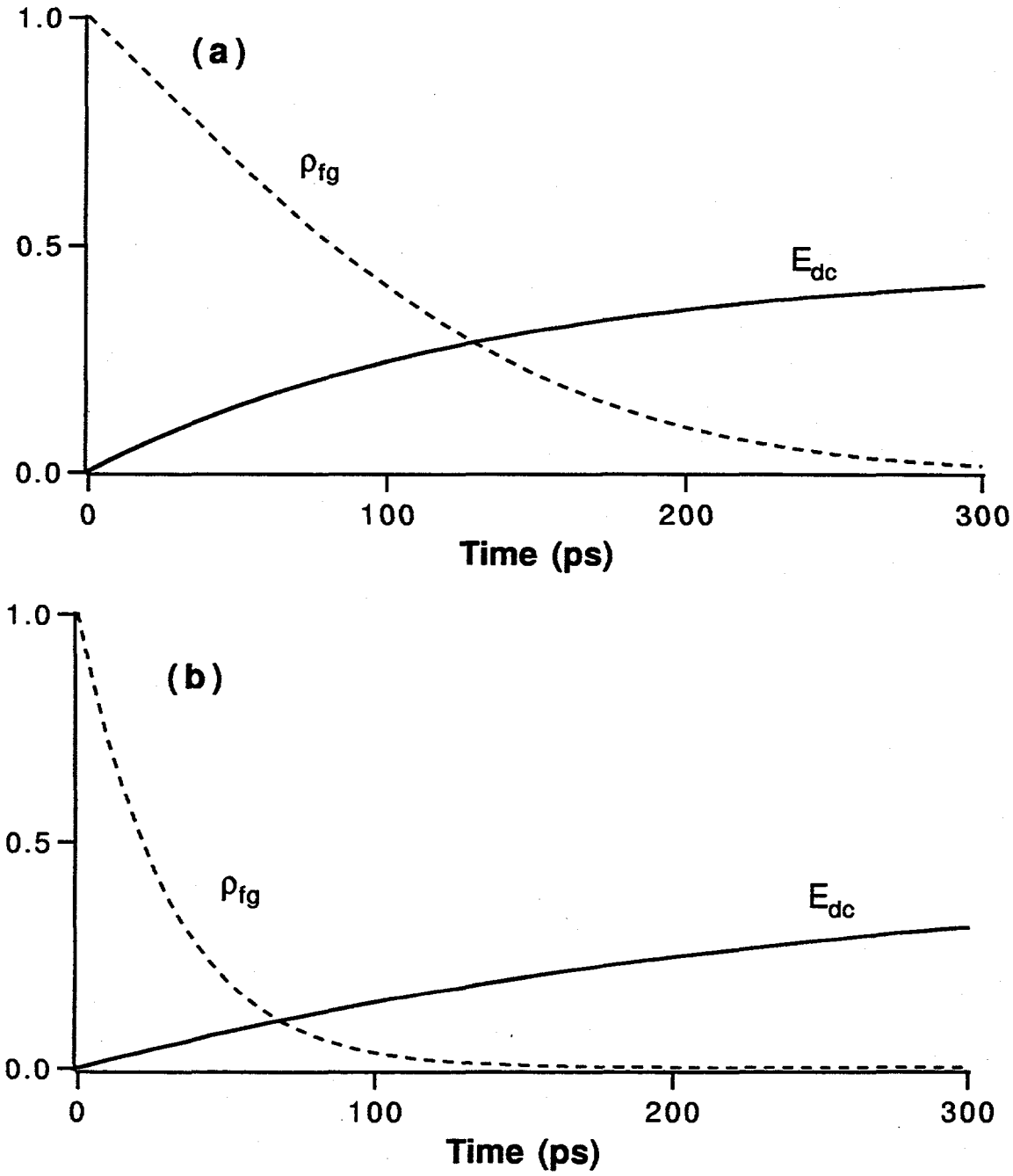
1.0
(a)
ρ_{fg}
0.5
E_{dc}
0.0
0
100
200
300
Time (ps)
1.0
(b)
0.5
ρ_{fg}
E_{dc}
0.0
0
100
200
300
Time (ps)

Fig. 13

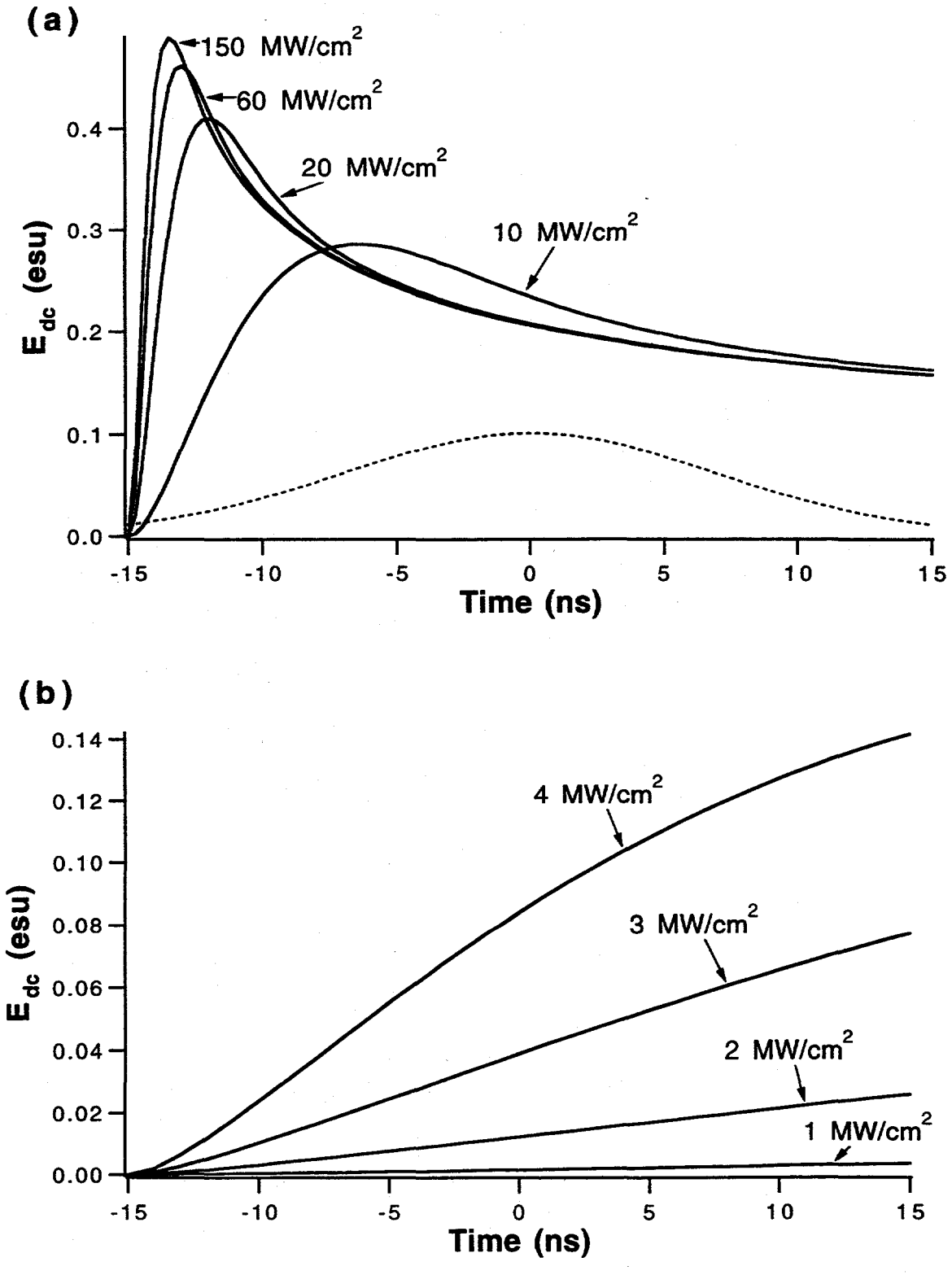
(a)
150 MW/cm2
60 MW/cm2
20 MW/cm2
10 MW/cm2
Edc (esu)
0.0
0.1
0.2
0.3
0.4
-15
-10
-5
0
5
10
15
Time (ns)
(b)
4 MW/cm2
3 MW/cm2
2 MW/cm2
1 MW/cm2
Edc (esu)
0.00
0.02
0.04
0.06
0.08
0.10
0.12
0.14
-15
-10
-5
0
5
10
15
Time (ns)

Fig. 14

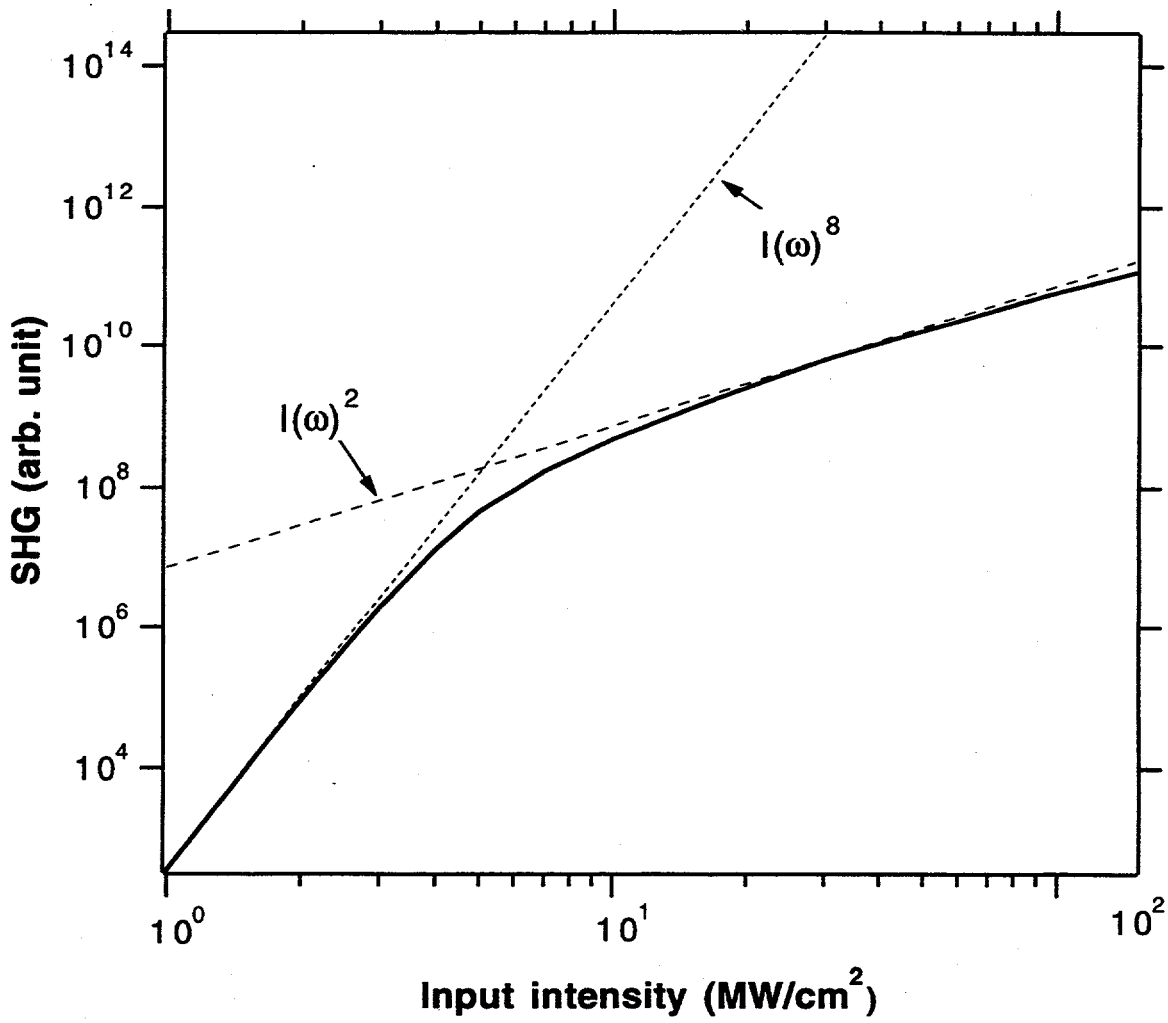
SHG (arb. unit)
10^14
10^12
10^10
10^8
10^6
10^4
I(ω)^8
I(ω)^2
10^0
10^1
10^2
Input intensity (MW/cm^2)

Fig. 15

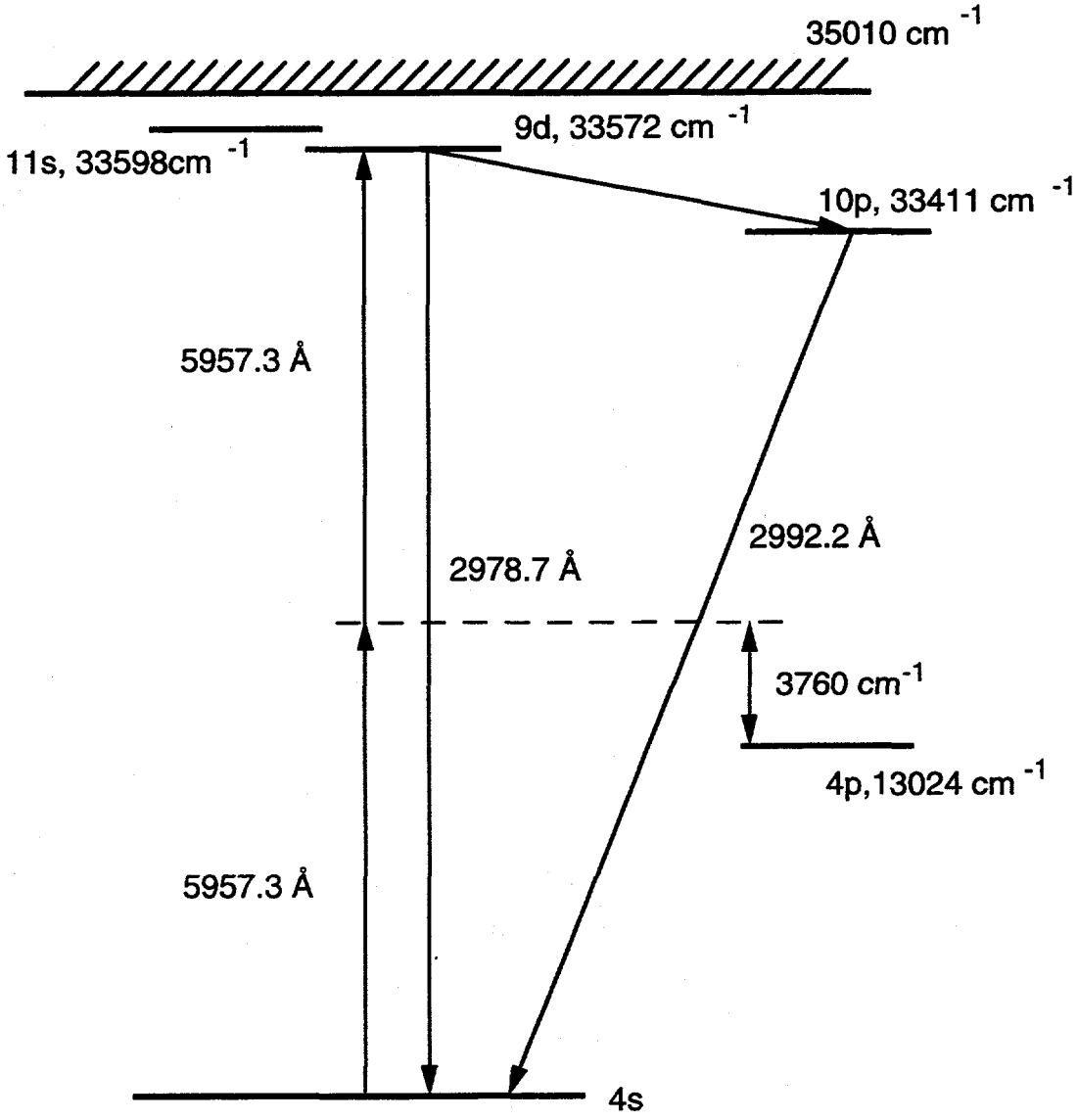
35010 cm -1
9d, 33572 cm -1
11s, 33598cm -1
10p, 33411 cm -1
5957.3 Å
2992.2 Å
2978.7 Å
3760 cm-1
4p,13024 cm -1
5957.3 Å
4s

Fig. 16

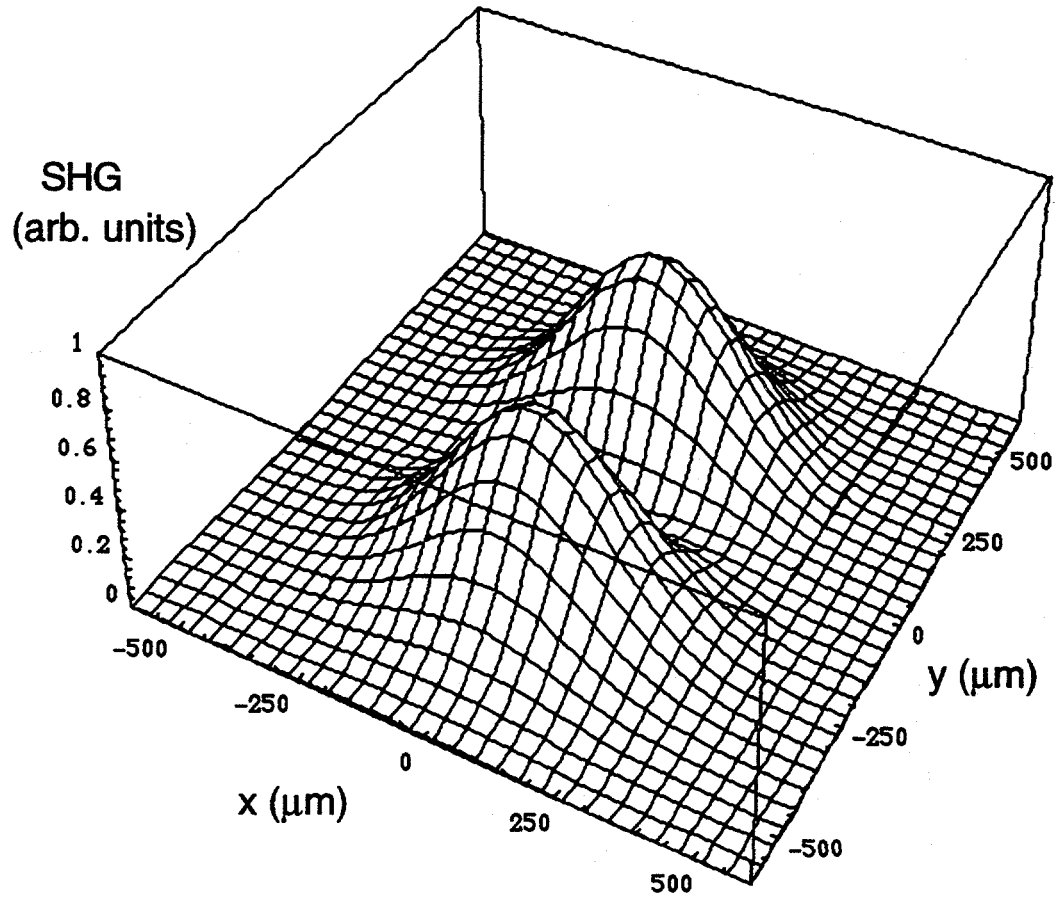
SHG
(arb. units)
1
0.8
0.6
0.4
0.2
0
-500
-250
0
250
500
x (μm)
500
250
0
-250
-500
y (μm)

Fig. 17

Chapter 3

Picosecond Optical Parametric Generator/Amplifier

Optical parametric oscillators and amplifiers have long been considered ideal coherent tunable sources [1]. In this chapter a homebuilt picosecond optical parametric generator/amplifier system (OPG/OPA) pumped by the third harmonic of a pulsed Nd:YAG laser is described in detail. We discuss in two separate sections construction and output characteristics of the system. The system has been used in surface vibrational spectroscopic studies via sum–frequency generation (SFG). Several SFG spectra obtained with this system are presented as examples.

3.1 Construction

The pump laser is a commercial active–passive mode–locked Nd:YAG laser (PY61C–20) manufactured by Continuum Inc. The oscillator stage of the laser produces 25 ps, ~3 mJ pulses at 1.06 μm with 20 Hz repetition rate. The recommended single–pulse output energy from the oscillator is 3–5 mJ/pulse with #5 dye for passive mode–locking but the dye cell mirror could be easily damaged at this output power level. By lowering the dye concentration to yield a 2.2 mJ/pulse output, the overall stability of the output was not as good as in the 3/mJ/pulse output case but with good alignment of the cavity we were still able to get less than 2 % average output fluctuation. Also with good alignment the burn pattern of the output is nearly TEM_{00}. Even at this dye concentration, the dye cell was damaged usually after one month of heavy use. The damage could be easily seen without removing the dye cell mirror but since nonlinear optical conversion is very sensitive to small deteriorations of the laser mode quality, the reduced OPG/OPA conversion efficiency and stability was our most sensitive indication of the presence of damage. To ease the process of realignment of the cavity upon damage of the dye cell, the mount for dye–cell end mirror was modified such that we could translate the whole end–mirror and realign the cavity without moving other elements in the cavity. The damage on the mirror was not permanent but in the form of some laser–decomposed dye residue sticking on the window. The residue could be wiped out and the cell could be reused.

The single–pulse output from the oscillator was focused and sent through a pinhole

for spatial filtering to improve the mode quality. Then it is amplified by the single–pass Nd:YAG amplifer to generate ~30 mJ/pulse of amplified output. The whole laser system can operate at 10 Hz or 20 Hz repetition rate. At 20 Hz, we observed slight degradation of the amplified output mode. At a distance of ~7 m from the amplifier rod, the mode became more elliptical (the horizontal beam size was about 20 % larger than the vertical one) and the polarization of the amplifier output contained about 10 % of unwanted horizontal polarization mainly along the two diagonal directions of the beam. This degradation at 20 Hz cannot be corrected and is believed to come from thermal birefringence of the Nd:YAG amplifier rod since even at 20 Hz we saw less degradation at lower output powers.

We used 75 % of the 30 mJ/pulse output to generate third–harmonic of the 1064 nm output. First, it was used to generate second–harmonic in a a non–critically phase–matched (type–I) LBO (lithium triborate) crystal ($7\times7\times6$ mm^3). The phase–matching temperature of the crystal at 1064 nm was 148 °C [2] from the literature, but we obtained best conversion at 153 °C (temperature of the oven surrounding the crystal). The second–harmonic output then combined with the transmitted fundamental beam in a type–II angle–tuned LBO crystal ($\theta = 90°$, $\theta = 42.2°$, $7\times7\times6$ mm^3) at room temperature to generate the third harmonic. LBO crystals are known to be hygroscopic. If they are used at room temperature in an ambient atmosphere, they can become foggy after several months of use even if the crystal surfaces are AR coated. To prevent fogging, we raised the temperature of the whole crystal to 50 °C and changed the phase matching angle by 1.3°

following the known temperature dependence of the dielectric constant of the LBO crystal [3] to get the optimal phase–matching. The third–harmonic crystal was cut for type–II phase–matching. For optimal third–harmonic generation, the photon numbers of the fundamental and second–harmonic input beams should be nearly equal and the spatial modes of the two beams should be well matched. To avoid mode distortion of the fundamental due to energy depletion by SHG in the SHG crystal, we used a $\lambda/2$ plate in front of the SHG crystal to put the part of the input beam in the wrong polarization for SHG so that it would not be depleted and used another $\lambda/2$ plate after the SHG crystal to bring it back to the right polarization for THG. By this means, we could obtain a 15 ps, 7mJ/pulse, horizontally polarized TH output at 355 nm which was then used to pump two identical OPG/OPA systems. A BBO crystal ($\theta = 31.3°$, $7\times7\times4$ mm^3) cut for type–I phase–matching was briefly tried as a replacement for the LBO THG crystal. From the known nonlinearities of LBO and BBO [4], it was expected that the BBO crystal should yield a better third–harmonic conversion in spite of the shorter length, but the observed result was opposite to the prediction.

Figure 3.1 is the schematic of the OPG/OPA setup pumped by the above third–harmonic output. This OPG/OPA system is based on the design by Zhang *et al.* [5]. The 7 mJ/pulse THG output was split into two by a 355 nm beamsplitter, and each beam pumped an OPG/OPA system. For OPG/OPA systems, BBO is often the crystal of choice due to its large nonlinearity and high damage threshold [5, 6]. In each of our OPG/OPA systems, the two BBO crystals ($\theta = 28.5°$, $8\times6\times8$

mm^3) were positioned 25 cm apart with optic axis of both crystals parallel to the table but rotated azimuthally in opposite directions to compensate walk–off in each crystal. The size of the 355 nm pump beam was 1.4 mm × 1.2 mm (horizontal and vertical $1/e$ radius, respectively), which gave 4 GW/cm^2 of pump intensity.

The signal and idler beams generated by the optical parametric process in the first path were sent to a grating. The reflected beam had a reduced linewidth and acted as a seed beam in the second path passing through the crystals. The grating used in one arm was a holographic grating with 1800 grooves/mm. The reflection efficiency was greater than 30 % for both polarizations throughout the tuning range of 350 – 800 nm. The grating used in the other arm was a holographic grating with 3600 grooves/mm with similar reflection efficiency. A pair of lenses was used as a telescope (magnification = 11) between the second BBO crystal and the grating to increase the effective dispersion of the grating. The spectral bandwidth of the reflected seed beam from the grating is given by:

$$\Delta\lambda = \Delta\beta \frac{d\cos\beta}{mM}, \tag{3.1}$$

where β is the average diffraction angle of the dispersed seed beam, $\Delta\beta$ is the angular spread of the seed beam that would be amplified in the second path through the BBO crystals, d is the groove spacing (e. g. $d = 1/1800$ mm for a 1800 grooves/mm grating), m is the order of diffraction, and M is the magnification of the telescope. For $\lambda = 5500$ Å, the diffraction angle is $\beta = 30°$. Since the pump beam size is ~2.5 mm and the distance from the crystal to the first telescope lens is 50 cm, we have $\Delta\beta = 0.3/50 = 5$ mrad. By putting $m = 1$ and $M = 11$

we get $\Delta\lambda = 2.2$ Å, in reasonable agreement with the measured linewidth of the OPG/OPA, as will be described in the next section (Fig 3.4).

The OPG/OPA output is tunable from 0.41 μm to 2.6 μm (signal and idler output combined). To get tunable IR output in the mid–IR range, we used difference frequency generation (DFG) from either a $AgGaS_2$ or a $LiNbO_3$ crystal. Difference frequency generation is the nonlinear optical process that generates output at the difference frequency of the two input beams. We used the 1.06 μm beam from the Nd:YAG laser and the tunable idler output from the OPG/OPA as the two input beams for DFG. A color filter (RG 715 or RG 850) was used to block the signal beam from the OPG/OPA. The energy of the idler beam at the DFG crystal position was measured to be ~20 μJ/pulse. The beam size of the 1.06 μm input (2.5 mJ/pulse) was 2.8 mm $\times$ 2.1 mm (horizontal and vertical $1/e$ radius, respectively), which gave 0.5 GW/cm^2 of pump intensity, well below the known surface damage threshold of the $AgGaS_2$ crystal at 1.06 μm [7]. The $AgGaS_2$ crystal ($\theta = 41.5°$, $8\times10\times15$ mm^3) was cut for type–I phase–matching to generate tunable IR output from 2.3 μm to 9 μm, optimized (normal incidence) for DFG output at 6 μm . Although good care was taken to use the crystal under the damage threshold, one of the $AgGaS_2$ crystals was damaged after several months of use. Since the damage was from the exit surface of the crystal (where the 1.06 μm intensity was lower due to depletion of the pump beam) into the bulk with a shape of a cone, it was believed to come from the self–focusing of the 1.06 μm pump beam.

In the IR wavelength range shorter than 4 μm, a $LiNbO_3$ crystal (5 cm long, $\theta = 47°$) was used with identical input beam parameters as those for the $AgGaS_2$ crystal and yielded the same output energy. Since the damage threshold of $LiNbO_3$ at 1.06 μm is much higher than that for $AgGaS_2$ crystal [8], the input beam intensity can be increased further to yield more DFG.

The DFG output from either the $AgGaS_2$ or the $LiNbO_3$ crystal is collinear with the remaining 1.06 μm beam and amplified seed (idler) beam, and we used a Ge plate to block them. The DFG output was vertically polarized as expected from type–I phase matching. The Ge plate at the brewster angle position allowed transmission of the DFG output without appreciable loss of the energy.

The final tunable IR output was reflected via a set of two gold mirrors to change its polarization in either vertical or horizontal directions and focused onto the sample with a BaF_2 lens (f=10 cm). A 532 nm beam from a separate BBO SHG crystal was also loosely focused (f=1 m) on the sample to overlap with the tunable IR spatially and temporally to generate surface SFG. The layout of the laser and SFG system is shown in Fig. 3.2 along with the beam paths and polarizations of the beams.

3.2 Output Characteristics and Sample Spectra

The output energies from the OPG/OPA system and from DFG vary with the wavelength as shown in Figure 3.3. The low power of the signal output at short

and long wavelength ends can be due to increased absorption of the idler photon inside the BBO crystal. Even though the quoted transparency range of the BBO crystal is 0.19 μm – 3 μm [5], the transparency of the crystal starting from 2.3 μm begins to drop [9]. As for DFG output, we have fairly constant output energy down to 2500 cm^{-1}. Afterwards it drops gradually and at 9 μm the energy is only about 10 μJ/pulse. FTIR measurement of our crystals showed significant absorption starting at 8.5 μm.

The pulsewidth of the DFG tunable IR output was measured using cross–correlation of the IR pulse and the second–harmonic pulse from the laser by sum–frequency generation in a z–cut crystalline quartz. Figure 3.4 depicts the result. The second–harmonic pulse has a 18 ps pulsewidth. Since the cross–correlation trace shows a FWHM of 23 ps, we can deduce for the DFG output a pulsewidth of about 14 ps.

Figure 3.5 is the linewidth of the visible output (with an 1800 grooves/mm grating) at several different wavelengths in the tuning range. As mentioned in the previous section, the linewidth is close to the calculated value (Eq. (3.1)). It is even smaller at short wavelengths but becomes larger at longer wavelengths and reaches the maximum value at the degenerate point of OPG/OPA. The FWHM linewidth at the degenerate point is ~3.1 Å , significantly larger than that at 4200 Å.

We have used the OPG/OPA system for surface sum–frequency generation spectroscopic work. The wide IR tuning range allows us to study surface vibrational

resonances of different materials. Figures 3.6–3.9 show some sample SFG spectra for various surfaces and interfaces (air/solid, air/monolayer/solid, Langmuir monolayer, air/liquid) obtained with the above OPG/OPA system.

Bibliography

[1] J. A. Giordmaine and R. C. Miller, Phys. Rev. Lett. **14**, 973 (1965); R. A. Baumgartner and R. L. Byer, IEEE. J. Quantum Electron. **QE–15**, 432 (1979).

[2] T. Ukachi, R. J. Lane, W. R. Bosenberg, and C. L. Tang, Appl. Phys. Lett. **57**, 980 (1990).

[3] D. N. Nikogosyan, Appl. Phys. A **58**, 181 (1994).

[4] V. G. Dmitriev, G. G. Gurzadyan, and D. N. Nikogosyan, *Handbook of Nonlinear Optical Crystals* (Springer–Verlag, Berlin, 1991).

[5] J. Y. Zhang, J. Y. Huang, Y. R. Shen, and C. Chen, J. Opt. Soc. Am. B **10**, 1758 (1993).

[6] J. Y. Huang *et al.*, Appl. Phys. Lett. **57**, 1961 (1990); J. Y. Zhang *et al.*, Appl. Phys. Lett. **58**, 213 (1991).

[7] H. J. Krause and W. Daum, Appl. Phys. Lett. **60**, 2180 (1992); Appl. Phys. B **56**, 8 (1993).

[8] J. H. Hunt, Ph. D. Thesis, Unversity of California, 1988, unpublished.

[9] D. Eimerl, *et al.*, J. Appl. Phys. **62**, 1968 (1987).

Figure Captions

Figure 3.1: Layout of the OPG/OPA system (IR arm). The visible arm is identical to this except an 1800 grooves/mm holographic grating is used for seeding.

Figure 3.2: Layout of the laser system. M1: 1.06 μm mirror, M2: 532 nm mirror, M3: 355 nm mirror, M_{ir}: gold mirror for the tunable IR output. BS: beamsplitter. The two mirrors M2 and M_{ir} at the top left of the figure can be changed to get either s or p polarization into the sample. The $\updownarrow$ (or $\leftrightarrow$) on the beam path denotes horizontal polarization and $\circ$ means vertical polarization of the beam.

Figure 3.3: Output energy spectrum of the OPG/OPA (signal+idler) and DFG (from an $AgGaS_2$ crystal) throughout the tuning range.

Figure 3.4: Cross correlation SFG signal from crystalline (z–cut) quartz with 532 nm beam and tunable IR output at 3 μm. Full–width at half–maximum of the cross–correlation trace is 25 ps and the pulsewidth of tunable output is 15 ps from the known pulsewidth (18ps) of the 532 nm beam.

Figure 3.5: Linewidths of the OPG/OPA output (visible arm) at several different output wavelengths. (a) At 4207 Å, full–width at half–maximum (FWHM) 1.0 Å; (b) at 5441 Å, FWHM 2.9 Å; (c) at 7078 Å, FWHM 3.1 Å.

Figure 3.6: SFG spectrum for the solid(Si)/air interface with ppp polarization. After chemical oxidation of Si(111) in H_2O:H_2O_2:HCl=4:1:1 solution for 10 minutes and wet etching of surface in buffered NH_4F ((49 %) for 3 minutes, a SiH vibrational resonance at 2080 cm^{-1} is seen with ppp polarization. Solid line is a fit to the spectrum with 12 cm^{-1} peakwidth.

Figure 3.7: SFG spectra of monolayer OTS (octadecyltrichlorosilane) on glass surface with ssp, ppp, and sps polarizations. Peak at 2878 cm^{-1}: CH_3 symmetric stretch, 2920 cm^{-1}: CH_2 asymmetric stretch, 2950 cm^{-1}: Fermi resonance of CH_3 symmetric stretch with the overtone of CH_3 bending vibration, 2965 cm^{-1}: CH_3 asymmetric stretch.

Figure 3.8: SFG spectra of Langmuir monolayer of 8CB (4'n–octyl–4–cyanobiphenyl) on water. Peak assignments are the same as in Fig. 3.7.

Figure 3.9: SFG spectrum of neat liquid (water)/air interface with ssp polarization. Two broad peaks around 3250 and 3400 cm^{-1} are due to OH vibration of water molecules hydrogen bonded to the neighboring water molecules (bound OH), and the narrower peak at 3700 cm^{-1} is due to the surface OH vibration free of any hydrogen bond to neighboring water molecules (free OH).

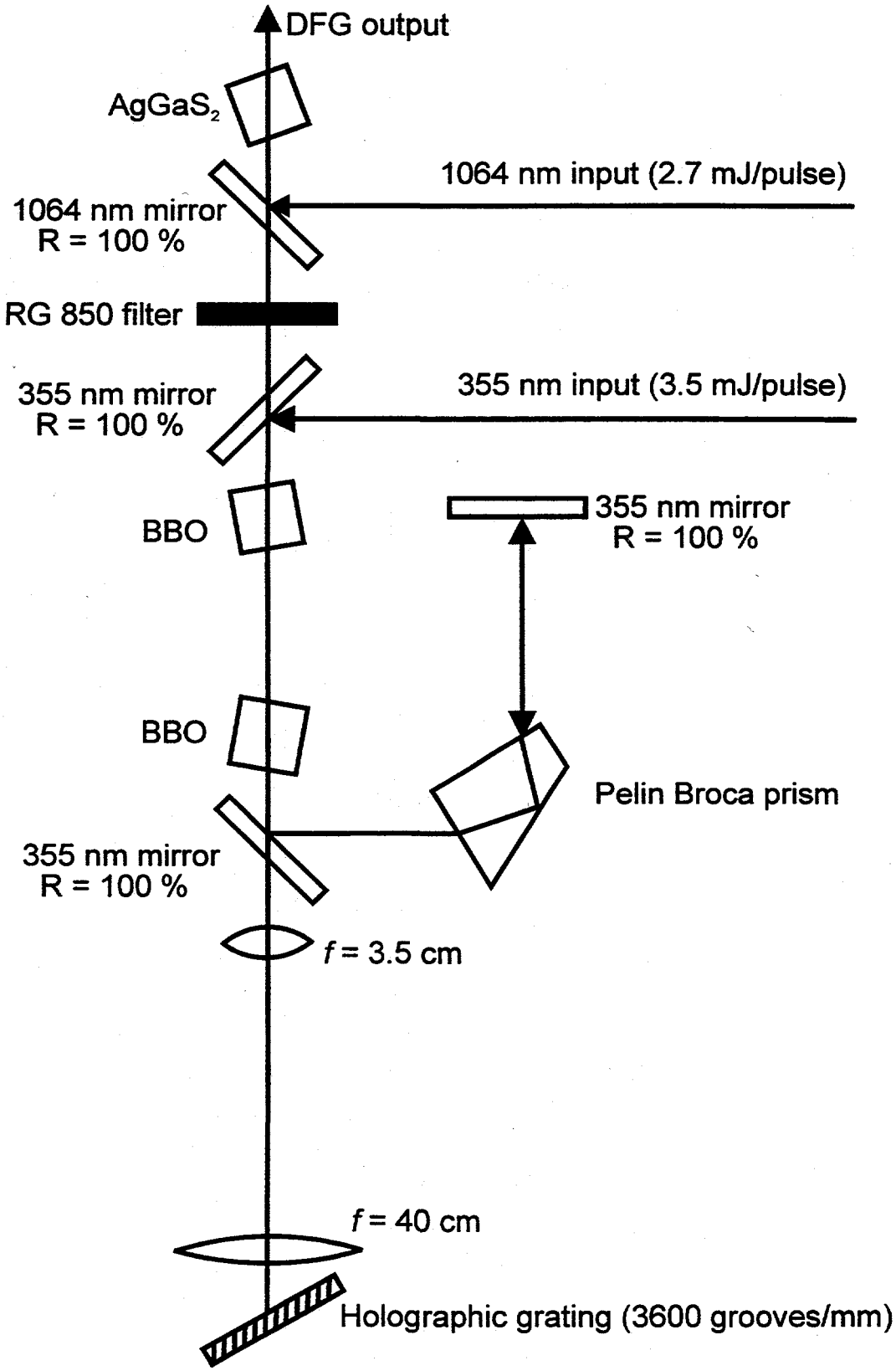
DFG output
$AgGaS_2$
1064 nm input (2.7 mJ/pulse)
1064 nm mirror
R = 100 %
RG 850 filter
355 nm mirror
R = 100 %
355 nm input (3.5 mJ/pulse)
BBO
355 nm mirror
R = 100 %
BBO
Pelin Broca prism
355 nm mirror
R = 100 %
f = 3.5 cm
f = 40 cm
Holographic grating (3600 grooves/mm)

Fig. 1

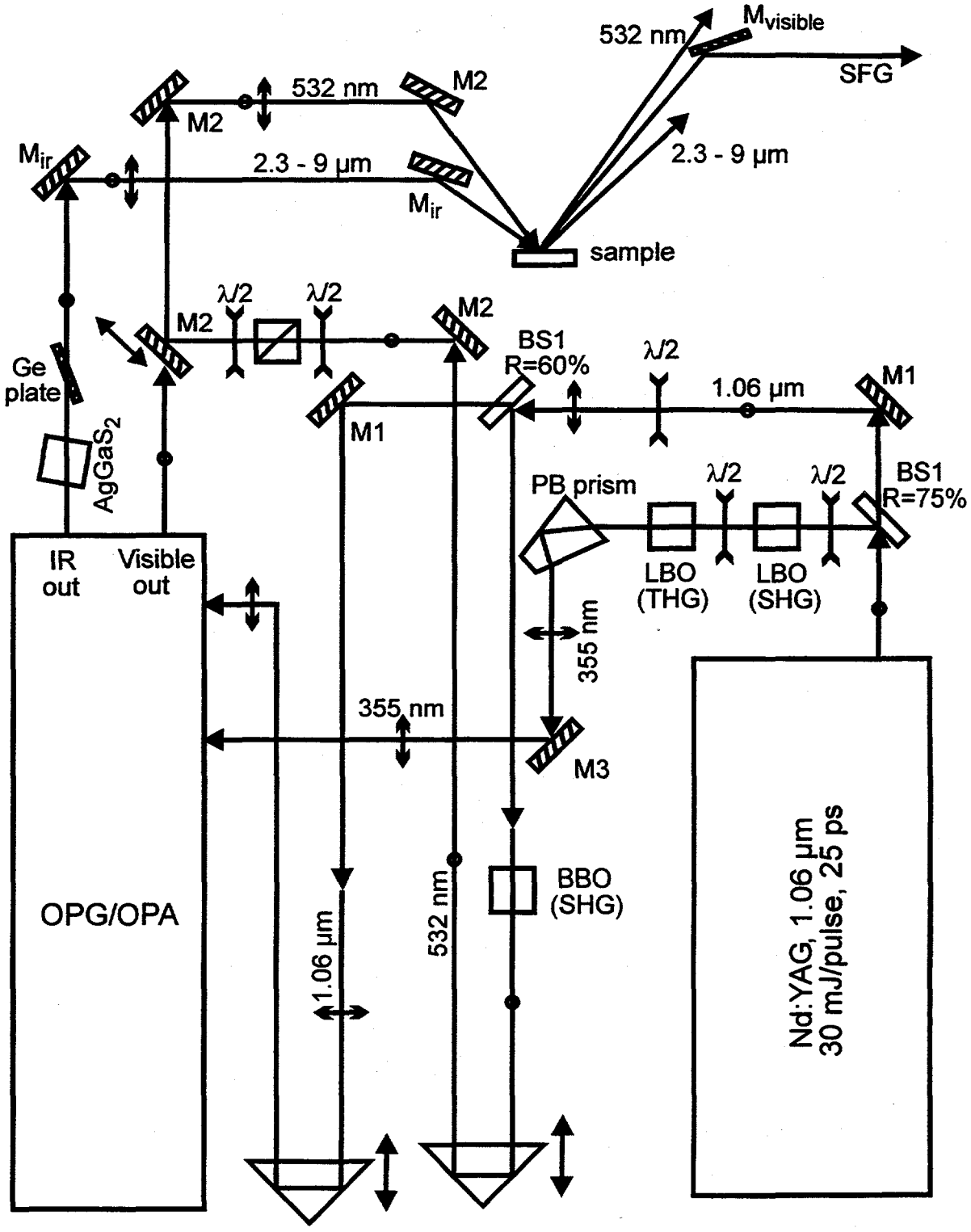
532 nm
M visible
SFG
532 nm
M2
M2
M ir
2.3 - 9 μm
2.3 - 9 μm
M ir
sample
λ/2
λ/2
M2
M2
BS1
R=60%
λ/2
1.06 μm
M1
Ge
plate
M1
AgGaS2
PB prism
λ/2
λ/2
BS1
R=75%
IR
out
Visible
out
LBO
(THG)
LBO
(SHG)
355 nm
355 nm
M3
OPG/OPA
1.06 μm
532 nm
BBO
(SHG)
Nd:YAG, 1.06 μm
30 mJ/pulse, 25 ps

Fig. 2

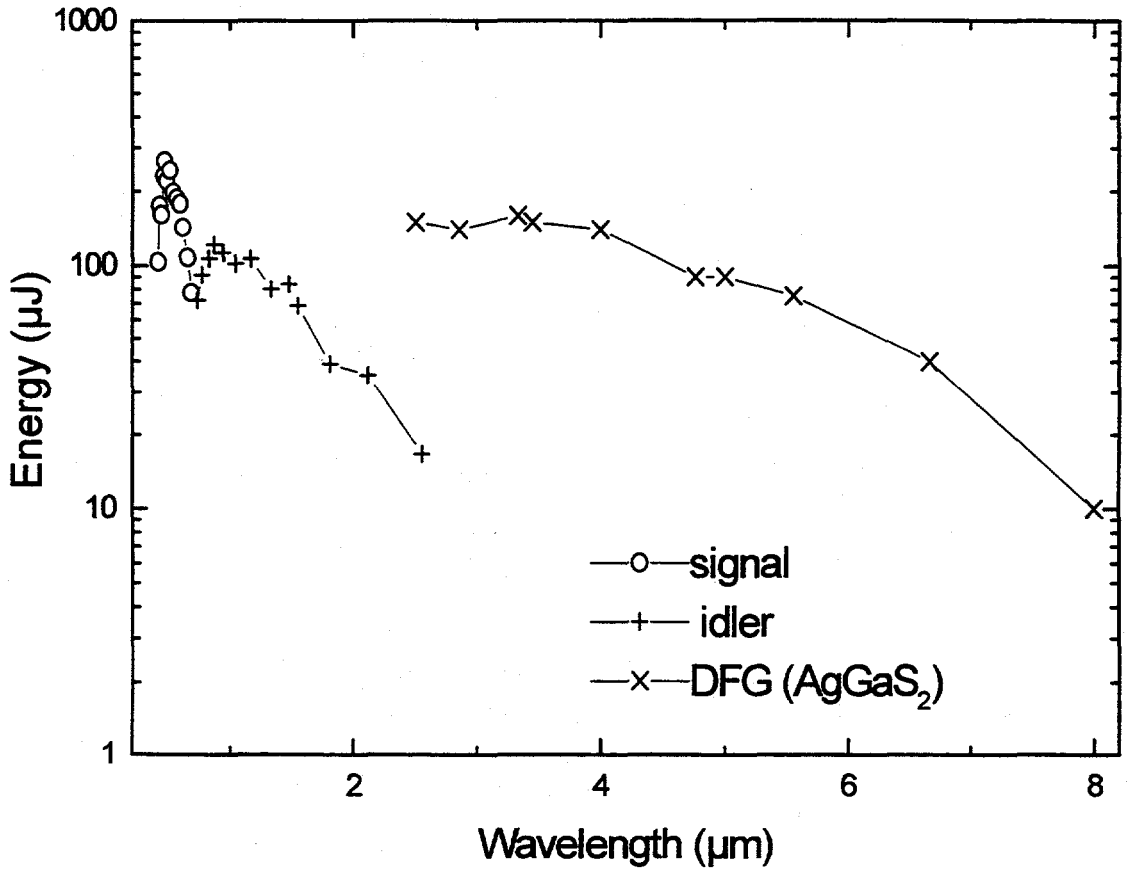
1000
100
10
1
Energy (μJ)
2
4
6
8
Wavelength (μm)
signal
idler
DFG (AgGaS2)

Fig. 3

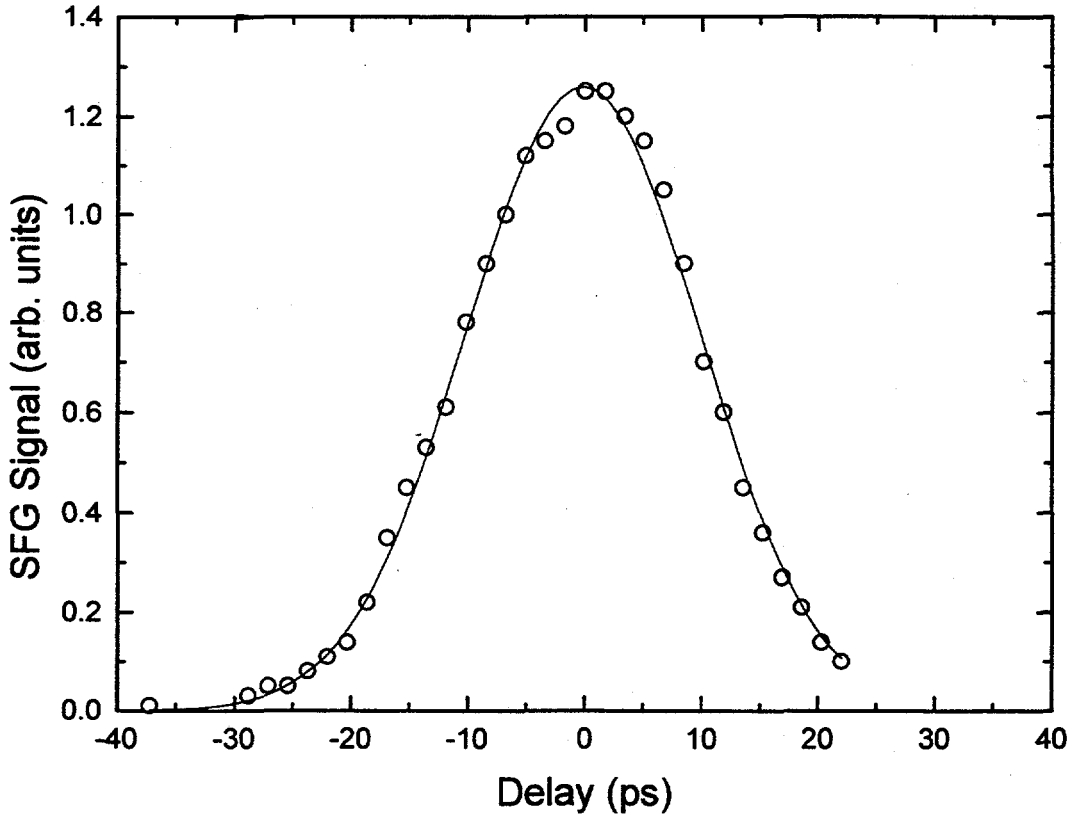
SFG Signal (arb. units)
Delay (ps)
1.4
1.2
1.0
0.8
0.6
0.4
0.2
0.0
-40
-30
-20
-10
0
10
20
30
40

Fig. 4

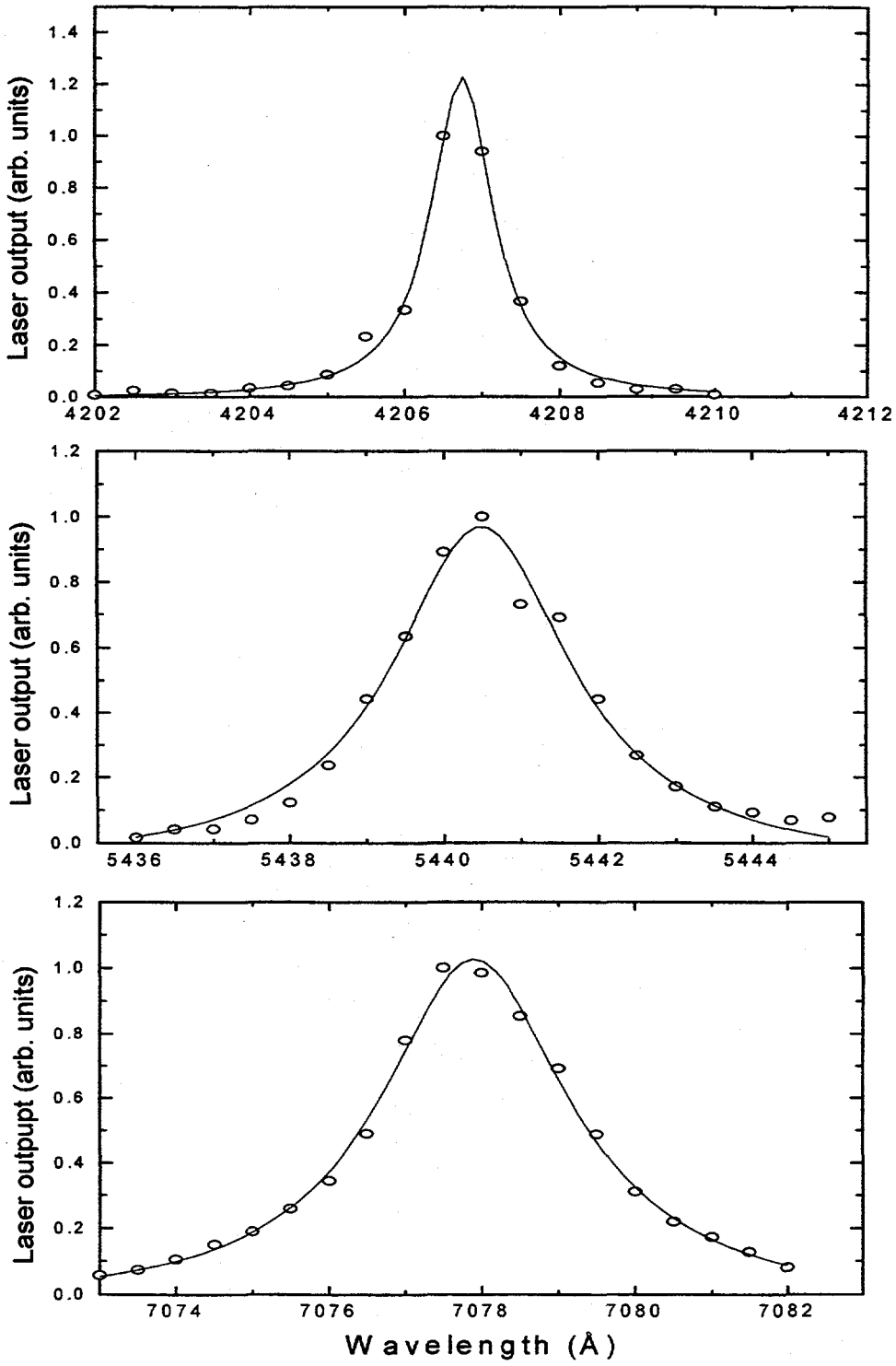
Laser output (arb. units)
1.4
1.2
1.0
0.8
0.6
0.4
0.2
0.0
4202
4204
4206
4208
4210
4212
Laser output (arb. units)
1.2
1.0
0.8
0.6
0.4
0.2
0.0
5436
5438
5440
5442
5444
Laser outpupt (arb. units)
1.2
1.0
0.8
0.6
0.4
0.2
0.0
7074
7076
7078
7080
7082
Wavelength (Å)

Fig. 5

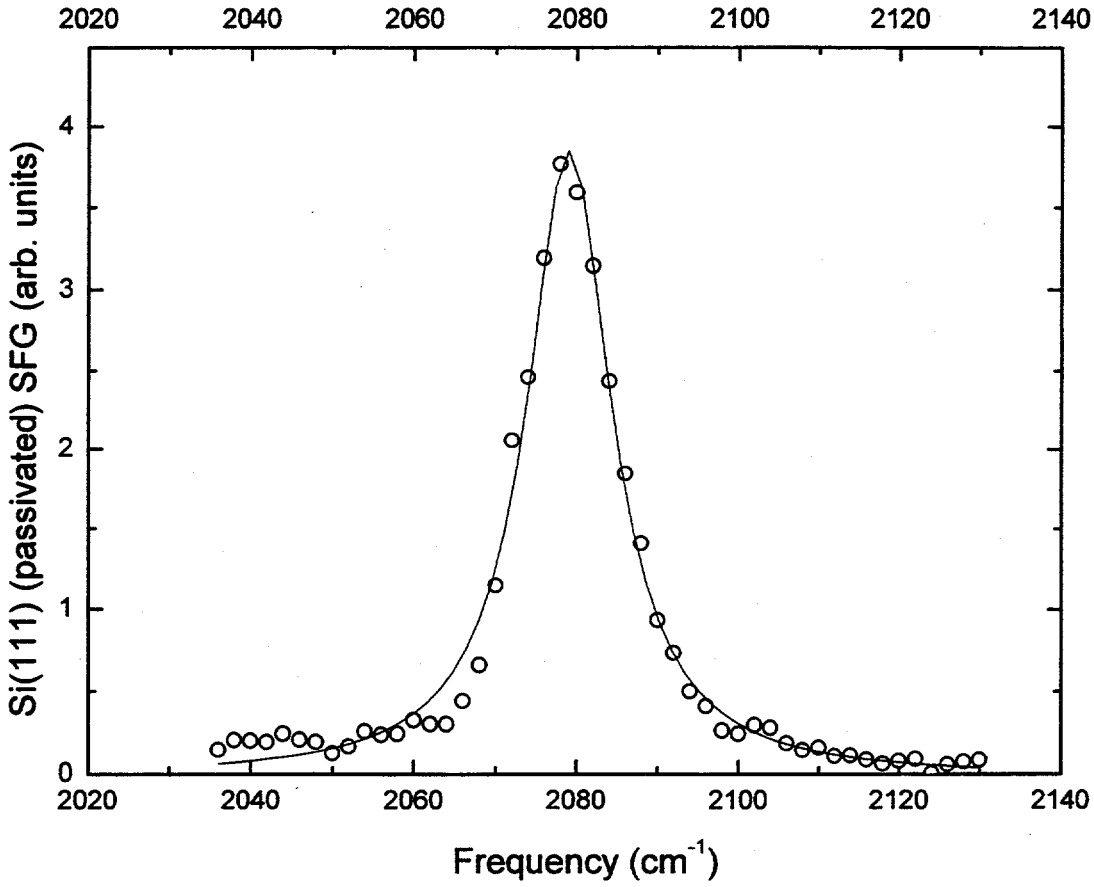
2020
2040
2060
2080
2100
2120
2140
0
1
2
3
4
Si(111) (passivated) SFG (arb. units)
Frequency (cm-1)

Fig. 6

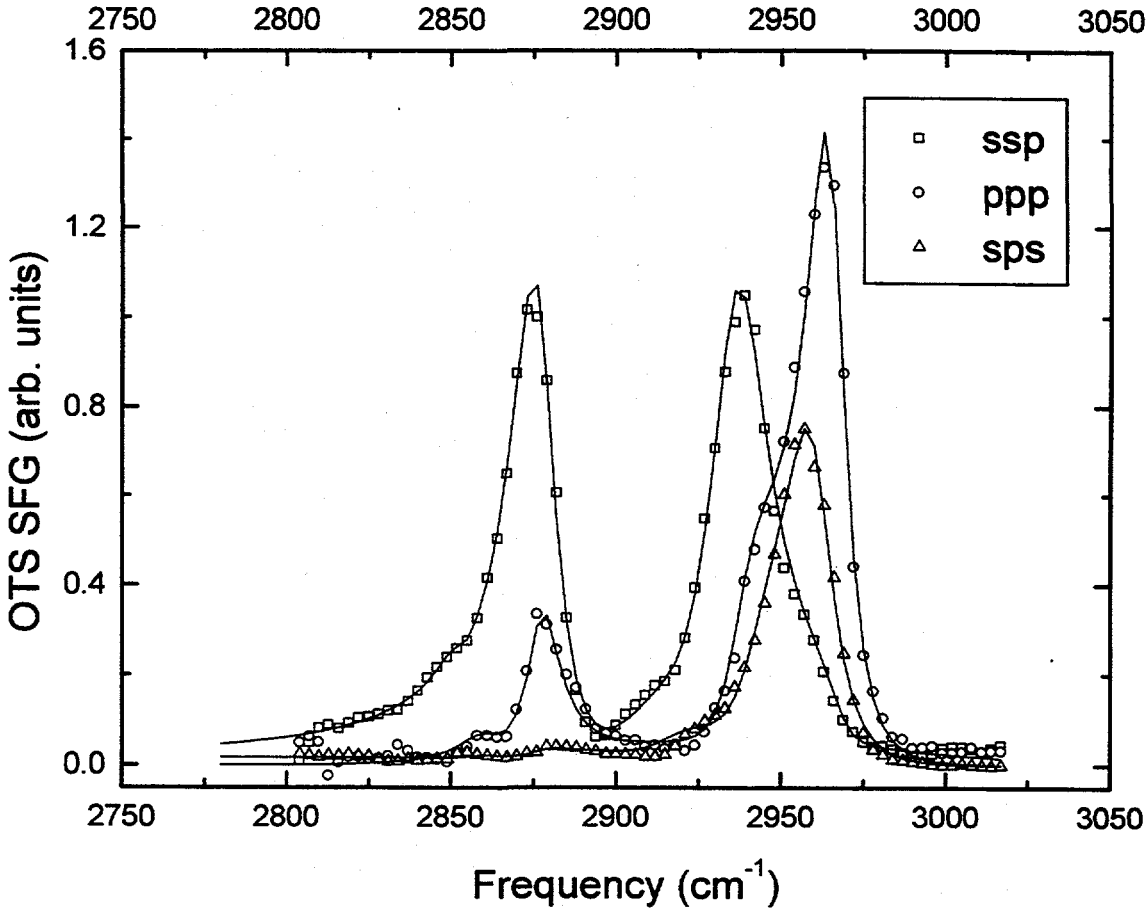
2750
2800
2850
2900
2950
3000
3050
1.6
1.2
0.8
0.4
0.0
OTS SFG (arb. units)
ssp
ppp
sps
Frequency (cm-1)

Fig. 7

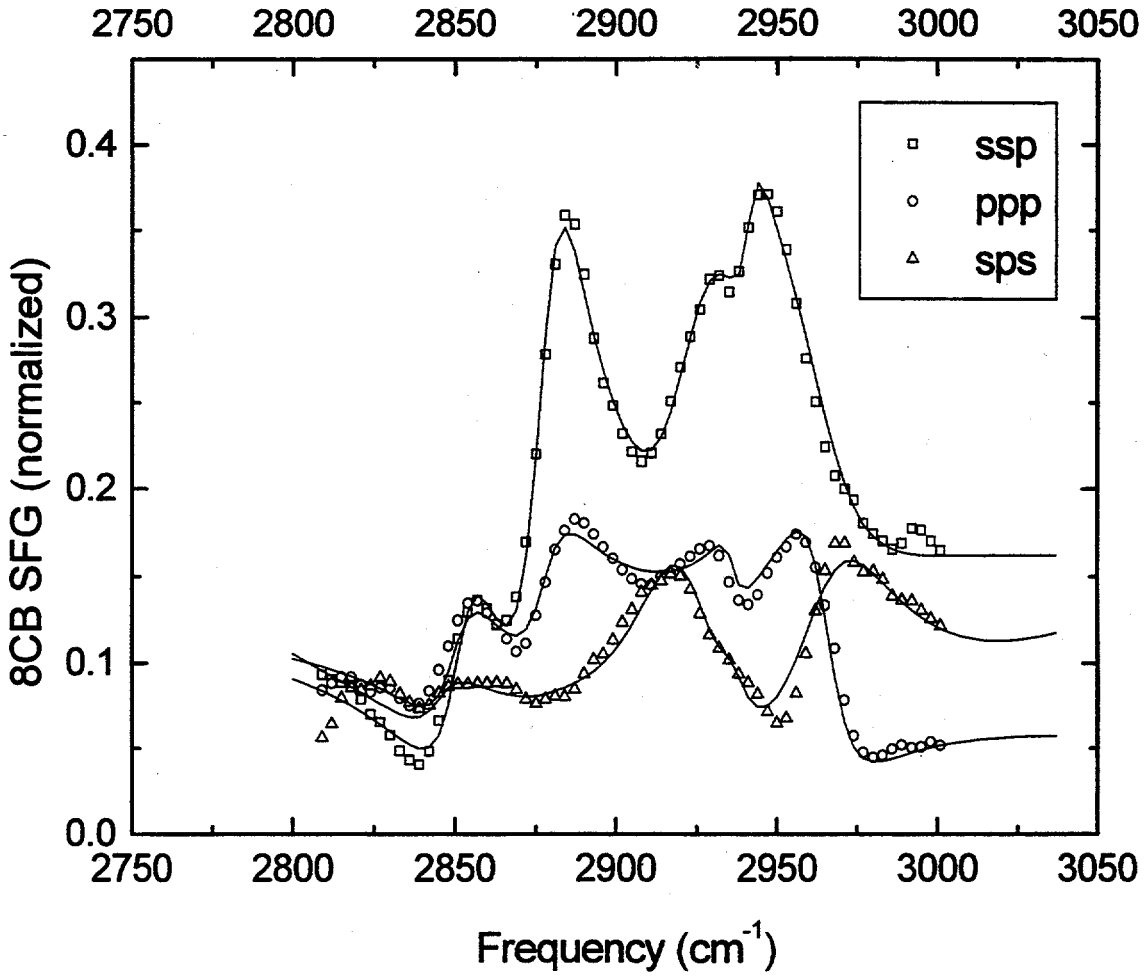
2750
2800
2850
2900
2950
3000
3050
0.4
0.3
0.2
0.1
0.0
8CB SFG (normalized)
ssp
ppp
sps
Frequency (cm-1)

Fig. 8

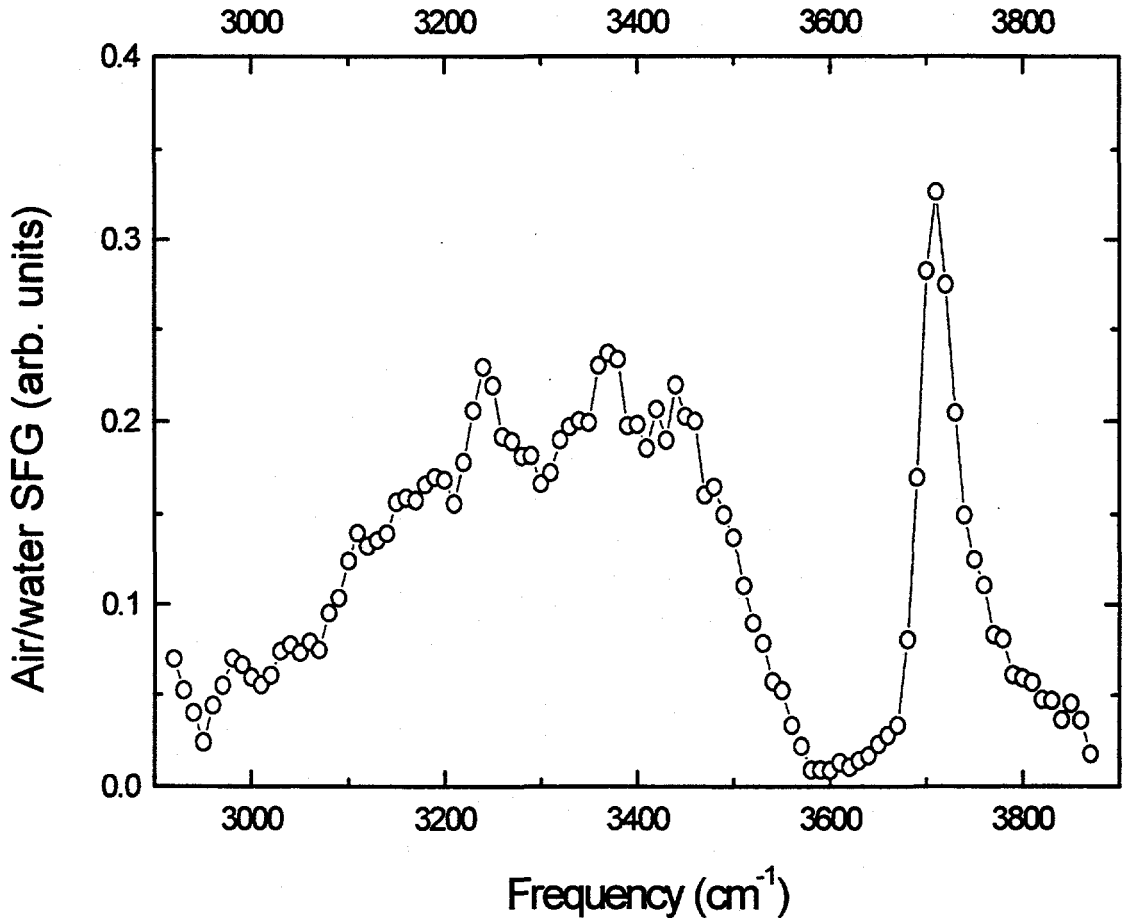
3000
3200
3400
3600
3800
0.4
0.3
0.2
0.1
0.0
Air/water SFG (arb. units)
Frequency (cm-1)

Fig. 9

Chapter 4

Multiphoton Photoluminescence from Semiconductors

4.1 Multiphoton Photoluminescence from Porous Silicon

The discovery of efficient visible luminescence from room–temperature porous Si in 1990 [1] has stimulated a tremendous amount of interest about the material as it could lead to novel Si–based optoelectronic devices. More than 3000 papers have already been published on porous Si. Among them a large fraction focused on its photoluminescence properties. Yet hardly any deals with multiphoton excitations of luminescence [2, 3, 4]. it is generally believed that porous Si can be regarded as a system of loosely connected Si clusters [1]. The average size of the

clusters can be controlled by etching. Both absorption and luminescence spectra of porous Si have been found to exhibit the quantum–size effect [1, 5, 6]. Not only are the bandedge frequencies of absorption and luminescence blue–shifted with decrease of the cluster size, but the transition strengths are enhanced because of confinement of electrons and holes [7]. The latter feature suggests that for a multiphoton transition process, the enhancement can be much stronger than that for a one–photon process. This indeed seems to be the case. In a bulk Si (or semiconductor and metal in general), three–photon excitation can hardly be observed before laser breakdown of the sample occurs, but in porous Si, the same process is easily measurable at room temperature [2, 3, 4]. In fact, even an eight or nine–photon excitation in porous Si is readily detectable via photoluminescence [3, 4]. This makes multiphoton excitation of photoluminescence interesting and worth investigating.

The other motivation of our study is the fact that although one–photon–excited photoluminescence in porous Si has been studied extensively, there is still argument on whether it originates from quantum–confined bulk structure or from surface regions with involvement of surface states [7]. Hopefully the study of multiphoton–excited photoluminescence can provide some clues to this question.

We have used in our study a picosecond OPG/OPA system described in detail in the last chapter to excite photoluminescence in porous Si. The results indicate that direct excitations into surface states and subsequent luminescence from these states are possible. Visible luminescence at $\sim$680 nm induced by multiphoton

excitation of infrared radiation at wavelength ≤ 5.3 μm can be easily detected.

The porous Si films used in our study were prepared by anodic etching of crystalline Si(100) wafers in an electrochemical cell containing 1:1 mixture of 49 % HF in water and pure ethanol by volume [7]. Those prepared on an n-type Si samples were etched under UV radiation. The size of the nanocrystallities in the samples was around 5–10 nm and could be further reduced by post–stripping the samples in HF. The samples were characterized by optical absorption measurement in the energy range 1.1–3.8 eV [8] and FTIR spectroscopy in the 1900–2400 cm^{-1} (0.23–0.30 eV) range, and by their luminescence spectra obtained with above bandgap, one–photon excitation. A typical example is shown in Fig. 4.1 for absorption measurements and Fig. 4.2 for photoluminescence. At room temperature, the UV–excited photoluminescence efficiency was $\sim$5 %, and its decay time was in the μs range. The FTIR spectra indicated that the freshly prepared samples were surface–passivated mainly by hydrogen termination, but when exposed to air they became gradually oxidized by replacing SiH_X with SiO_X and $OSiH_X$ species on the surface [9]. The electronic absorption edge exhibited a long tail extended into the mid–IR region, which is generally attributed to surface states [7].

The laser system used in our experiment for multiphoton excitation was from an optical parametric generator/amplifier pumped by an active–passive mode–locked Nd:YAG laser as described in detail in Chap. 3. The system produced tunable 15 ps pulses at 20 Hz with an energy larger than 100 μJ/pulse in the tuning range 0.4 μm – 5.3 μm. The beam can be focused to $\sim$2 GW/cm^2 on porous

Si without causing any degradation of the sample. To vary the pump intensity, calibrated neutral density filters were used in the visible and near infrared range and Ge plates of different surface coatings were used in the mid infrared range. Photoluminescence from the sample was collected after spectral filtering by a photomultiplier and a gated electronic system. To measure photoluminescence close to the pump wavelength, interference filters were used before the monochromator to block the scattered pump light. All measurements were performed with the sample in air and at room temperature. The setup of photoluminescence excitation and detection system is shown in Fig. 4.3. In the following, unless specified, the results presented were from an n–type porous Si film.

The photoluminescence spectra from porous Si induced by picosecond pulse excitation of different wavelengths, 0.46, 0.9, 1.06, 1.4, and 4.88 μm, (corresponding to photon energies of 2.7, 1.38, 1.17, 0.86, and 0.25 eV, respectively) are presented in Fig. 4.2. While in all cases, luminescence appears in the red–yellow range, the peak of luminescence is red–shifted and becomes broader with increase of excitation wavelength. Note that to generate one luminescence photon at 2 eV and above, we need absorption of at least one, two, three, and eight photons, respectively, at the above–listed excitation wavelengths. The above–mentioned red shift of luminescence indicates that the multiphoton excitation must be multi–resonant and multi–step presumably via the surface or defect states because otherwise a direct one–step multiphoton excitation to an energy level above the luminescence band would yield a luminescence spectrum identical to that obtained by one–photon ex-

citation to the same level. Luminescence from the lower states in the energy band tail and relaxation to lower surface states during the multi–resonant, multi–step excitation process could lead to a luminescence spectrum weighted more toward low–frequency side.

One would expect that luminescence induced by an n–photon excitation should have a pump intensity dependence of I^n. This is however only true in the weak perturbation limit. In out case of high–intensity excitation with strong pumping at intermediate resonant steps, the I^n dependence can have an n very different from the number of absorbed photons required to excite the system to a level above the luminescence band. Figure 4.4 displays the experimental result: an I^1 dependence in the 0,35–0.71 μm excitation range, an I^2 dependence in the 0.85–1.7 μm range, and an I^3 dependence in the 1.9–4.8 μm range. The fact that most of the IR excitation has an I^n dependence with n less than the number of absorbed photons required for luminescence indicates the presence of strong pumping at intermediate resonant steps. Consider, for example, excitation at 4.5 μm. The I^3 dependence of the induced luminescence suggests that the initial three–photon excitation to the midgap surface (defect) states is the limiting step in the overall seven or eight–photon excitation process. Presumably following the three–photon excitation to the midgap states, the system could be pumped by one–photon resonant steps via the surface states all the way up until it reaches a level where luminescence and nonradiative decays compete with and suppress the up–pumping. As expected, the luminescence intensity drops rapidly when the

number of absorbed photons required for luminescence increases. For example, at the excitation intensity of 0.07 GW/cm^2, the luminescence intensity already drops by more than six orders of magnitude as the pump wavelength changes from 0.52 μm to 1.55 μm and by another two to three orders as the wavelength further increases to 4.5 μm.

One would ask whether the mid–IR multi–photon–excited luminescence can be affected by vibrational resonances of surface species like SiH_X and $OSiH_X$ passivating the surface of porous Si. In an earlier study on a p–type Si(100) sample [3], the excitation spectrum showed a broad peak that coincided with the SiH_X stretch vibrational resonances at low pump intensities, but shifted to lower frequencies at high pump intensities. The result provided us to propose a model of multiphoton excitation via vibrational ladders, analogous to that of polyatomic molecules, to explain the observation. However, we now have found that the excitation spectrum for porous Si prepared from an n–type Si(100) substrate is different. Figure 4.5(a) shows a typical FTIR spectrum of the Si–H stretch vibrations for such a sample. The 2110 cm^{-1} absorption peak comes from the SiH_X surface species while the 2260 cm^{-1} one comes from $OSiH_X$. The relative strength of the two peaks depends on the degree of oxidation of the sample. For a freshly prepared sample, the spectrum is dominated by the SiH_X stretch peak. With pump radiation in this spectral range (4.4 –5.3 μm or 1900 –2300 cm^{-1}), the observed visible luminescence had an I^3 dependence on the excitation intensity although energy conservation would require the absorption of at least seven to nine IR photons

for emission of one visible photon. The photoluminescence excitation spectrum in this range for the sample of Fig. 4.5(a) is depicted in Fig. 4.5(b). The relative strength of the two dips in Fig. 4.5(b) is well correlated with that of the absorption peaks in Fig. 4.5(a). This is true for a series of samples with different degrees of oxidation that yielded different relative strengths of the two absorption peaks, as shown in Fig. 4.6.

The result of Fig. 4.5 from the n–type sample seems to suggest that vibrational resonances of surface species were involved in the multiphoton excitation. However, a close look at the sample revealed that the n–type porous Si was composed of two layers. The top layer was $\sim$ 1 μm thick, had cluster sizes of $\sim$ 5 nm, and exhibited visible luminescence under UV excitation. The underlying second layer was $\sim$ 30 μm thick. Because of the limited UV penetration depth in Si, this layer was created by etching without the influence of UV radiation. Consequently, the cluster size of the layer was $\geq$10 nm. Measurements on samples that had the top layer stripped off showed that no strong visible luminescence could be detected from this underlying layer, but the deep red and near–IR luminescence (corresponding to the spectrum obtained with the 4.88 μ, excitation in Fig. 4.2) observed from porous Si under mid–IR multiphoton excitation appeared to come entirely from this layer. The excitation spectrum in the mid–IR region is displayed in Fig. 4.5(c); it now exhibits no dips at the SiH_X and $OSiH_X$ vibrational resonances. Obviously the dips seen in the earlier excitation spectrum (Curve (b) in Fig. 4.5) must have resulted from IR absorption in the top layer at

those vibrational resonances. Careful IR absorption measurements of the samples showed that 50–60 % of the input beam was absorbed by the top layer at the vibrational resonance peaks. Knowing the IR intensity $I(\omega)$ transmitted through the top layer and incident on the underlying layer and knowing that the observed luminescence has an $I(\omega)^3$ dependence, we can calculate how the vibrational resonances affect the excitation spectrum. As illustrated in Fig. 4.5, it fits well with the experimental observation.

In summary, we have observed multiphoton–excited luminescence from porous Si. The quantum confinement effect or the more localized surface excitations may have such a process more easily observable in porous Si than in bulk Si. Visible photoluminescence induced by IR excitation down to 1900 cm^{-1} has been measured. At $\sim$ 2000 cm^{-1}, absorption of at least 8 or 9 photons is needed to generate one visible luminescent photon. The IR multiphoton excitation could in principle be a one–step direct process. However, because of the existence of surface states in the bandgap of porous Si, it is more likely a multi–resonant and multi–step process. The system reaches a certain energy level after each step; depending on the pumping strength, it can be pumped further up or drop to lower levels via luminescence or nonradiative decay. At sufficiently high energy levels, the probability of having the system pumped further up should become negligibly small. In such a multiphoton excitation process, surface states must be involved if they do exist in the bandgap of porous Si, and the red–shifted luminescence may also have originated from the surface states.

4.2 Multiphoton Photoluminescence from GaN

Recently there has been a great deal of interest in the study of wide bandgap semiconductors because of their potential applications to electronics and opto-electronics [11]. Among them, GaN particularly has attracted much attention for its being the most promising material for construction of blue lasers and blue luminescent devices. The wurtzite GaN crystal has a direct bandgap of 3.4 eV at room temperature. Excitations above the bandgap usually give rise to a luminescence with two characteristic spectral peaks: one at ~3.35 eV is identified as the bandedge emission and the other at ~ 2.3 eV has been assigned to transitions from shallow donor to deep midgap states [12, 13, 14]. While linear optical properties of GaN have been studied extensively [11, 15], the reported nonlinear optical measurements are mainly on its second and third–order nonlinear susceptibilities [16].

In this part of the thesis, we describe our recent experiments on multiphoton–excited luminescence from GaN. With sufficiently intense picosecond pump pulses, even a five–photon–excited luminescence process could be readily observed. The excitation spectrum of the two–photon–excited luminescence reflects directly the two–photon absorption spectrum of GaN for the valence–conduction interband transition if no intermediate resonances are involved. In a measurement with two tunable input beams, however, the two–photon excitation actually exhibited an intermediate resonance at ~1 eV. This provides a direct evidence for the existence of midgap states responsible for the yellow luminescence at 2.3 eV.

The GaN sample used in our experiment was grown on the basal plane of a sapphire substrate by the metalorganic chemical–vapor deposition (MOCVD) method. A buffer layer (500 Å) of AlN was first deposited on sapphire at 400 °C and then the wurtzite GaN layer was grown on AlN at 1100 °C. The source materials were trimethylaluminum (TMA), trimethylgallium (TMG), and NH_3. The flow rates were 88 μmol/min for TMA, 44 μmol/min for TMG, and 10 L/min for NH_3. The polycrystalline GaN layer was 3.4 μm thick with an n–type carrier concentration in the low 10^{17} cm^{-3} presumably due to Si impurities and N vacancies.

Our PL experiment was carried out using the optical parametric generator/amplifier system as described in Chap. 3. The experimental setup is is the same as that for the porous silicon experiment and is shown in Fig. 4.3. The output from the OPG/OPA system was weakly focused on the room–temperature sample along the optic (hexagonal c) axis with a maximum intensity of 0.5 GW/cm^2 to assure absence of laser damage. Photoluminescence (PL) from the sample was collected and sent through a monochromator to be spectrally analyzed, and finally detected by a photomultiplier and a gated integrator.

The solid curve in Fig. 4.7 is the PL spectrum of our GaN sample obtained by weak, one–photon excitation at 3.5 eV using the third–harmonic output of the picosecond pulsed Nd:YAG laser. Similar to those reported in the literature, it consists of a near–bandedge emission peak at 3.35 eV with a shoulder at 3.4 eV (transition from conduction band/shallow donor states to valence band states)

and a weak broad yellow luminescence peak centered around 2.3 eV [12, 13, 14]. The full–width at half maxima of this bandedge emission was 17 nm (150 meV). To see whether multiphoton excitation induces the same luminescence, we also present in Fig. 4.7 the PL spectra of the bandedge peak obtained with several different pump frequencies. The different curves in Fig. 4.7 are normalized to the same peak height. They do appear nearly the same, although the peak widths of the multiphoton–excited PL seem to be somewhat broader mainly because of the poorer monochromator resolution used in the measurement.

We have studied the pump intensity dependence of the multiphoton–excited PL at various pump wavelengths. Figure 4.8 describes the results of a few selected cases. Here, PL was collected through a monochromator set at 370 nm with a 20 nm passing bandwidth. For pump wavelengths between 0.4 and 0.7 μm (corresponding to 3.1 and 1.77 eV), an I^2 dependence was observed, where I is the pump intensity. This indicates that the excitation was a direct two–photon process as one would expect from the relation $\hbar\omega_p < E_g < 2\hbar\omega_p$, with ω_p being the pump frequency and E_g the bandgap. As the pump wavelength increased from 0.75 to 1.1 μm (1.65 to 1.13 eV), the observed pump intensity dependence changed gradually from I^2 to I^3 while the expected dependence from a direct multiphoton–excited PL should be I^3. For pump wavelength between 1.1 and 1.7 μm (1.13 — 0.73 eV), I^n with $n \geq 4$ is expected for direct excitation, but $I^{3.2}$ was observed. The deviation can be explained if the multiphoton excitation process involves saturable intermediate resonances. This appears to be the case in GaN as we shall discuss later.

Figure 4.9 displays the photoluminescence excitation (PLE) spectrum taken with pump intensity fixed at 0.3 GW/cm^2. In this measurement, PL was again collected through a monochromator set at 370 nm with a 20 nm bandwidth. Most notable feature in the PLE spectrum is the sudden drop when the pump photon energy $\hbar\omega_p$ decreases below $E_g/2 \sim 1.7$eV as the two–photon excitation changes over to three–photon excitation. We expect that in the range of $\hbar\omega_p < E_g < 2\hbar\omega_p$, the PLE spectrum essentially reflects the two– photon absorption spectrum assuming that the luminescence efficiency is independent of the excitation. For $2\hbar\omega_p \sim E_g$, we have from the two–band parabolic approximation the following expression for the two– photon absorption (TPA) coefficient for a direct–gap semiconductor [17]

$$\begin{aligned} \beta(\omega_p) &= K_{pb}\frac{\sqrt{E_p}}{n(\omega_p)^2 E_g^3}\frac{(2x-1)^{3/2}}{(2x)^5} \qquad \text{for} \quad x \geq \frac{1}{2} \\ &= 0 \qquad\qquad\qquad\qquad\qquad\qquad\quad \text{for} \quad x < \frac{1}{2} \end{aligned} \tag{4.1}$$

where $K_{pb} = 1940$ cm/GW(eV)$^{5/2}$ is the material independent parameter, $E_p = \frac{2}{m}|\langle s|p_i|x_i\rangle|^2$=18 eV for GaN ($|s\rangle$ and $|x_i\rangle$ are the wavefunctions of conduction and valence bands, respectively, and p_i is the momentum operator.), $n(\omega_p)$ is the index of refraction at ω_p, and $x = \hbar\omega_p/E_g$. The solid curve in Fig. 4.9 is calculated from Eq. (4.1) to compare with the observed PLE in the $\hbar\omega_p \geq E_g/2$ region and the fit appears quite satisfactory. The estimated two–photon absorption coefficient for GaN at 2 eV is $\sim$1 cm/GW. Given a sample thickness of 3.4 μm as in our case and a laser intensity of 0.3 GW/cm^2, the two–photon absorption is only $\sim 10^{-4}$. This makes quantitative measurement of two–photon absorption difficult, but via PLE, the two–photon absorption spectrum can be obtained fairly easily.

For $\hbar\omega_p$ below 1.7 eV, we need at least 3 photons to excite the electrons above the bandgap and accordingly, PLE decreases by more than an order of magnitude, as shown in Fig. 4.9. We would expect another drop in PLE as $\hbar\omega_p$ decreases below $E_g/3$ =1.13 eV since one more photon is needed to excite the electrons across the bandgap. However, the observed PLE actually increases and exhibits a peak at ~0.95 eV. After the peak, the PLE decreases rapidly as expected. This suggests that there is an intermediate resonance at ~0.95 eV in the multiphoton excitation process. We can actually relate it to the midgap impurity or defect states involved in the emission of yellow luminescence at 2.3 eV often seen from GaN samples [12, 13, 14]. Hofmann *et al.* [13] and Perlin *et al.* [14] have investigated the origin of this omnipresent yellow luminescence and concluded that it is due to transitions from the shallow donor to the deep midgap states. These midgap states should be about 1 eV above the valence band maximum. Therefore in the multiphoton excitation of photoluminescence we can expect a resonance enhancement at ~1 eV due to transitions from the valence band to these midgap states. Pump saturation at this resonant step would then make the overall multiphoton excitation process at ~1 eV appear to have a pump intensity dependence of $\sim I^3$, as shown in Fig. 4.8.

To further confirm the existence of these midgap states, we employed a two–photon, two– color excitation scheme instead of the above–mentioned multiphoton excitation scheme. The optical parametric generator/amplifier (OPG/OPA) system we used generated simultaneously two tunable coherent beams of frequen-

cies ω_1 and ω_2, but the sum frequency $\omega_1 + \omega_2$ was fixed at 3.5 eV (corresponding to a wavelength of 355 nm), which is slightly above the bandgap of GaN. With both ω_1 and ω_2 beams impinging on the sample, the two–photon excited PL was easily observed. Tuning of ω_1 and ω_2 with $\omega_1 + \omega_2$ fixed allowed us to scan over possible intermediate resonances without changing the final level of excitation. Indeed as shown in Fig. 4.10, the PLE spectrum as a function of ω_1 exhibits a resonance peak at $\sim$1 eV. In the experiment, the intensities of the ω_1 and ω_2 beams were about 0.07 GW/cm^2 and 0.3 GW/cm^2, respectively. With the ω_1 beam alone, the PL was hardly detectable. With the ω_2 beam alone, the PL was less than 1/3 of the peak value shown in Fig. 4.10 and no resonant features could be detected throughout the tuning range. The result of Fig. 4.10 provides a direct evidence of the existence of the midgap states at $\sim$1 eV above the valence band. The resonant peak width of 145 meV is also comparable with the width of the 2.3 eV yellow luminescence.

In conclusion, we have observed a bandedge photoluminescence from GaN with multiphoton excitation using tunable picosecond pump pulses. The PL was easily detectable even with moderate pump intensity. The pump intensity dependence of the PL gets more nonlinear as the pump wavelength is increased as expected. The PLE spectrum of single–color, two–photon excitation near the bandgap agrees qualitatively with the theoretical two–photon absorption spectrum. The PLE spectrum of four–photon excitation shows a resonant peak at $\sim$1 eV. This peak arises from an intermediate resonance due to transitions from the

valence band to the midgap defect states. The same resonant transitions are also observed in the two–color, two–photon–excited PLE spectrum.

Bibliography

[1] L. T. Canham, Appl. Phys. Lett. **57**, 1046 (1990).

[2] X. Wang *Porous Silicon*, edited by Z. Chuan and R. Tsu (World Scientific, River Edge, NJ, 1994), p. 77–98; J. Wang *et al.*, Phys. Rev. Lett. **69**, 3252, (1992).

[3] R. P. Chin, Y. R. Shen, and V. Petrova–Koch, Science, **270**, 776 (1995).

[4] J. Diener, M. Ben–Chorin, D. I. Kovalev, S. D. Ganichev, and F. Koch, Phys. Rev. B **52**, R6817 (1995).

[5] V. Lehmann and U. Gosele, Appl. Phys. Lett. **58**, 856 (1991); D. J. Lockwood, A. Wang, and B. Bryskiewicz, Solid State Comm. **89**, 587 (1994); Y. Kanemitsu *et al.*, Phys. Rev. B **48**, 2827 (1993).

[6] A. G. Cullis and L. T. Canham, Nature **353**, 335 (1991).

[7] F. Koch, V. Petrova–Koch, and T. Muschik, J. Luminescence, **57**, 271 (1993); D. J. Lockwood, Solid State Comm. **92**, 101 (1994).

[8] D. Kovalev, G. Polisski, M. Ben–Chorin, J. Diener, and F. Koch, J. Appl. Phys. **80**, 5978 (1996).

[9] T. Maruyanna and S. Ohtani, Appl. Phys. Lett. **64**, 280 (1994).

[10] J. Y. Zhang, J. Y. Huang, Y. R. Shen, and C. Chen, J. Opt. Soc. Am. B **10**, 1758 (1993).

[11] See, for example, S. Strite and H. Morkoc, J. Vac. Sci. Technol. B **10**, 1237 (1992); H. Morkoc *et al.*, J. Appl. Phys. **76**, 1363 (1994).

[12] T. Ogino and M. Aoki, Jpn. J. Appl. Phys. **19**, 2395 (1980).

[13] D. M. Hofmann *et al.*, Phys. Rev. B **52**, 16702 (1995).

[14] P. Perlin *et al.*, Phys. Rev. Lett. **75**, 296 (1995); T. Suski *et al.*, Appl. Phys. Lett. **67**, 2188 (1995).

[15] J. I. Pankove, H. P. Maruska, and J. E. Berkeyheiser, Appl. Phys. Lett. **17**, 197 (1970); S. Logothetidis, J. Petalas, M. Cardona, and T. D. Moustakas, Phys. Rev. B **50**, 18017 (1994); W. R. L. Lambrecht, B. Segall, J. Rife, W. R. Hunter, and D. K. Wickenden, Phys. Rev. B **51**, 13516 (1995).

[16] J. Miragliotta, D. K. Wickenden, T. J. Kistenmacher, and W. A. Bryden, J. Opt. Soc. Am. B **10**, 1447 (1993); J. Miragliotta and D. K. Wickenden, Phys. Rev. B **50**, 14960 (1994); **53**, 1388 (1996).

[17] C. C. Lee and H. Y. Fan, Phys. Rev. B **9**, 3502 (1974); B. S. Wherrett, J. Opt. Soc. Am. B **1**, 67 (1984); E. W. Van Stryland *et al.*, Opt. Eng. **24**, 613 (1985); D. C. Hutchings and E. W. Van Stryland, J. Opt. Soc. Am. B **9**, 2065 (1992); J. A. Bolger *et al.*, Opt. Commun. **97**, 203 (1993).

Figure Captions

Figure 4.1: Absorption spectra of porous Si. (a) Electronic absorption in the 1.1 to 3.8 eV range. The experimental details of this absorption measurement can be found in Ref. [8]. (b) Absorption in the 0.23–0.30 eV range due to vibrational resonances of the surface SiH_x (2110 cm^{-1}) and $OSiH_x$ (2260 cm^{-1}).

Figure 4.2: Photoluminescence spectra of n–type porous Si film with 2.7, 1.38, 1.17, 0.86, and 0.25 eV (corresponding to 0.46, 0.9, 1.06, 1.4 and 4.88 μm, respectively) pump excitations.

Figure 4.3: Experimental setup. F: color filter or neutral density filter; L1: CaF_2 focusing lens, $f = 4$ cm; L2: collecting lens, $f = 5$ cm.

Figure 4.4: photoluminescence signal as a function of pump intensity for different pump wavelengths

Figure 4.5: (a) Vibrational absorption spectrum of an n–type porous Si in the Si–H stretch region. (b) Corresponding excitation spectrum of multiphoton–excited luminescence from the same sample; the solid line is a theoretical fit. (c) Excitation spectrum of multiphoton–excited luminescence from the sample with the top layer stripped.

Figure 4.6: Absorption spectra (solid lines) and PLE spectra (circles) of n–type porous silicon samples with varying degrees of oxidation. The top graph is for the freshly etched sample and the degree of oxidation increases from top to bottom.

Figure 4.7: Photoluminescence spectra of GaN. Solid line is for above–bandgap (at 3.5 eV) excitation; all the other lines are for multiphoton excitations at different pump wavelengths.

Figure 4.8: Intensity dependence of PL with different excitation wavelength. Solid line: I^2. Dotted line: $I^{2.5}$. Dashed line: $I^{3.2}$.

Figure 4.9: Photoluminescence excitation (PLE) spectrum of GaN obtained with pump intensity fixed at 0.3 GW/cm^2. Solid line is a theoretical curve describing two–photon absorption in GaN near the bandgap using the parabolic band approximation.

Figure 4.10: Photoluminescence excitation spectrum of GaN with two–photon, two–color excitations. Sum of the two photon energies is fixed at 3.5 eV (355 nm) and only the infrared photon energy ($\hbar\omega_1$) is shown as a variable in the plot. The solid line is a Gaussian fit to the data with the peak position 1.0 eV and a peak width of 145 meV.

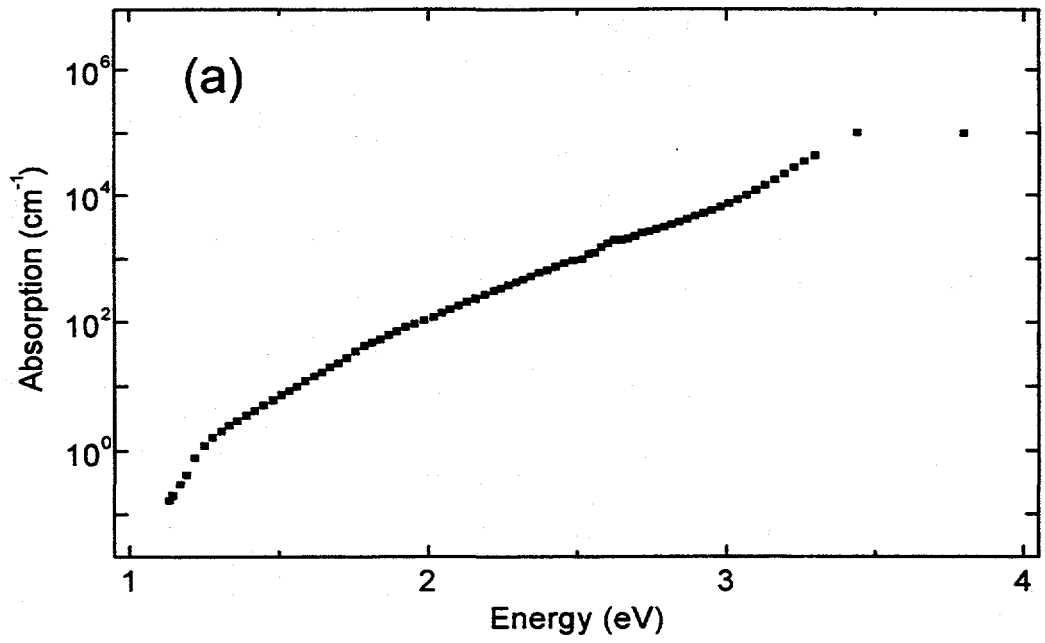
(a)
Absorption (cm^{-1})
10^6
10^4
10^2
10^0
1
2
3
4
Energy (eV)

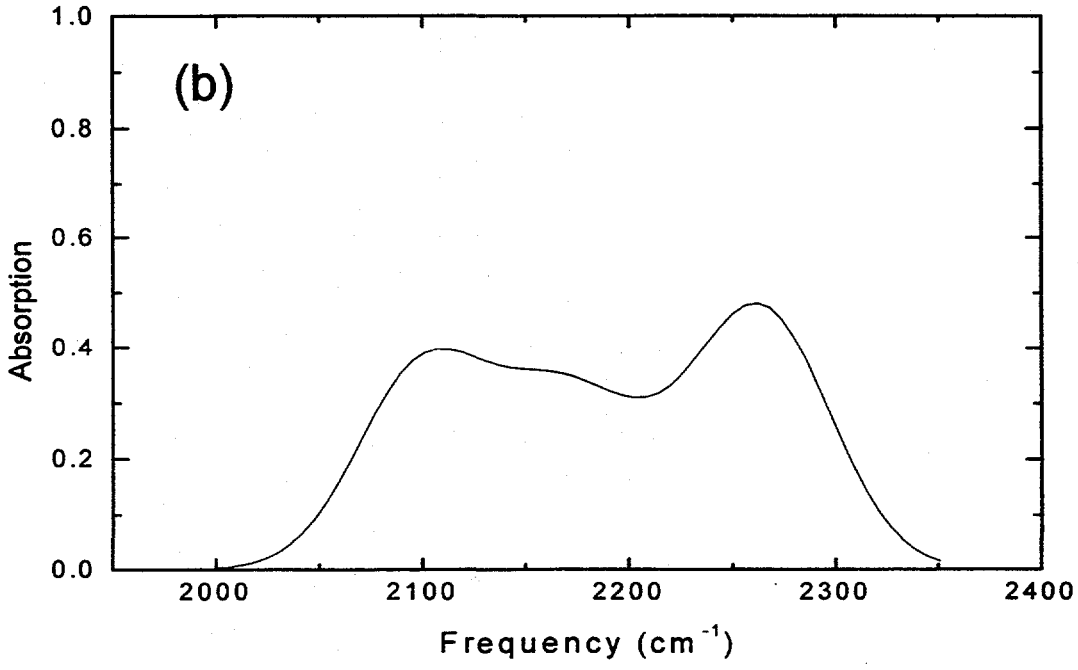
(b)
Absorption
1.0
0.8
0.6
0.4
0.2
0.0
2000
2100
2200
2300
2400
Frequency (cm^{-1})

Fig. 1

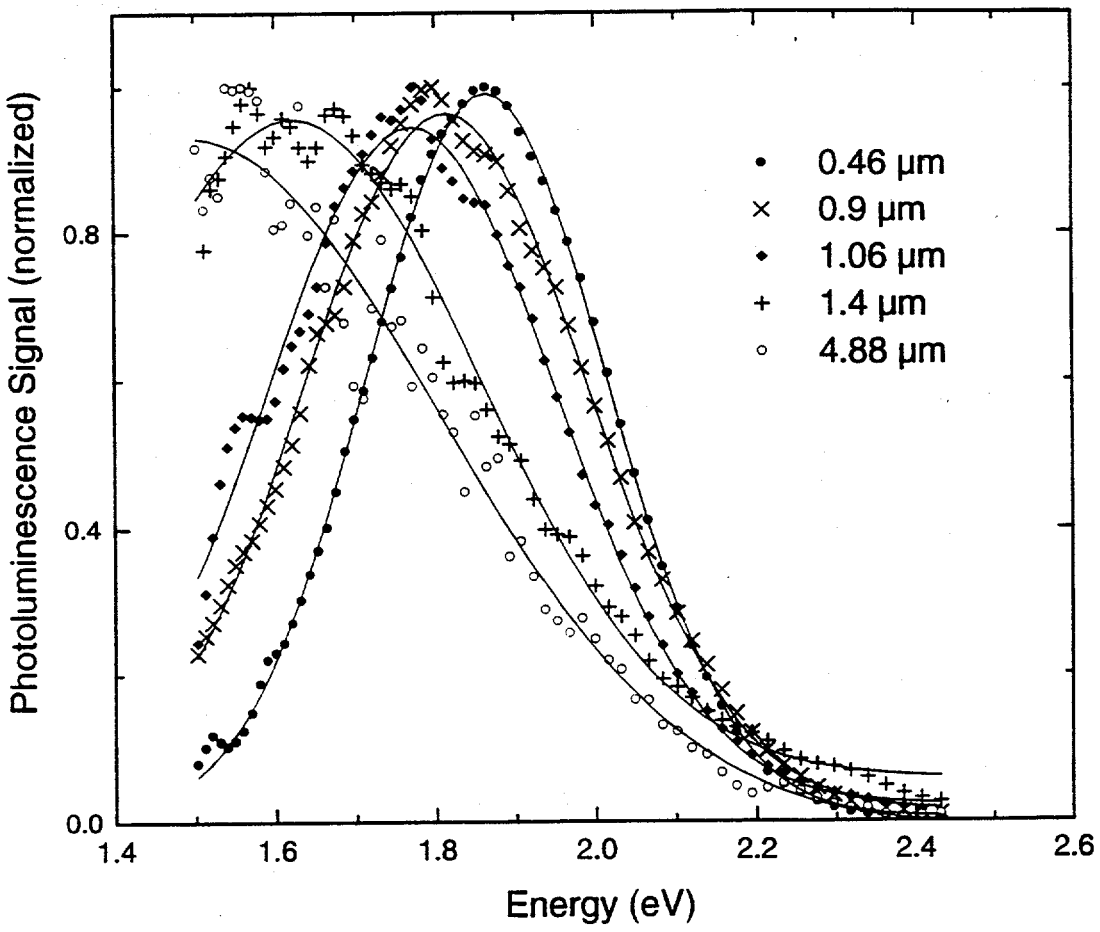
Photoluminescence Signal (normalized)
0.0
0.4
0.8
1.4
1.6
1.8
2.0
2.2
2.4
2.6
Energy (eV)
0.46 μm
0.9 μm
1.06 μm
1.4 μm
4.88 μm

Fig. 2

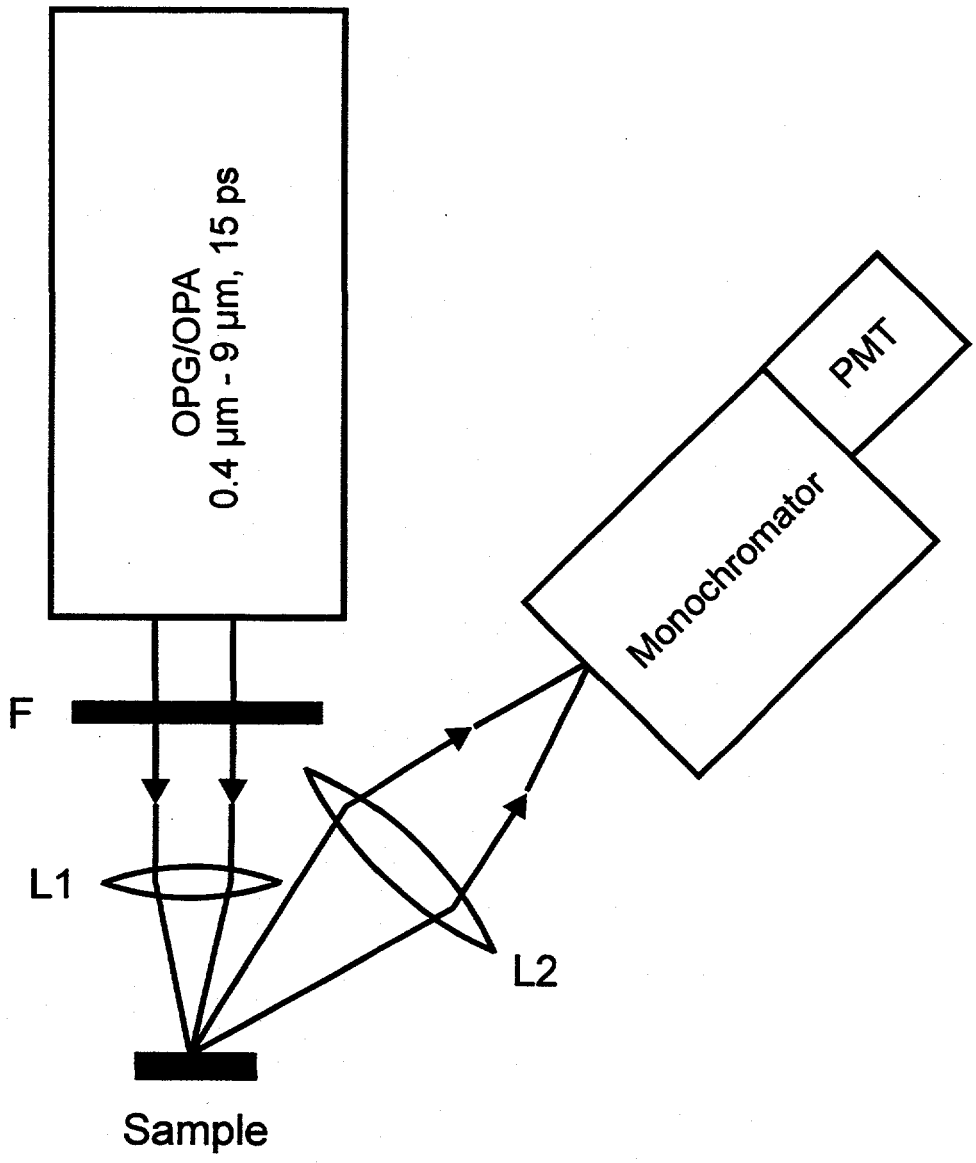

Fig. 3

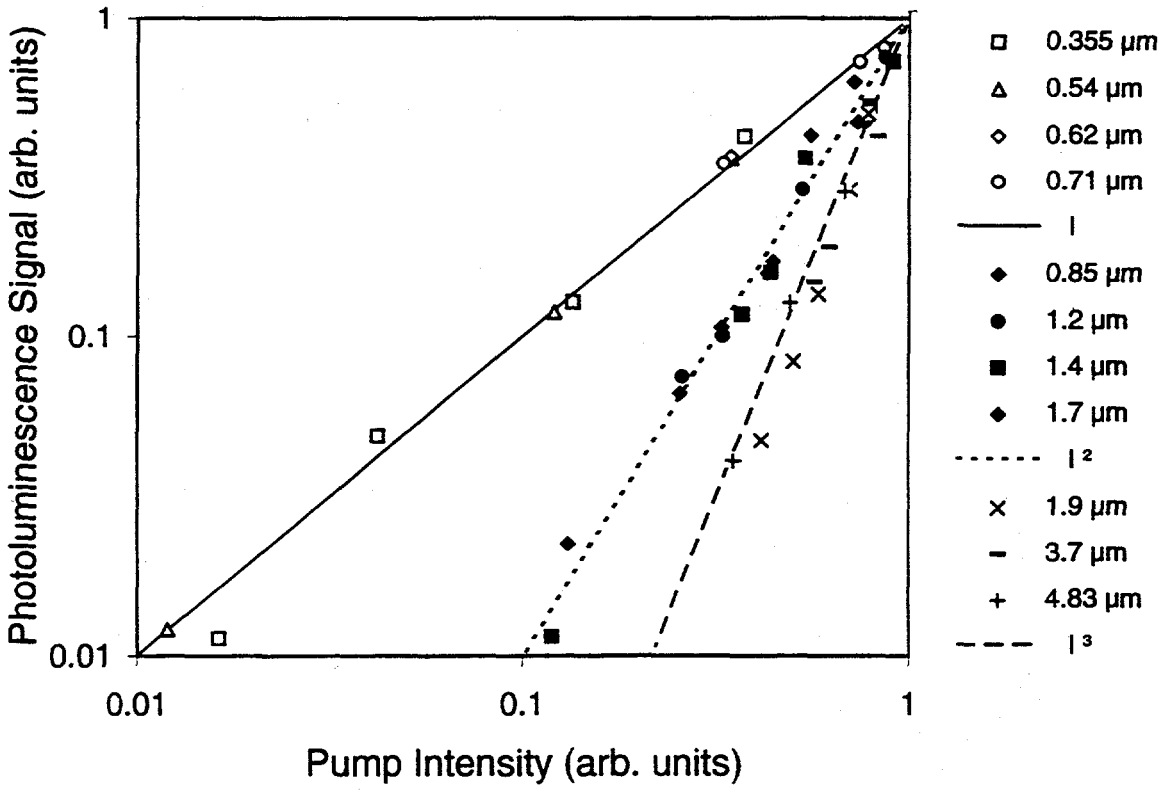
Photoluminescence Signal (arb. units)
1
0.1
0.01
0.01
0.1
1
Pump Intensity (arb. units)
0.355 µm
0.54 µm
0.62 µm
0.71 µm
I
0.85 µm
1.2 µm
1.4 µm
1.7 µm
I²
1.9 µm
3.7 µm
4.83 µm
I³

Fig. 4

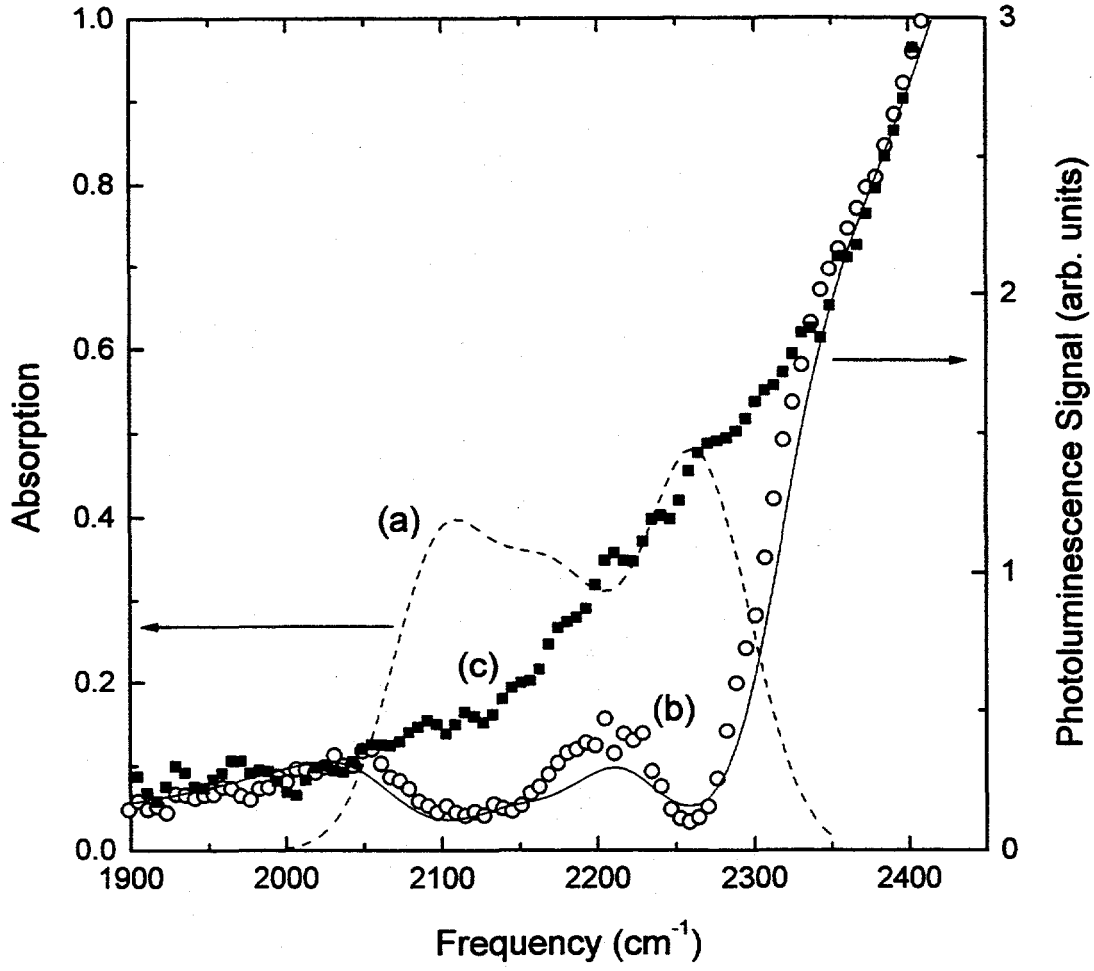
1.0
0.8
0.6
0.4
0.2
0.0
Absorption
3
2
1
0
Photoluminescence Signal (arb. units)
1900
2000
2100
2200
2300
2400
Frequency (cm-1)
(a)
(b)
(c)

Fig. 5

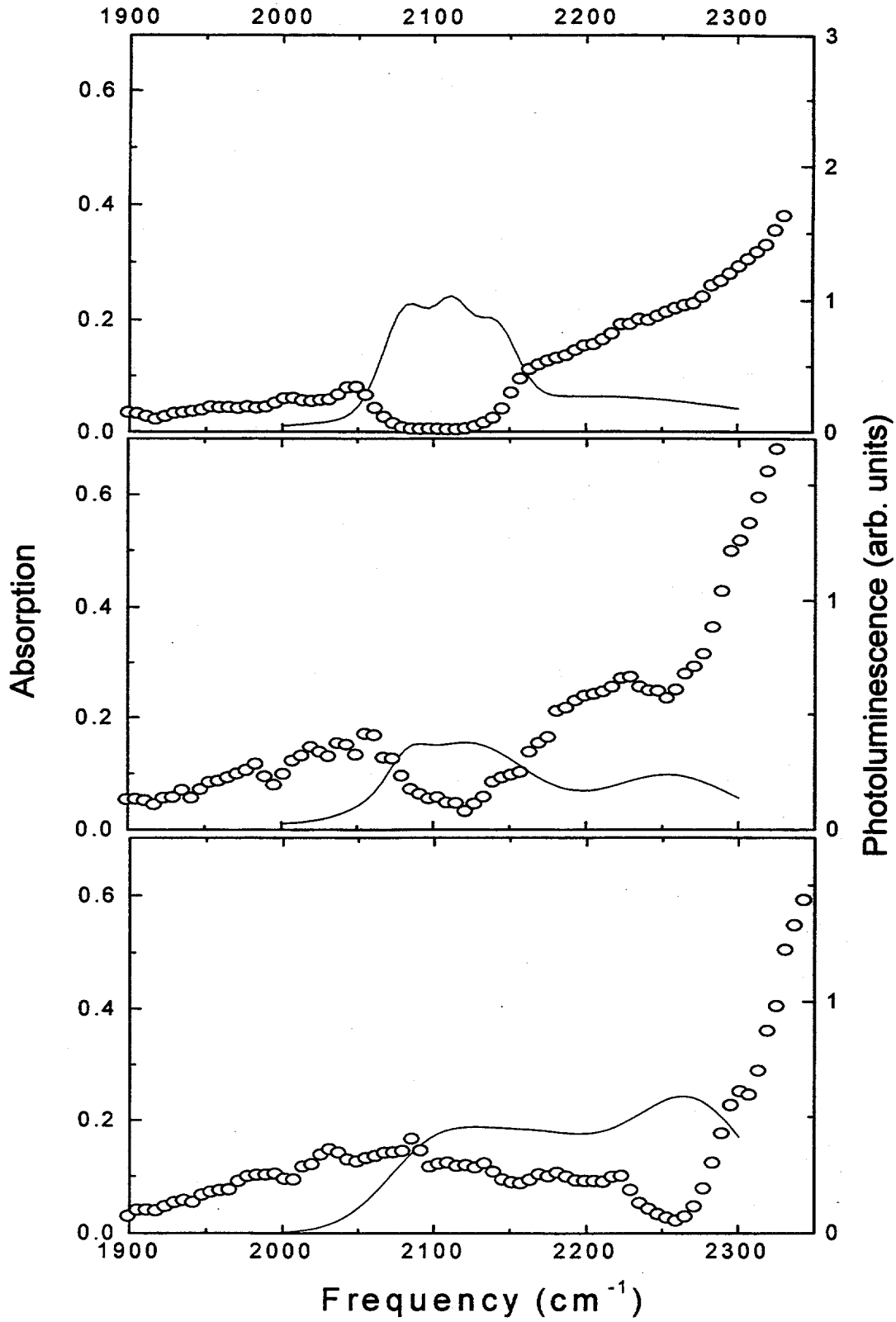
1900
2000
2100
2200
2300
0.6
0.4
0.2
0.0
3
2
1
0
Absorption
Photoluminescence (arb. units)
Frequency (cm^{-1})

Fig. 6

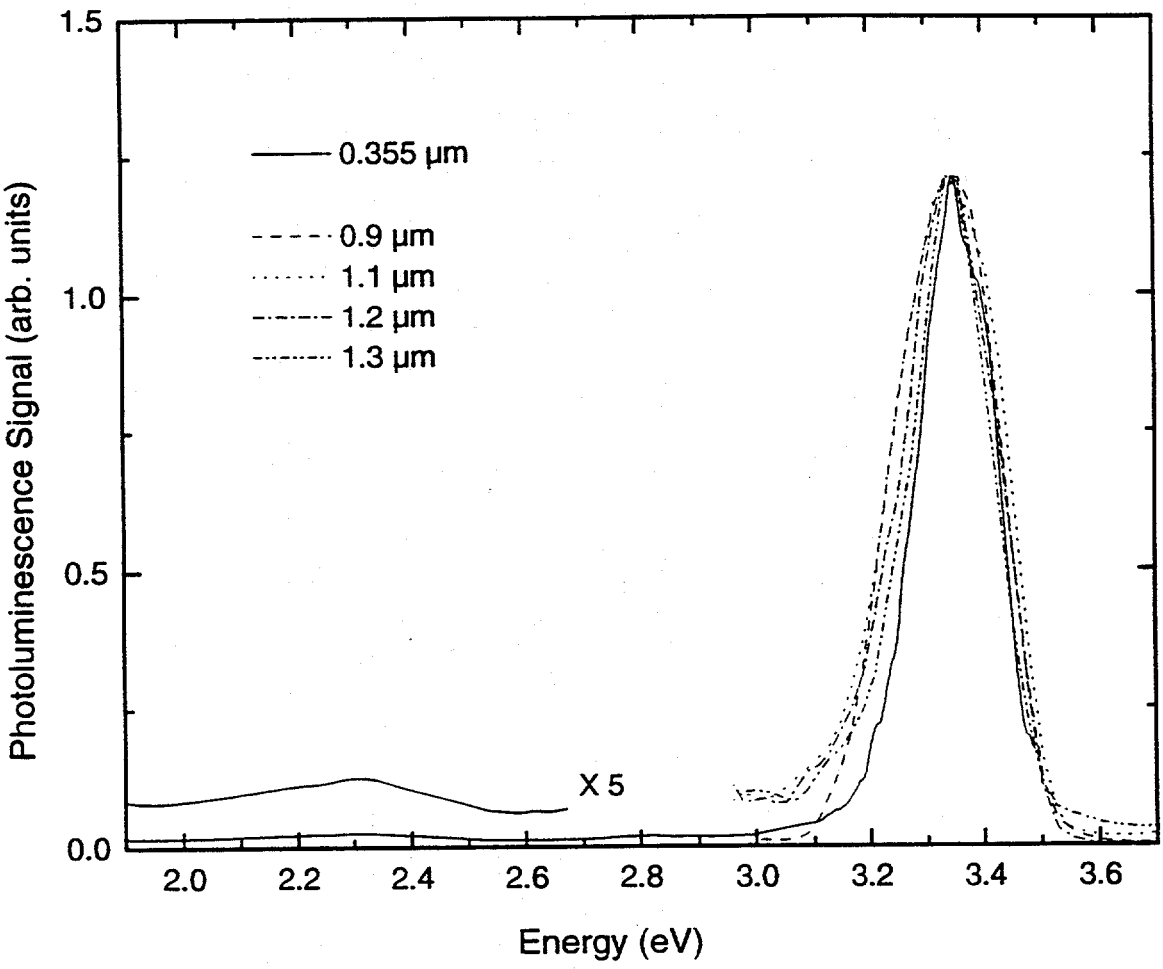
1.5
1.0
0.5
0.0
Photoluminescence Signal (arb. units)
0.355 μm
0.9 μm
1.1 μm
1.2 μm
1.3 μm
X 5
2.0
2.2
2.4
2.6
2.8
3.0
3.2
3.4
3.6
Energy (eV)

Fig. 7

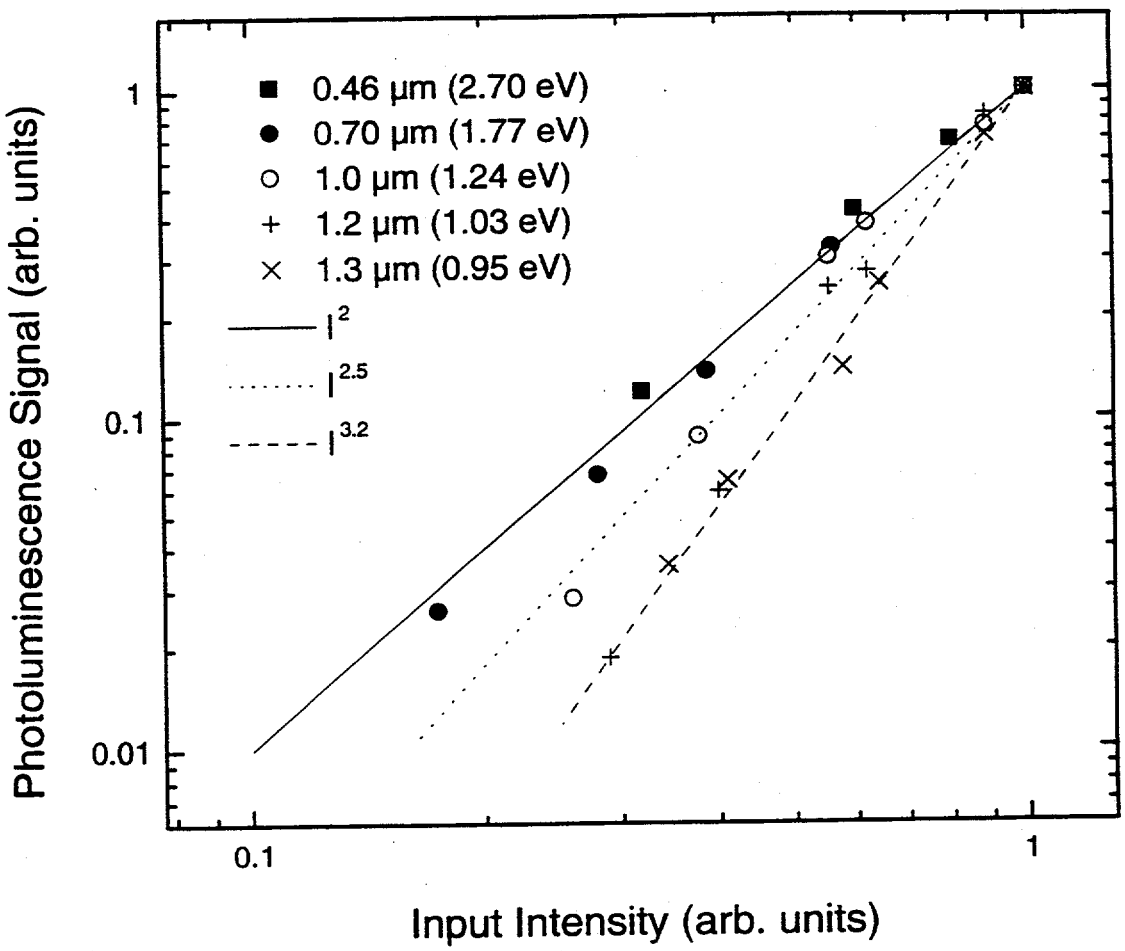
0.46 μm (2.70 eV)
0.70 μm (1.77 eV)
1.0 μm (1.24 eV)
1.2 μm (1.03 eV)
1.3 μm (0.95 eV)
I^2
I^2.5
I^3.2
Photoluminescence Signal (arb. units)
Input Intensity (arb. units)
1
0.1
0.01
0.1
1

Fig. 8

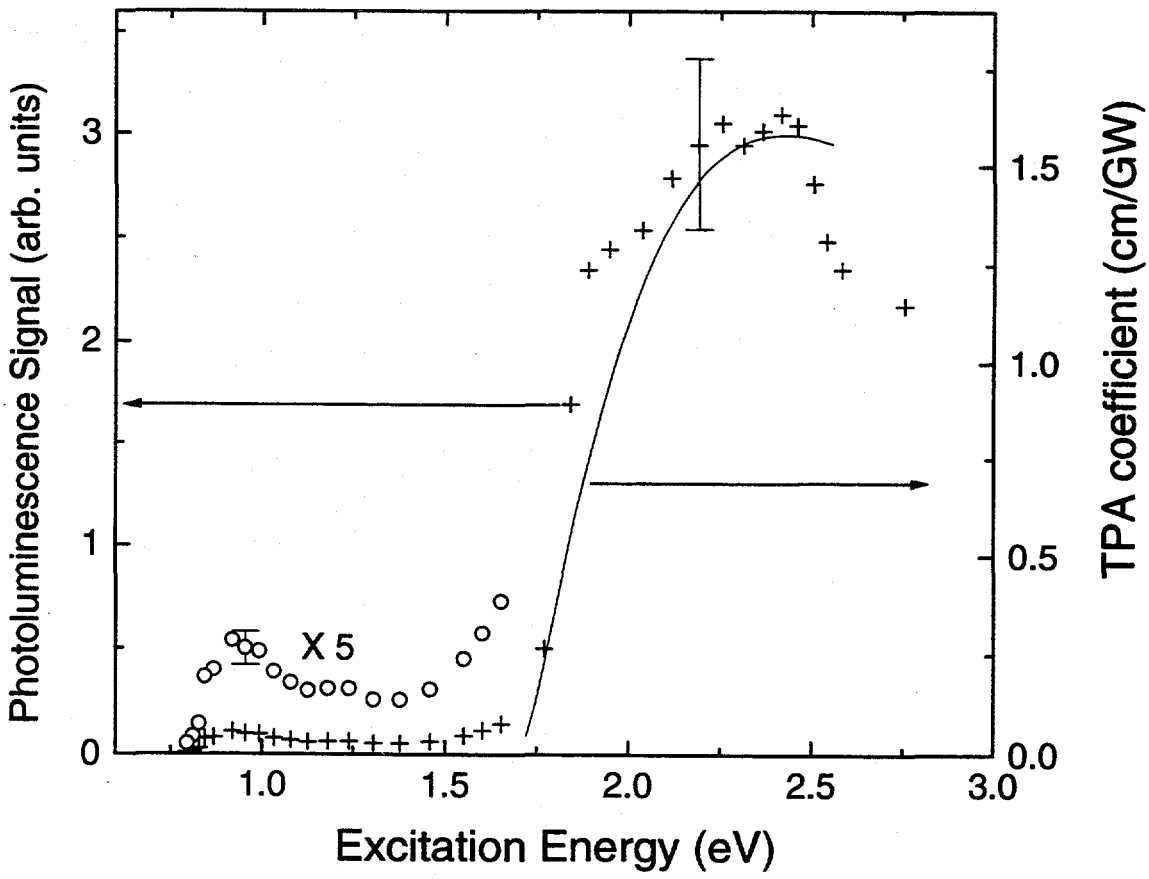
Photoluminescence Signal (arb. units)
TPA coefficient (cm/GW)
Excitation Energy (eV)
X 5
0
1
2
3
0.0
0.5
1.0
1.5
1.0
1.5
2.0
2.5
3.0

Fig. 9

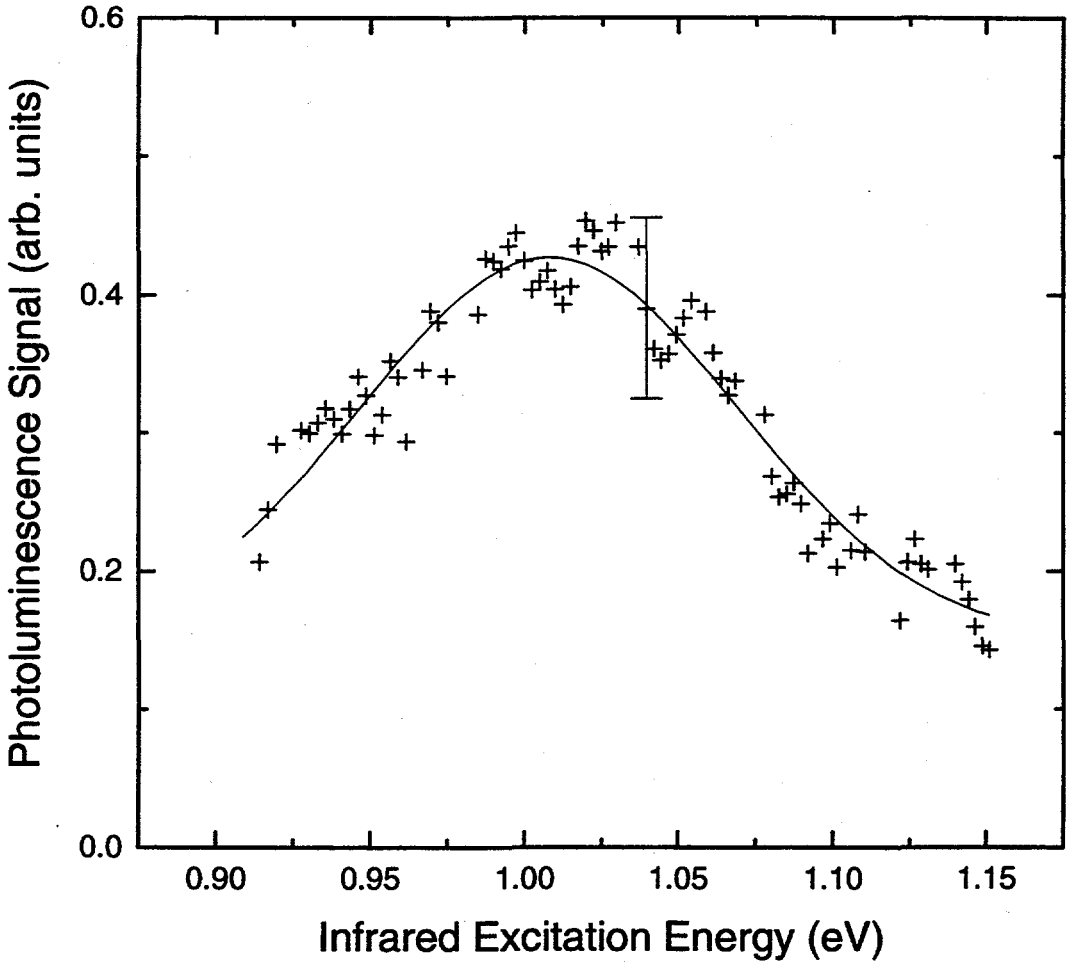
0.6
0.4
0.2
0.0
Photoluminescence Signal (arb. units)
0.90
0.95
1.00
1.05
1.10
1.15
Infrared Excitation Energy (eV)

Fig. 10